

transverse energy production and charged-particle multiplicity at midrapidity in various systems from $\sqrt{s_{NN}} = 7.7$ to 200 GeV

(PHENIX Collaboration) Adare, A.; ...; Makek, Mihael; ...; Zou, L.

Source / Izvornik: **Physical Review C - Nuclear Physics, 2016, 93**

Journal article, Published version

Rad u časopisu, Objavljena verzija rada (izdavačev PDF)

<https://doi.org/10.1103/PhysRevC.93.024901>

Permanent link / Trajna poveznica: <https://um.nsk.hr/um:nbn:hr:217:813615>

Rights / Prava: [In copyright](#) / [Zaštićeno autorskim pravom.](#)

Download date / Datum preuzimanja: **2024-08-06**



Repository / Repozitorij:

[Repository of the Faculty of Science - University of Zagreb](#)



Transverse energy production and charged-particle multiplicity at midrapidity in various systems from $\sqrt{s_{NN}} = 7.7$ to 200 GeV

A. Adare,¹³ S. Afanasiev,³² C. Aidala,^{14,43,47,48} N. N. Ajitanand,⁶⁸ Y. Akiba,^{62,63} R. Akimoto,¹² H. Al-Bataineh,⁵⁶ J. Alexander,⁶⁸ M. Alfred,²⁵ A. Al-Jamel,⁵⁶ H. Al-Ta'ani,⁵⁶ A. Angerami,¹⁴ K. Aoki,^{36,39,62} N. Apadula,^{30,69} L. Aphecetche,⁷⁰ Y. Aramaki,^{12,62} R. Armendariz,⁵⁶ S. H. Aronson,⁷ J. Asai,⁶³ H. Asano,^{39,62} E. C. Aschenauer,⁷ E. T. Atomssa,^{40,69} R. Averbeck,⁶⁹ T. C. Awes,⁵⁸ B. Azmoun,⁷ V. Babintsev,²⁶ M. Bai,⁶ X. Bai,¹¹ G. Baksay,²⁰ L. Baksay,²⁰ A. Baldissieri,¹⁶ N. S. Bandara,⁴⁷ B. Bannier,⁶⁹ K. N. Barish,⁸ P. D. Barnes,^{43,*} B. Bassalleck,⁵⁵ A. T. Basye,¹ S. Bathe,^{5,8,63} S. Batsouli,^{14,58} V. Baublis,⁶¹ F. Bauer,⁸ C. Baumann,^{7,49} S. Baumgart,⁶² A. Bazilevsky,⁷ M. Beaumier,⁸ S. Beckman,¹³ S. Belikov,^{7,30,*} R. Belmont,^{13,48,75} R. Bennett,⁶⁹ A. Berdnikov,⁶⁵ Y. Berdnikov,⁶⁵ J. H. Bhom,⁷⁹ A. A. Bickley,¹³ M. T. Bjorndal,¹⁴ D. Black,⁸ D. S. Blau,³⁸ J. G. Boissevain,⁴³ J. S. Bok,^{55,56,79} H. Borel,¹⁶ K. Boyle,^{63,69} M. L. Brooks,⁴³ D. S. Brown,⁵⁶ J. Bryslawski,⁵ D. Bucher,⁴⁹ H. Buesching,⁷ V. Bumazhnov,²⁶ G. Bunce,^{7,63} J. M. Burward-Hoy,⁴³ S. Butsyk,^{43,55,69} S. Campbell,^{14,30,69} A. Caringi,⁵⁰ P. Castera,⁶⁹ J.-S. Chai,^{34,71} B. S. Chang,⁷⁹ J.-L. Charvet,¹⁶ C.-H. Chen,^{63,69} S. Chernichenko,²⁶ C. Y. Chi,¹⁴ J. Chiba,³⁶ M. Chiu,^{7,14,27} I. J. Choi,^{27,79} J. B. Choi,¹⁰ S. Choi,⁶⁷ R. K. Choudhury,⁴ P. Christiansen,⁴⁵ T. Chujo,^{74,75} P. Chung,⁶⁸ A. Churny,²⁶ O. Chvala,⁸ V. Cianciolo,⁵⁸ Z. Citron,^{69,77} C. R. Cleven,²² Y. Cobigo,¹⁶ B. A. Cole,¹⁴ M. P. Comets,⁵⁹ Z. Conesa del Valle,⁴⁰ M. Connors,⁶⁹ P. Constantin,^{30,43} N. Cronin,^{50,69} N. Crossette,⁵⁰ M. Csanád,¹⁸ T. Csörgő,⁷⁸ T. Dahms,⁶⁹ S. Dairaku,^{39,62} I. Danchev,⁷⁵ T. W. Danley,⁵⁷ K. Das,²¹ A. Datta,^{47,55} M. S. Daugherty,¹ G. David,⁷ M. K. Dayananda,²² M. B. Deaton,¹ K. DeBlasio,⁵⁵ K. Dehmelt,^{20,69} H. Delagrange,^{70,*} A. Denisov,²⁶ D. d'Enterria,¹⁴ A. Deshpande,^{63,69} E. J. Desmond,⁷ K. V. Dharmawardane,⁵⁶ O. Dietzsch,⁶⁶ L. Ding,³⁰ A. Dion,^{30,69} P. B. Diss,⁴⁶ J. H. Do,⁷⁹ M. Donadelli,⁶⁶ L. D'Orazio,⁴⁶ J. L. Drachenberg,¹ O. Drapier,⁴⁰ A. Drees,⁶⁹ K. A. Drees,⁶ A. K. Dubey,⁷⁷ J. M. Durham,^{43,69} A. Durum,²⁶ D. Dutta,⁴ V. Dzordzhadze,^{8,72} S. Edwards,^{6,21} Y. V. Efremenko,⁵⁸ J. Egdemir,⁶⁹ F. Ellinghaus,¹³ W. S. Emam,⁸ T. Engelmöore,¹⁴ A. Enokizono,^{24,42,58,62,64} H. En'yo,^{62,63} B. Espagnon,⁵⁹ S. Esumi,⁷⁴ K. O. Eyser,^{7,8} B. Fadern,⁵⁰ N. Feege,⁶⁹ D. E. Fields,^{55,63} M. Finger,^{9,32} M. Finger, Jr.,^{9,32} F. Fleuret,⁴⁰ S. L. Fokin,³⁸ B. Forestier,⁴⁴ Z. Fraenkel,^{77,*} J. E. Frantz,^{14,57,69} A. Franz,⁷ A. D. Frawley,²¹ K. Fujiwara,⁶² Y. Fukao,^{36,39,62} S.-Y. Fung,⁸ T. Fusayasu,⁵² S. Gadrat,⁴⁴ K. Gainey,¹ C. Gal,⁶⁹ P. Gallus,¹⁵ P. Garg,³ A. Garishvili,⁷² I. Garishvili,^{42,72} F. Gastineau,⁷⁰ H. Ge,⁶⁹ M. Germain,⁷⁰ F. Giordano,²⁷ A. Glenn,^{13,42,72} H. Gong,⁶⁹ X. Gong,⁶⁸ M. Gonin,⁴⁰ J. Gosset,¹⁶ Y. Goto,^{62,63} R. Granier de Cassagnac,⁴⁰ N. Grau,^{2,14,30} S. V. Greene,⁷⁵ G. Grim,⁴³ M. Grosse Perdekamp,^{27,63} Y. Gu,⁶⁸ T. Gunji,¹² L. Guo,⁴³ H. Guragain,²² H.-Å. Gustafsson,^{45,*} T. Hachiya,^{24,62} A. Hadj Henni,⁷⁰ C. Haegemann,⁵⁵ J. S. Haggerty,⁷ M. N. Hagiwara,¹ K. I. Hahn,¹⁹ H. Hamagaki,¹² J. Hamblen,⁷² H. F. Hamilton,¹ R. Han,⁶⁰ S. Y. Han,¹⁹ J. Hanks,^{14,69} H. Harada,²⁴ E. P. Hartouni,⁴² K. Haruna,²⁴ M. Harvey,⁷ S. Hasegawa,³¹ T. O. S. Haseler,²² K. Hashimoto,^{62,64} E. Haslum,⁴⁵ K. Hasuko,⁶² R. Hayano,¹² S. Hayashi,¹² X. He,²² M. Heffner,⁴² T. K. Hemmick,⁶⁹ T. Hester,⁸ J. M. Heuser,⁶² H. Hiejima,²⁷ J. C. Hill,³⁰ R. Hobbs,⁵⁵ M. Hohmann,²⁰ R. S. Hollis,⁸ M. Holmes,⁷⁵ W. Holzmann,^{14,68} K. Homma,²⁴ B. Hong,³⁷ T. Horaguchi,^{24,62,73,74} Y. Hori,¹² D. Hornback,⁷² T. Hoshino,²⁴ N. Hotvedt,³⁰ J. Huang,^{7,43} S. Huang,⁷⁵ M. G. Hur,³⁴ T. Ichihara,^{62,63} R. Ichimiya,⁶² H. Iinuma,^{36,39,62} Y. Ikeda,^{62,74} K. Imai,^{31,39,62} Y. Imazu,⁶² J. Imrek,¹⁷ M. Inaba,⁷⁴ Y. Inoue,^{62,64} A. Iordanova,⁸ D. Isenhower,¹ L. Isenhower,¹ M. Ishihara,⁶² A. Isinhue,⁵⁰ T. Isobe,¹² M. Issah,^{68,75} A. Isupov,³² D. Ivanishchev,⁶¹ Y. Iwanaga,²⁴ B. V. Jacak,⁶⁹ M. Javani,²² S. J. Jeon,⁵¹ M. Jezghani,²² J. Jia,^{7,14,68} X. Jiang,⁴³ J. Jin,¹⁴ O. Jinnouchi,⁶³ B. M. Johnson,⁷ T. Jones,¹ K. S. Joo,⁵¹ D. Jouan,⁵⁹ D. S. Jumper,^{1,27} F. Kajihara,^{12,62} S. Kametani,^{12,76} N. Kamihara,^{62,73} J. Kamin,⁶⁹ S. Kanda,^{12,36} M. Kaneta,⁶³ S. Kaneti,⁶⁹ B. H. Kang,²³ J. H. Kang,⁷⁹ J. S. Kang,²³ H. Kanou,^{62,73} J. Kapustinsky,⁴³ K. Karatsu,^{39,62} M. Kasai,^{62,64} T. Kawagishi,⁷⁴ D. Kawall,^{47,63} M. Kawashima,^{62,64} A. V. Kazantsev,³⁸ S. Kelly,¹³ T. Kempel,³⁰ J. A. Key,⁵⁵ V. Khachatryan,⁶⁹ P. K. Khandai,³ A. Khanzadeev,⁶¹ K. M. Kijima,²⁴ J. Kikuchi,⁷⁶ A. Kim,¹⁹ B. I. Kim,³⁷ C. Kim,³⁷ D. H. Kim,⁵¹ D. J. Kim,^{33,79} E. Kim,⁶⁷ E.-J. Kim,¹⁰ G. W. Kim,¹⁹ H. J. Kim,⁷⁹ K.-B. Kim,¹⁰ M. Kim,⁶⁷ Y.-J. Kim,²⁷ Y. K. Kim,²³ Y.-S. Kim,³⁴ B. Kimelman,⁵⁰ E. Kinney,¹³ Á. Kiss,¹⁸ E. Kistenev,⁷ R. Kitamura,¹² A. Kiyomichi,⁶² J. Klatsky,²¹ J. Klay,⁴² C. Klein-Boesing,⁴⁹ D. Kleinjan,⁸ P. Kline,⁶⁹ T. Koblesky,¹³ L. Kochenda,⁶¹ V. Kochetkov,²⁶ M. Kofarago,¹⁸ Y. Komatsu,^{12,36} B. Komkov,⁶¹ M. Konno,⁷⁴ J. Koster,^{27,63} D. Kotchetkov,^{8,57} D. Kotov,^{61,65} A. Kozlov,⁷⁷ A. Král,¹⁵ A. Kravitz,¹⁴ F. Krizek,³³ P. J. Kroon,⁷ J. Kubart,^{9,29} G. J. Kunde,⁴³ N. Kurihara,¹² K. Kurita,^{62,64} M. Kurosawa,^{62,63} M. J. Kweon,³⁷ Y. Kwon,^{72,79} G. S. Kyle,⁵⁶ R. Lacey,⁶⁸ Y. S. Lai,¹⁴ J. G. Lajoie,³⁰ A. Lebedev,³⁰ Y. Le Bornec,⁵⁹ S. Leckey,⁶⁹ B. Lee,²³ D. M. Lee,⁴³ G. H. Lee,¹⁰ J. Lee,¹⁹ K. B. Lee,^{37,43} K. S. Lee,³⁷ M. K. Lee,⁷⁹ S. Lee,⁷⁹ S. H. Lee,⁶⁹ S. R. Lee,¹⁰ T. Lee,⁶⁷ M. J. Leitch,⁴³ M. A. L. Leite,⁶⁶ M. Leitgab,²⁷ B. Lenzi,⁶⁶ B. Lewis,⁶⁹ X. Li,¹¹ X. H. Li,⁸ P. Lichtenwalner,⁵⁰ P. Liebing,⁶³ H. Lim,⁶⁷ S. H. Lim,⁷⁹ L. A. Linden Levy,^{13,27,42} T. Liška,¹⁵ A. Litvinenko,³² H. Liu,⁴³ M. X. Liu,⁴³ B. Love,⁷⁵ D. Lynch,⁷ C. F. Maguire,⁷⁵ Y. I. Makdisi,^{6,7} M. Makek,^{77,80} A. Malakhov,³² M. D. Malik,⁵⁵ A. Manion,⁶⁹ V. I. Manko,³⁸ E. Mannel,^{7,14} Y. Mao,^{60,62} T. Maruyama,³¹ L. Mašek,^{9,29} H. Masui,⁷⁴ S. Masumoto,^{12,36} F. Matathias,^{14,69} M. C. McCain,²⁷ M. McCumber,^{13,43,69} P. L. McGaughey,⁴³ D. McGlinchey,^{13,21} C. McKinney,²⁷ N. Means,⁶⁹ A. Meles,⁵⁶ M. Mendoza,⁸ B. Meredith,²⁷ Y. Miake,⁷⁴ T. Mibe,³⁶ J. Midori,²⁴ A. C. Mignerey,⁴⁶ P. Mikeš,^{9,29} K. Miki,^{62,74} T. E. Miller,⁷⁵ A. Milov,^{7,69,77} S. Mioduszewski,⁷ D. K. Mishra,⁴ G. C. Mishra,²² M. Mishra,³ J. T. Mitchell,⁷ M. Mitrovski,⁶⁸ Y. Miyachi,^{62,73} S. Miyasaka,^{62,73} S. Mizuno,^{62,74} A. K. Mohanty,⁴ S. Mohapatra,⁶⁸ P. Montuenga,²⁷ H. J. Moon,⁵¹ T. Moon,⁷⁹ Y. Morino,¹² A. Morreale,⁸ D. P. Morrison,^{7,†} M. Moskowitz,⁵⁰ J. M. Moss,⁴³ S. Motschwiller,⁵⁰ T. V. Moukhanova,³⁸ D. Mukhopadhyay,⁷⁵ T. Murakami,^{39,62} J. Murata,^{62,64} A. Mwai,⁶⁸ T. Nagae,³⁹ S. Nagamiya,^{36,62} K. Nagashima,²⁴ Y. Nagata,⁷⁴ J. L. Nagle,^{13,‡} M. Naglis,⁷⁷ M. I. Nagy,^{18,78} I. Nakagawa,^{62,63} H. Nakagomi,^{62,74} Y. Nakamiya,²⁴ K. R. Nakamura,^{39,62} T. Nakamura,^{24,62} K. Nakano,^{62,73} S. Nam,¹⁹

C. Nattrass,⁷² A. Nederlof,⁵⁰ P. K. Netrakanti,⁴ J. Newby,⁴² M. Nguyen,⁶⁹ M. Nishashi,^{24,62} T. Niida,⁷⁴ S. Nishimura,¹² B. E. Norman,⁴³ R. Nouicer,^{7,63} T. Novák,^{35,78} N. Novitzky,^{33,69} A. Nukariya,¹² A. S. Nyanin,³⁸ J. Nystrand,⁴⁵ C. Oakley,²² H. Obayashi,²⁴ E. O'Brien,⁷ S. X. Oda,¹² C. A. Ogilvie,³⁰ H. Ohnishi,⁶² H. Oide,¹² I. D. Ojha,⁷⁵ M. Oka,⁷⁴ K. Okada,⁶³ O. O. Omiwade,¹ Y. Onuki,⁶² J. D. Orjuela Koop,¹³ J. D. Osborn,⁴⁸ A. Oskarsson,⁴⁵ I. Otterlund,⁴⁵ M. Ouchida,^{24,62} K. Ozawa,^{12,36} R. Pak,⁷ D. Pal,⁷⁵ A. P. T. Palounek,⁴³ V. Pantuev,^{28,69} V. Papavassiliou,⁵⁶ B. H. Park,²³ I. H. Park,¹⁹ J. Park,^{10,67} J. S. Park,⁶⁷ S. Park,⁶⁷ S. K. Park,³⁷ W. J. Park,³⁷ S. F. Pate,⁵⁶ L. Patel,²² M. Patel,³⁰ H. Pei,³⁰ J.-C. Peng,²⁷ H. Pereira,¹⁶ D. V. Perepelitsa,^{7,14} G. D. N. Perera,⁵⁶ V. Peresedov,³² D. Yu. Peressounko,³⁸ J. Perry,³⁰ R. Petti,^{7,69} C. Pinkenburg,⁷ R. Pinson,¹ R. P. Pisani,⁷ M. Proissl,⁶⁹ M. L. Purschke,⁷ A. K. Purwar,^{43,69} H. Qu,^{1,22} J. Rak,^{30,33,55} A. Rakotozafindrabe,⁴⁰ B. J. Ramson,⁴⁸ I. Ravinovich,⁷⁷ K. F. Read,^{58,72} S. Rembeczki,²⁰ M. Reuter,⁶⁹ K. Reygers,⁴⁹ D. Reynolds,⁶⁸ V. Riabov,^{54,61} Y. Riabov,^{61,65} E. Richardson,⁴⁶ T. Rinn,³⁰ N. Riveli,⁵⁷ D. Roach,⁷⁵ G. Roche,^{44,*} S. D. Rolnick,⁸ A. Romana,^{40,*} M. Rosati,³⁰ C. A. Rosen,¹³ S. S. E. Rosendahl,⁴⁵ P. Rosnet,⁴⁴ Z. Rowan,⁵ J. G. Rubin,⁴⁸ P. Rukoyatkin,³² P. Ružička,²⁹ V. L. Rykov,⁶² M. S. Ryu,²³ S. S. Ryu,⁷⁹ B. Sahlmueller,^{49,69} N. Saito,^{36,39,62,63} T. Sakaguchi,^{7,12,76} S. Sakai,⁷⁴ K. Sakashita,^{62,73} H. Sakata,²⁴ H. Sako,³¹ V. Samsonov,^{54,61} M. Sano,⁷⁴ S. Sano,^{12,76} M. Sarsour,²² H. D. Sato,^{39,62} S. Sato,^{7,31,36,74} T. Sato,⁷⁴ S. Sawada,³⁶ B. Schaefer,⁷⁵ B. K. Schmoll,⁷² K. Sedgwick,⁸ J. Seele,^{13,63} R. Seidl,^{27,62,63} Y. Sekiguchi,¹² V. Semenov,²⁶ A. Sen,^{22,72} R. Seto,⁸ P. Sett,⁴ A. Sexton,⁴⁶ D. Sharma,^{69,77} A. Shaver,³⁰ T. K. Shea,⁷ I. Shein,²⁶ A. Shevel,^{61,68} T.-A. Shibata,^{62,73} K. Shigaki,²⁴ M. Shimomura,^{30,53,74} T. Shohjoh,⁷⁴ K. Shoji,^{39,62} P. Shukla,⁴ A. Sickles,^{7,27,69} C. L. Silva,^{30,43,66} D. Silvermyr,^{45,58} C. Silvestre,¹⁶ K. S. Sim,³⁷ B. K. Singh,³ C. P. Singh,³ V. Singh,³ M. Skolnik,⁵⁰ S. Skutnik,³⁰ M. Slunečka,^{9,32} W. C. Smith,¹ M. Snowball,⁴³ S. Solano,⁵⁰ A. Soldatov,²⁶ R. A. Soltz,⁴² W. E. Sondheim,⁴³ S. P. Sorensen,⁷² I. V. Sourikova,⁷ F. Staley,¹⁶ P. W. Stankus,⁵⁸ P. Steinberg,⁷ E. Stenlund,⁴⁵ M. Stepanov,^{47,56,*} A. Ster,⁷⁸ S. P. Stoll,⁷ M. R. Stone,¹³ T. Sugitate,²⁴ C. Suire,⁵⁹ A. Sukhanov,⁷ J. P. Sullivan,⁴³ T. Sumita,⁶² J. Sun,⁶⁹ J. Sziklai,⁷⁸ T. Tabaru,⁶³ S. Takagi,⁷⁴ E. M. Takagui,⁶⁶ A. Takahara,¹² A. Taketani,^{62,63} R. Tanabe,⁷⁴ K. H. Tanaka,³⁶ Y. Tanaka,⁵² S. Taneja,⁶⁹ K. Tanida,^{39,62,63,67} M. J. Tannenbaum,⁷ S. Tarafdar,^{3,77} A. Taranenko,^{54,68} P. Tarján,¹⁷ E. Tennant,⁵⁶ H. Themann,⁶⁹ D. Thomas,¹ T. L. Thomas,⁵⁵ R. Tieulent,²² A. Timilsina,³⁰ T. Todoroki,^{62,74} M. Togawa,^{39,62,63} A. Toia,⁶⁹ J. Tojo,⁶² L. Tomášek,²⁹ M. Tomášek,^{15,29} H. Torii,^{12,24,62} C. L. Towell,¹ R. Towell,¹ R. S. Towell,¹ V.-N. Tram,⁴⁰ I. Tserruya,⁷⁷ Y. Tsuchimoto,^{12,24,62} T. Tsuji,¹² S. K. Tuli,^{3,*} H. Tydesjö,⁴⁵ N. Tyurin,²⁶ C. Vale,^{7,30} H. Valle,⁷⁵ H. W. van Hecke,¹⁵ M. Vargyas,¹⁸ E. Vazquez-Zambrano,¹⁴ A. Veicht,^{14,27} J. Velkovska,⁷⁵ R. Vértesi,^{17,78} A. A. Vinogradov,³⁸ M. Virius,¹⁵ B. Voas,³⁰ A. Vossen,²⁷ V. Vrba,^{15,29} E. Vznuzdaev,⁶¹ M. Wagner,^{39,62} D. Walker,⁶⁹ X. R. Wang,^{56,63} D. Watanabe,²⁴ K. Watanabe,^{62,64,74} Y. Watanabe,^{62,63} Y. S. Watanabe,^{12,36} F. Wei,^{30,56} R. Wei,⁶⁸ J. Wessels,⁴⁹ S. Whitaker,³⁰ A. S. White,⁴⁸ S. N. White,⁷ N. Willis,⁵⁹ D. Winter,¹⁴ S. Wolin,²⁷ C. L. Woody,⁷ R. M. Wright,¹ M. Wysocki,^{13,58} B. Xia,⁵⁷ W. Xie,^{8,63} L. Xue,²² S. Yalcin,⁶⁹ Y. L. Yamaguchi,^{12,62,69,76} K. Yamaura,²⁴ R. Yang,²⁷ A. Yanovich,²⁶ Z. Yasin,⁸ J. Ying,²² S. Yokkaichi,^{62,63} J. H. Yoo,³⁷ I. Yoon,⁶⁷ Z. You,^{43,60} G. R. Young,⁵⁸ I. Younus,^{41,55} H. Yu,⁶⁰ I. E. Yushmanov,³⁸ W. A. Zajc,¹⁴ O. Zaudtke,⁴⁹ A. Zelenski,⁶ C. Zhang,^{14,58} S. Zhou,¹¹ J. Zimanyi,^{78,*} L. Zolin,³² and L. Zou⁸

(PHENIX Collaboration)

¹Abilene Christian University, Abilene, Texas 79699, USA²Department of Physics, Augustana University, Sioux Falls, South Dakota 57197, USA³Department of Physics, Banaras Hindu University, Varanasi 221005, India⁴Bhabha Atomic Research Centre, Bombay 400 085, India⁵Baruch College, City University of New York, New York, New York 10010, USA⁶Collider-Accelerator Department, Brookhaven National Laboratory, Upton, New York 11973-5000, USA⁷Physics Department, Brookhaven National Laboratory, Upton, New York 11973-5000, USA⁸University of California-Riverside, Riverside, California 92521, USA⁹Charles University, Ovocný trh 5, Praha 1, 116 36 Prague, Czech Republic¹⁰Chonbuk National University, Jeonju 561-756, Korea¹¹Science and Technology on Nuclear Data Laboratory, China Institute of Atomic Energy, Beijing 102413, People's Republic of China¹²Center for Nuclear Study, Graduate School of Science, University of Tokyo, 7-3-1 Hongo, Bunkyo, Tokyo 113-0033, Japan¹³University of Colorado, Boulder, Colorado 80309, USA¹⁴Columbia University, New York, New York 10027, USA, and Nevis Laboratories, Irvington, New York 10533, USA¹⁵Czech Technical University, Zikova 4, 166 36 Prague 6, Czech Republic¹⁶Dapnia, CEA Saclay, F-91191 Gif-sur-Yvette, France¹⁷Debrecen University, H-4010 Debrecen, Egyetem tér 1, Hungary¹⁸ELTE, Eötvös Loránd University, H-1117 Budapest, Pázmány P. s. 1/A, Hungary¹⁹Ewha Womans University, Seoul 120-750, Korea²⁰Florida Institute of Technology, Melbourne, Florida 32901, USA²¹Florida State University, Tallahassee, Florida 32306, USA²²Georgia State University, Atlanta, Georgia 30303, USA²³Hanyang University, Seoul 133-792, Korea²⁴Hiroshima University, Kagamiyama, Higashi-Hiroshima 739-8526, Japan²⁵Department of Physics and Astronomy, Howard University, Washington, DC 20059, USA²⁶IHEP Protvino, State Research Center of Russian Federation, Institute for High Energy Physics, Protvino 142281, Russia

- ²⁷University of Illinois at Urbana-Champaign, Urbana, Illinois 61801, USA
- ²⁸Institute for Nuclear Research of the Russian Academy of Sciences, prospekt 60-letiya Oktyabrya 7a, Moscow 117312, Russia
- ²⁹Institute of Physics, Academy of Sciences of the Czech Republic, Na Slovance 2, 182 21 Prague 8, Czech Republic
- ³⁰Iowa State University, Ames, Iowa 50011, USA
- ³¹Advanced Science Research Center, Japan Atomic Energy Agency, 2-4 Shirakata Shirane, Tokai-mura, Naka-gun, Ibaraki-ken 319-1195, Japan
- ³²Joint Institute for Nuclear Research, 141980 Dubna, Moscow Region, Russia
- ³³Helsinki Institute of Physics and University of Jyväskylä, P.O. Box 35, FI-40014 Jyväskylä, Finland
- ³⁴KAERI, Cyclotron Application Laboratory, Seoul, Korea
- ³⁵Károly Róberts University College, H-3200 Gyöngyös, Mátrai út 36, Hungary
- ³⁶KEK, High Energy Accelerator Research Organization, Tsukuba, Ibaraki 305-0801, Japan
- ³⁷Korea University, Seoul 136-701, Korea
- ³⁸National Research Center “Kurchatov Institute,” Moscow 123098, Russia
- ³⁹Kyoto University, Kyoto 606-8502, Japan
- ⁴⁰Laboratoire Leprince-Ringuet, Ecole Polytechnique, CNRS-IN2P3, Route de Saclay, F-91128 Palaiseau, France
- ⁴¹Physics Department, Lahore University of Management Sciences, Lahore 54792, Pakistan
- ⁴²Lawrence Livermore National Laboratory, Livermore, California 94550, USA
- ⁴³Los Alamos National Laboratory, Los Alamos, New Mexico 87545, USA
- ⁴⁴LPC, Université Blaise Pascal, CNRS-IN2P3, Clermont-Fd, 63177 Aubiere Cedex, France
- ⁴⁵Department of Physics, Lund University, Box 118, SE-221 00 Lund, Sweden
- ⁴⁶University of Maryland, College Park, Maryland 20742, USA
- ⁴⁷Department of Physics, University of Massachusetts, Amherst, Massachusetts 01003-9337, USA
- ⁴⁸Department of Physics, University of Michigan, Ann Arbor, Michigan 48109-1040, USA
- ⁴⁹Institut für Kernphysik, University of Muenster, D-48149 Muenster, Germany
- ⁵⁰Muhlenberg College, Allentown, Pennsylvania 18104-5586, USA
- ⁵¹Myongji University, Yongin, Kyonggido 449-728, Korea
- ⁵²Nagasaki Institute of Applied Science, Nagasaki-shi, Nagasaki 851-0193, Japan
- ⁵³Nara Women’s University, Kita-uoya Nishi-machi Nara 630-8506, Japan
- ⁵⁴National Research Nuclear University, MPhI, Moscow Engineering Physics Institute, Moscow 115409, Russia
- ⁵⁵University of New Mexico, Albuquerque, New Mexico 87131, USA
- ⁵⁶New Mexico State University, Las Cruces, New Mexico 88003, USA
- ⁵⁷Department of Physics and Astronomy, Ohio University, Athens, Ohio 45701, USA
- ⁵⁸Oak Ridge National Laboratory, Oak Ridge, Tennessee 37831, USA
- ⁵⁹IPN-Orsay, Univ. Paris-Sud, CNRS/IN2P3, Université Paris-Saclay, BP1, F-91406 Orsay, France
- ⁶⁰Peking University, Beijing 100871, People’s Republic of China
- ⁶¹PNPI, Petersburg Nuclear Physics Institute, Gatchina, Leningrad Region 188300, Russia
- ⁶²RIKEN Nishina Center for Accelerator-Based Science, Wako, Saitama 351-0198, Japan
- ⁶³RIKEN BNL Research Center, Brookhaven National Laboratory, Upton, New York 11973-5000, USA
- ⁶⁴Physics Department, Rikkyo University, 3-34-1 Nishi-Ikebukuro, Toshima, Tokyo 171-8501, Japan
- ⁶⁵Saint Petersburg State Polytechnic University, St. Petersburg 195251, Russia
- ⁶⁶Universidade de São Paulo, Instituto de Física, Caixa Postal 66318, São Paulo CEP05315-970, Brazil
- ⁶⁷Department of Physics and Astronomy, Seoul National University, Seoul 151-742, Korea
- ⁶⁸Chemistry Department, Stony Brook University, SUNY, Stony Brook, New York 11794-3400, USA
- ⁶⁹Department of Physics and Astronomy, Stony Brook University, SUNY, Stony Brook, New York 11794-3800, USA
- ⁷⁰SUBATECH (Ecole des Mines de Nantes, CNRS-IN2P3, Université de Nantes) BP 20722-44307, Nantes, France
- ⁷¹Sungkyunkwan University, Suwon 440-746, Korea
- ⁷²University of Tennessee, Knoxville, Tennessee 37996, USA
- ⁷³Department of Physics, Tokyo Institute of Technology, Oh-okayama, Meguro, Tokyo 152-8551, Japan
- ⁷⁴Center for Integrated Research in Fundamental Science and Engineering, University of Tsukuba, Tsukuba, Ibaraki 305, Japan
- ⁷⁵Vanderbilt University, Nashville, Tennessee 37235, USA
- ⁷⁶Waseda University, Advanced Research Institute for Science and Engineering, 17 Kikui-cho, Shinjuku-ku, Tokyo 162-0044, Japan
- ⁷⁷Weizmann Institute, Rehovot 76100, Israel
- ⁷⁸Institute for Particle and Nuclear Physics, Wigner Research Centre for Physics, Hungarian Academy of Sciences (Wigner RCP, RMKI) H-1525 Budapest 114, PO Box 49, Budapest, Hungary
- ⁷⁹Yonsei University, IPAP, Seoul 120-749, Korea
- ⁸⁰University of Zagreb, Faculty of Science, Department of Physics, Bijenička 32, HR-10002 Zagreb, Croatia

(Received 5 October 2015; published 3 February 2016)

Measurements of midrapidity charged-particle multiplicity distributions, $dN_{\text{ch}}/d\eta$, and midrapidity transverse-energy distributions, $dE_T/d\eta$, are presented for a variety of collision systems and energies. Included are distributions for Au + Au collisions at $\sqrt{s_{NN}} = 200, 130, 62.4, 39, 27, 19.6, 14.5,$ and 7.7 GeV, Cu + Cu collisions at $\sqrt{s_{NN}} = 200$ and 62.4 GeV, Cu + Au collisions at $\sqrt{s_{NN}} = 200$ GeV, U + U collisions at $\sqrt{s_{NN}} = 193$ GeV, $d + \text{Au}$ collisions at $\sqrt{s_{NN}} = 200$ GeV, $^3\text{He} + \text{Au}$ collisions at $\sqrt{s_{NN}} = 200$ GeV, and $p + p$ collisions at $\sqrt{s_{NN}} = 200$ GeV. Centrality-dependent distributions at midrapidity are presented in terms of the number of nucleon participants, N_{part} , and the number of constituent quark participants, N_{qp} . For all $A + A$ collisions down to $\sqrt{s_{NN}} = 7.7$ GeV, it is observed that the midrapidity data are better described by scaling with N_{qp} than scaling with N_{part} . Also presented are estimates of the Bjorken energy density, ε_{BJ} , and the ratio of $dE_T/d\eta$ to $dN_{\text{ch}}/d\eta$, the latter of which is seen to be constant as a function of centrality for all systems.

DOI: [10.1103/PhysRevC.93.024901](https://doi.org/10.1103/PhysRevC.93.024901)

I. INTRODUCTION

Systematic measurements of the centrality dependence of transverse-energy production and charged-particle multiplicity at midrapidity provide excellent characterization of the nuclear geometry of the reaction and are sensitive to the dynamics of the colliding system. For example, measurements of $dN_{\text{ch}}/d\eta$ and $dE_T/d\eta$ in Au + Au collisions at $\sqrt{s_{NN}} = 200$ and 130 GeV as a function of centrality expressed as the number of participant nucleons, N_{part} , exhibit a nonlinear increase with increasing N_{part} . This has been explained by a two-component model proportional to a linear combination of the number of collisions, N_{coll} , and N_{part} [1,2]. In a previous study by the PHENIX collaboration, measurements of $dE_T/d\eta$ and $dN_{\text{ch}}/d\eta$ for Au + Au collisions at $200, 130,$ and 62.4 GeV are presented along with comparisons to the results of several models [3]. The models that were examined included HIJING [4], a final-state parton saturation model called EKRT [5], an initial-state parton saturation model called KLN [2], and a multiphase transport model called AMPT [6]. The comparisons showed that most models could reproduce some of the features of the data, but most failed in describing all of the data with the HIJING and AMPT models best describing the overall trends, including the nonlinear increase of $dE_T/d\eta$ and $dN_{\text{ch}}/d\eta$ as a function of N_{part} .

It was also proposed that $dN_{\text{ch}}/d\eta$ is linearly proportional to the number of constituent-quark participants without a significant contribution from a hard scattering component [7]. Recently, the PHENIX Collaboration at Brookhaven National Laboratory's Relativistic Heavy Ion Collider (RHIC) presented $dE_T/d\eta$ distributions at midrapidity for Au + Au collisions at $\sqrt{s_{NN}} = 200, 130,$ and 62.4 GeV, $d + \text{Au}$ collisions at $\sqrt{s_{NN}} = 200$ GeV, and $p + p$ collisions at $\sqrt{s_{NN}} = 200$ GeV [8]. The data are better described by a model based upon the number of constituent-quark participants than by the wounded-nucleon model [9]. Here this study is extended to include both $dE_T/d\eta$ and $dN_{\text{ch}}/d\eta$ measurements at midrapidity in Au + Au collisions down to $\sqrt{s_{NN}} = 7.7$ GeV. This study also examines the centrality dependence of $dE_T/d\eta$ and $dN_{\text{ch}}/d\eta$

for smaller systems, including Cu + Au, Cu + Cu, $d + \text{Au}$, and $^3\text{He} + \text{Au}$.

Recent lattice quantum chromodynamics (QCD) calculations indicate that the transition from quark to hadronic matter is a crossover transition at high temperature and small baryochemical potential, μ_B [10]. At high values of μ_B and low temperatures, model calculations indicate the presence of a first-order phase transition and the possibility of a critical end point in the QCD phase diagram [11]. Relativistic heavy-ion collisions serve as excellent probes of the QCD phase diagram [12]. The region of the QCD phase diagram sampled by the collisions can be controlled by changing the beam energy. Lowering the beam energy corresponds to raising the value of μ_B . From 2010 to 2014, RHIC executed a beam energy scan program to explore the QCD phase diagram, look for evidence of the phase boundaries, and search for evidence of the critical end point. Presented here are $dE_T/d\eta$ and $dN_{\text{ch}}/d\eta$ measurements from the beam energy scan as a function of centrality expressed as the number of nucleon participants, N_{part} , from Au + Au collisions at $\sqrt{s_{NN}} = 200, 130, 62.4, 39, 27, 19.6, 14.5,$ and 7.7 GeV.

Over the past 15 years, PHENIX has collected a comprehensive dataset covering a wide variety of colliding nuclei and collision energies, including the Au + Au collision beam energy scan mentioned above. Presented here are charged-particle multiplicity and transverse-energy measurements from the following systems: Au + Au collisions at $\sqrt{s_{NN}} = 200, 130, 62.4, 39, 27, 19.6, 14.5,$ and 7.7 GeV; Cu + Cu collisions at $\sqrt{s_{NN}} = 200$ and 62.4 GeV; Cu + Au collisions at $\sqrt{s_{NN}} = 200$ GeV; U + U collisions at $\sqrt{s_{NN}} = 193$ GeV; $^3\text{He} + \text{Au}$ collisions at $\sqrt{s_{NN}} = 200$ GeV; $d + \text{Au}$ collisions at $\sqrt{s_{NN}} = 200$ GeV; and $p + p$ collisions at $\sqrt{s_{NN}} = 200$ GeV. The results are discussed in the context of scaling with the number of participant nucleons (N_{part}) and the number of participant quarks (N_{qp}).

PHENIX has previously published charged-particle multiplicity distributions from Au + Au collisions at $\sqrt{s_{NN}} = 200$ GeV [3], Au + Au collisions at $\sqrt{s_{NN}} = 130$ GeV [3,13], and Au + Au collisions at $\sqrt{s_{NN}} = 19.6$ GeV [3]. PHENIX has also previously published transverse energy distributions from Au + Au collisions at $\sqrt{s_{NN}} = 200$ GeV [3], Au + Au collisions at $\sqrt{s_{NN}} = 130$ GeV [14], Au + Au collisions at $\sqrt{s_{NN}} = 62.4$ GeV [8], Au + Au collisions at $\sqrt{s_{NN}} =$

*Deceased.

†PHENIX Co-Spokesperson: morrison@bnl.gov

‡PHENIX Co-Spokesperson: jamie.nagle@colorado.edu

19.6 GeV [3], and minimum-bias distributions for $d + \text{Au}$ and $p + p$ collisions at $\sqrt{s_{NN}} = 200$ GeV [8]. Here the previously published PHENIX results are presented along with data from the many new collision systems in a consistent format to facilitate comparisons.

Similar measurements have been published by the other RHIC experiments. Charged-particle multiplicity distributions have been published by BRAHMS for Au + Au collisions at $\sqrt{s_{NN}} = 200$ and 130 GeV [15], STAR for Au + Au collisions at $\sqrt{s_{NN}} = 130$ GeV [16], and PHOBOS for Au + Au collisions at $\sqrt{s_{NN}} = 200, 130, 62.4, 56,$ and 19.6 GeV, along with Cu + Cu collisions at $\sqrt{s_{NN}} = 200$ and 62.4 GeV, $d + \text{Au}$ collisions at $\sqrt{s_{NN}} = 200$ GeV, and $p + p$ collisions at $\sqrt{s_{NN}} = 410$ and 200 GeV [17]. Transverse-energy distributions have been published by STAR for Au + Au collisions at $\sqrt{s_{NN}} = 200$ GeV [18]. Presented here are many collision systems and energies that have not been previously published by PHENIX or the other RHIC experiments, especially for the transverse-energy measurements. The first complete results on charged-particle multiplicity and transverse energy from the RHIC beam energy scan program conducted from 2010 to 2014 are also included.

This paper is organized as follows. The PHENIX detector and the methods used for centrality determination in each dataset is described in Sec. II. The analysis of the data to measure $dE_T/d\eta$ and $dN_{ch}/d\eta$ including a description of estimates of the systematic uncertainties is described in Sec. III. The centrality-dependent results at midrapidity from the Au + Au beam energy scan in terms of N_{part} are presented in Sec. IV. A description of the centrality-dependent results at midrapidity for Cu + Cu and Cu + Au collisions in terms of N_{part} are found in Sec. V. A description of the centrality-dependent results at midrapidity for U + U collisions in terms of N_{part} are found in Sec. VI. Section VII contains a description of the centrality-dependent results at midrapidity of $^3\text{He} + \text{Au}$ and $d + \text{Au}$ collisions in terms of N_{part} . A review all of the centrality-dependent results in terms of N_{qp} is presented in Sec. VIII. Section IX contains a summary of the results. Data tables for all data sets are tabulated in the Appendix.

II. THE PHENIX DETECTOR

The PHENIX detector comprises two central spectrometer arms, two muon spectrometer arms, and a set of forward detectors. All of the detector components and their performance are described elsewhere [19]. The analysis of charged-particle multiplicity utilizes detectors in the central arm spectrometer [20], including the drift chamber (DC) and pad chamber 1 (PC1) detectors. The DCs are cylindrically shaped and located radially from 2.0 to 2.4 m. The DC covers the pseudorapidity region $|\eta| < 0.35$ and 90° in azimuth for each arm. The DC has a resolution better than $150 \mu\text{m}$ in $r-\phi$, better than 2 mm in the z direction, and a two-track separation better than 1.5 mm. The PC1 detector is a multiwire proportional chamber mounted on the outer radius of the DC at 2.5 m from the beam axis. PC1 covers the full central arm acceptance. PC1 measures minimum ionizing particles with an efficiency greater than 99.5% with a position resolution of 1.7 by 3 mm and a two-track separation of 4 cm. Reconstructed tracks

from the DC with an associated hit from PC1 are counted as charged-particle tracks in the multiplicity measurement.

The analysis of transverse energy utilizes five of the lead-scintillator (PbSc) electromagnetic-calorimeter (EMCal) sectors in the central arm spectrometers [21]. Each calorimeter sector covers a pseudorapidity range of $|\eta| < 0.38$ and subtends 22.5° in azimuth for a total azimuthal coverage of 112.5° . The front face of each sector is located 5.1 m from the beam axis. Each sector contains 2592 PbSc towers arranged in a 36×72 array. Each tower has a 5.535×5.535 -cm surface area and a thickness of 0.85 nuclear interaction lengths or 18 radiation lengths. The PbSc EMCal energy resolution has been measured using test beam electrons to be $\frac{\Delta E}{E} = \frac{8.1\%}{\sqrt{E(\text{GeV})}} \oplus 2.1\%$, with a measured response proportional to the incident electron energy to within $\pm 2\%$ over the range $0.3 \leq E_e \leq 40$ GeV.

For all data sets, a minimum-bias trigger is provided by a pair of beam-beam counters (BBCs) [22]. Each BBC comprises 64 individual Čerenkov counters. Each BBC covers 2π azimuthally and a pseudorapidity range of $3.0 < |\eta| < 3.9$. For $p + p$, $d + \text{Au}$, and $^3\text{He} + \text{Au}$ collisions, an event is required to have at least one counter fire in each BBC. For all other collisions, at least two counters must fire in each BBC. The event vertex is reconstructed with a resolution of 2.0 cm in $p + p$ collisions and 0.5 mm in central Au + Au collisions using the timing information from the BBCs. All events are required to have an event vertex within 20 cm of the center of the detector.

Centrality determination in the original $\sqrt{s_{NN}} = 200$ GeV and $\sqrt{s_{NN}} = 130$ GeV Au + Au PHENIX analysis is based upon the total charge deposited in the BBCs and the total energy deposited in the zero-degree calorimeters (ZDCs) [22]. The ZDCs are a pair of hadronic calorimeters that cover the pseudorapidity range $|\eta| > 6$. For subsequent data sets taken after 2002, only the BBC information is used for the centrality determination, including the following data sets: Cu + Au at $\sqrt{s_{NN}} = 200$ GeV, Cu + Cu at $\sqrt{s_{NN}} = 200$ GeV, U + U at $\sqrt{s_{NN}} = 193$ GeV, $^3\text{He} + \text{Au}$ at $\sqrt{s_{NN}} = 200$ GeV, and $d + \text{Au}$ at $\sqrt{s_{NN}} = 200$ GeV. As the collision energy decreases, the width of the pseudorapidity distribution of produced particles becomes more narrow [23]. As a result, for energies below $\sqrt{s_{NN}} = 130$ GeV, the acceptance of the ZDC is reduced; therefore, only the BBC information is used for Au + Au collisions at $\sqrt{s_{NN}} = 62.4$ and 39 GeV and for Cu + Cu collisions at $\sqrt{s_{NN}} = 62.4$ GeV. Below $\sqrt{s_{NN}} = 39$ GeV, the BBC acceptance becomes sensitive to the presence of beam fragments, which affects the linear response of the BBC to the centrality. To avoid this nonlinear response, the reaction-plane detector (RXNP) [24] is used for the centrality determination for Au + Au collisions at $\sqrt{s_{NN}} = 7.7$ GeV, which was taken during the 2010 running period. The RXNP comprises two sets of plastic scintillators positioned on either side of the collision vertex. Each RXNP detector is arranged in 12 azimuthal segments separated into an inner and an outer ring. The RXNP has an azimuthal coverage of 2π . The pseudorapidity coverage is $1.5 < |\eta| < 2.8$ and $1.0 < |\eta| < 1.5$ for the inner and outer rings, respectively. A 2-cm-thick lead converter is located directly in front of the RXNP scintillators with

TABLE I. Summary of the data sets used in this analysis.

$\sqrt{s_{NN}}$ (GeV)	System	Year	N_{events}	Centrality	Trigger efficiency
200	Au + Au	2002	270 k	BBC + ZDC	$93 \pm 3\%$
200	Au + Au	2004	133 M	BBC + ZDC	$93 \pm 3\%$
130	Au + Au	2000	160 k	BBC + ZDC	$93 \pm 3\%$
62.4	Au + Au	2004	20 M	BBC	$86 \pm 3\%$
62.4	Au + Au	2010	12 M	BBC	$86 \pm 3\%$
39	Au + Au	2010	132 M	BBC	$86 \pm 3\%$
27	Au + Au	2011	24.5 M	PC1	$86 \pm 3\%$
19.6	Au + Au	2011	6.3 M	PC1	$86 \pm 3\%$
14.5	Au + Au	2014	6.8 M	PC1	$85 \pm 3\%$
7.7	Au + Au	2010	803 k	RXNP	$75 \pm 3\%$
200	Cu + Cu	2005	558 M	BBC	$93 \pm 3\%$
62.4	Cu + Cu	2005	175 M	BBC	$88 \pm 3\%$
200	Cu + Au	2012	2.6 B	BBC	$93 \pm 3\%$
193	U + U	2012	317 M	BBC	$93 \pm 3\%$
200	$^3\text{He} + \text{Au}$	2014	1.6 B	BBC	$88 \pm 4\%$
200	$d + \text{Au}$	2008	1.4 B	BBC	$88 \pm 4\%$
200	$p + p$	2003	14.6 M	—	$54.8 \pm 5.3\%$

respect to the collision region, which allows the RXNP to also measure contributions from neutral particles through conversion electrons. The RXNP is designed to measure the reaction-plane angle, but it can also function well as a centrality detector, because the magnitude of the total charge measured by the RXNP is dependent on the centrality of the collision. To minimize contamination from beam fragments, only the outer ring of the RXNP is used for centrality determination for Au + Au collisions at $\sqrt{s_{NN}} = 7.7$ GeV. For the 2011 data-taking period and later when the Au + Au data sets at $\sqrt{s_{NN}} = 27$, 19.6, and 14.5 GeV were collected, the RXNP was removed to install a silicon vertex detector, which was being commissioned during this time. So, for these two data sets, the multiplicity of hits in the PC1 detector were used to determine the centrality. A summary of the centrality detectors used for each dataset is included in Table I.

III. DATA ANALYSIS

Table I provides a summary of the data sets used in this analysis. For Au + Au collisions at $\sqrt{s_{NN}} = 62.4$ GeV, the $dE_T/d\eta$ analysis uses data taken in 2004 [8] and the $dN_{\text{ch}}/d\eta$ analysis uses data taken in 2010. The number of events are those events that pass the minimum-bias trigger condition for the data set and have an event vertex within 20 cm of the center of the detector.

A. Transverse energy analysis

The analysis procedure for $dE_T/d\eta$ is described in detail in Ref. [8] and summarized here. The absolute energy scale for each EMCal sector is calibrated using the π^0 mass peak from pairs of reconstructed EMCal clusters for each dataset. The transverse energy for each event was computed using clusters in the EMCal with an energy greater than 30 MeV composed of adjacent towers each with a deposited energy of more than 10 MeV. Faulty towers and all towers in a 3×3 tower area around any faulty tower are excluded from the analysis. The

transverse-energy E_T is a multiparticle variable defined as the sum

$$E_T = \sum_i E_i \sin \theta_i, \quad (1)$$

$$dE_T(\eta)/d\eta = \sin \theta(\eta) dE(\eta)/d\eta,$$

where θ_i is the polar angle, $\eta = -\ln \tan(\theta/2)$ is the pseudorapidity, E_i is by convention taken as the kinetic energy for baryons, the kinetic energy + $2 m_N$ for antibaryons, and the total energy for all other particles, where m_N is the nucleon mass. The sum is taken over all particles emitted into a fixed solid angle for each event. An example of the raw $E_{T\text{EMC}}$ distributions as a function of centrality for Au + Au collisions at $\sqrt{s_{NN}} = 14.5$ GeV are shown in Fig. 1(a).

To obtain the total hadronic E_T within a reference acceptance of $\Delta\eta = 1.0, \Delta\phi = 2\pi$ from the measured raw transverse energy, $E_{T\text{EMC}}$, the total correction can be decomposed into three main components. First is a correction by a factor of 4.188 to account for the fiducial acceptance in azimuth and pseudorapidity. Second, a correction factor is applied to account for disabled calorimeter towers not used in the analysis. Third is a factor, k , which is the ratio of the total hadronic E_T in the fiducial aperture to the measured $E_{T\text{EMC}}$. Details on the estimate of the values of the k factor are given below.

The k factor comprises three components. The first component, denoted k_{response} , is attributable to the fact that the EMCal was designed for the detection of electromagnetic particles [14]. Hadronic particles passing through the EMCal only deposit a fraction of their total energy. The average EMCal response is estimated for the various particle species using the HIJING [4] event generator for $\sqrt{s_{NN}}$ above 7.7 GeV and the URQMD [25] event generator for Au + Au collisions at $\sqrt{s_{NN}} = 7.7$ GeV. The event generator output is processed through a GEANT-based Monte Carlo simulation of the PHENIX detector. For all of the data sets, 75% of the total energy incident on the EMCal is measured; thus, $k_{\text{response}} = 1/0.75 = 1.33$.

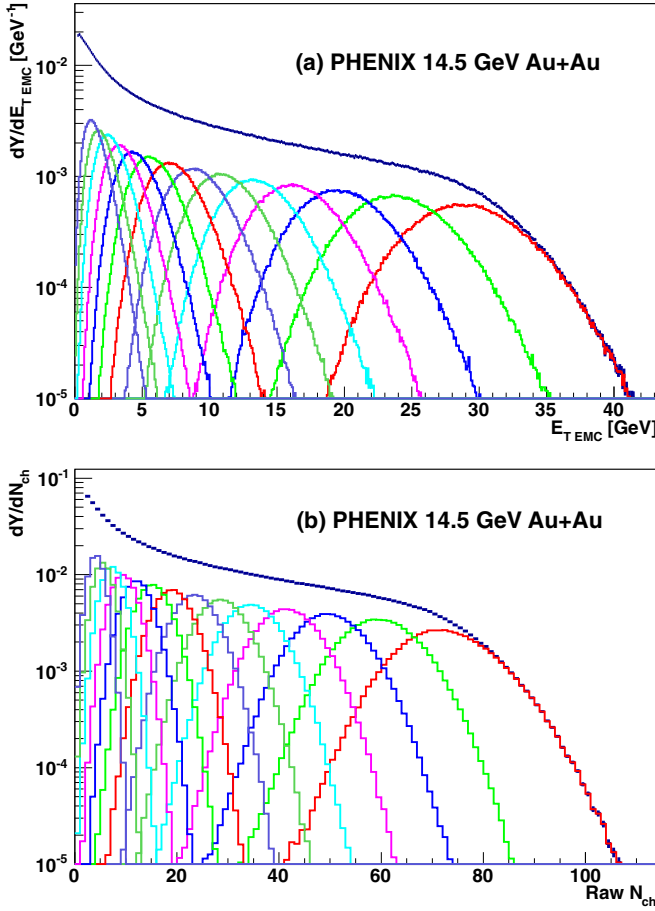


FIG. 1. Raw $E_{T\text{EMC}}$ (a) and N_{ch} (b) distributions for $\sqrt{s_{NN}} = 14.5$ GeV Au + Au collisions. Shown are the minimum-bias distribution along with the distributions in 5% wide centrality bins. All the plots are normalized so that the integral of the minimum-bias distribution is unity.

The second component of the k factor, denoted k_{inflow} , is a correction for energy inflow from outside the fiducial aperture of the EMCAL. This energy inflow has two sources: from parent particles with an original trajectory outside of the fiducial aperture whose decay products are incident within the fiducial aperture and from particles that reflect off of the PHENIX magnet poles into the EMCAL fiducial aperture. The energy inflow contribution is 24% of the measured energy; thus, $k_{\text{inflow}} = 1 - 0.24 = 0.76$. The third component of the k factor, denoted k_{losses} , is attributable to energy losses. There are three components to the energy loss: from particles with an original trajectory inside the fiducial aperture of the EMCAL whose decay products are outside of the fiducial aperture (10%), from energy losses at the edges of the EMCAL (6%), and from energy losses owing to the energy thresholds (6%). The total contribution from energy losses is 22%; thus, $k_{\text{losses}} = 1/(1 - 0.22) = 1.282$. The total k factor correction is $k = k_{\text{response}} \times k_{\text{inflow}} \times k_{\text{losses}} = 1.30$. This value varies by less than 1% for all data sets.

There are several contributions to the systematic uncertainties for the $dE_T/d\eta$ measurement which are added in quadrature to obtain the total uncertainty. These contributions

include the following: uncertainties owing to the energy response of the EMCAL, uncertainties owing to the estimate of the EMCAL acceptance, uncertainties owing to the estimate of losses and inflow, uncertainties owing to sector-by-sector variations, uncertainties owing to the noise background estimate, uncertainties owing to the trigger background estimate, and uncertainties owing to the trigger efficiency estimate. A summary of the systematic uncertainties for the $dE_T/d\eta$ analysis of each data set is listed in Table II for each data set and further explained below.

There is an uncertainty owing to the energy response of the EMCAL. This includes uncertainties in the absolute energy scale, uncertainties in the estimate of the hadronic response, uncertainties from energy losses on the EMCAL edges, and uncertainties from energy thresholds. The uncertainties in the hadronic response include a 3% uncertainty estimated using a comparison of the simulated energy deposited by hadrons with different momenta with test beam data [21] along with an additional 1% uncertainty in the particle composition and momentum distribution. There is an estimated uncertainty of 2% for the calculation of the EMCAL acceptance. There is an estimated uncertainty of 3% for the calculation of the fraction of the total energy incident on the EMCAL fiducial area (losses and inflow). There is an uncertainty owing to sector-by-sector variations in the energy measurement. There is an uncertainty owing to the noise, or background, contribution which is estimated to be consistent with zero with uncertainties determined by measuring the average energy deposited per sector in events where all the particles are screened by the central magnet pole tips by requiring an interaction z vertex of $+50 < z < +60$ cm and $-60 < z < -50$ cm. There is a centrality-dependent uncertainty for background owing to multiple interactions and trigger effects.

There is also an uncertainty in the trigger efficiency determination. The method by which the trigger efficiency is calculated is described in Ref. [3]. The BBC trigger efficiency for Au + Au collisions ranges from 93% at $\sqrt{s_{NN}} = 200$ GeV to 75% at $\sqrt{s_{NN}} = 7.7$ GeV. The trigger efficiencies for each data set are summarized in Table I. Note that the trigger inefficiency leads to a partial loss of the more peripheral collisions while the trigger is fully efficient for midcentral and central collisions. Because the centrality is defined for a given event as a percentage of the total geometrical cross section, an uncertainty in the trigger efficiency translates into an uncertainty in the centrality definition. This uncertainty is estimated by measuring the variation in $dE_T/d\eta$ by redefining the centrality using trigger efficiencies that vary by ± 1 standard deviation.

The trigger efficiency uncertainty allows for bending or inclination of the points. So, when plotting $(dE_T/d\eta)/(0.5N_{\text{part}})$ and $(dN_{\text{ch}}/d\eta)/(0.5N_{\text{part}})$, the trigger efficiency will be represented by error bands about the points within which the points can be tilted. The other systematic and statistical uncertainties are represented by error bars.

B. Charged-particle multiplicity analysis

In previous PHENIX publications [3,13] for Au + Au collisions at $\sqrt{s_{NN}} = 200$ and 130 GeV, charged-particle

TABLE II. Summary of the systematic uncertainties for the $dE_T/d\eta$ measurement for each dataset, given in percent (%). If a range is specified, the value for central collisions is listed first and the value for the most peripheral collisions presented for the data set is listed second. If no value is specified, then there is no contribution to the systematic uncertainty for that data set.

Data set	Energy response	Acceptance	Losses and inflow	Sector-by-sector	Noise	Trigger background	Trigger efficiency
200-GeV Au + Au	3.9	2.0	3.0	—	0.2–6.0	—	0.3–16.0
130-GeV Au + Au	3.8	2.0	3.0	—	0.4–10.0	—	0.3–16.0
62.4-GeV Au + Au	4.3	2.0	3.0	2.2	0.4–4.1	0.01–0.06	0.3–16.1
39-GeV Au + Au	4.5	2.0	3.0	1.6	0.5–3.6	0.002–0.02	0.2–16.3
27-GeV Au + Au	4.5	2.0	3.0	2.2	0.5–3.5	0.006–0.04	0.3–13.1
19.6-GeV Au + Au	4.7	2.0	3.0	2.8	0.5–3.5	0.008–0.07	0.3–13.4
14.5-GeV Au + Au	4.7	2.0	3.0	2.9	0.5–3.4	0.007–0.04	0.3–9.8
7.7-GeV Au + Au	4.7	2.0	3.0	3.7	0.5–3.4	0.002–0.05	0.4–10.6
200-GeV Cu + Cu	3.9	2.0	3.0	5.9	0.2–6.0	0.002–0.04	0.3–6.5
62.4-GeV Cu + Cu	4.5	2.0	3.0	2.2	0.4–4.1	0.006–0.02	0.3–8.1
200-GeV Cu + Au	3.9	2.0	3.0	2.8	0.5–3.5	0.02–0.20	0.2–8.8
193-GeV U + U	3.9	2.0	3.0	2.5	0.2–6.0	0.001–0.03	0.4–9.3
200-GeV d + Au	3.9	2.0	3.0	6.5	0.2–0.2	0.13–0.21	0.3–5.1
200-GeV ^3He + Au	3.9	2.0	3.0	3.9	0.2–0.2	0.08–0.16	0.2–5.2
200-GeV p + p	3.9	2.0	3.0	3.9	0.2	0.60	—

multiplicity was measured using cluster pairs reconstructed from the PC1 and PC3 detectors in the absence of a magnetic field. The $dN_{\text{ch}}/d\eta$ values quoted here for Au + Au collisions at $\sqrt{s_{NN}} = 200$ and 130 GeV are from the previous analyses. For all other collision species and collision energies, charged-particle multiplicity is measured using reconstructed tracks from the DC that have an unambiguous match to a reconstructed cluster in the PC1 detector with the magnetic field turned on. To remove multiple counting of incorrectly reconstructed tracks in the DC, commonly referred to as ghost tracks, a charge-dependent track proximity cut is applied. The two methods give consistent results for 200-GeV Au + Au collisions. An example of the raw N_{ch} distributions as a function of centrality for the Au + Au collisions at $\sqrt{s_{NN}} = 14.5$ GeV are shown in Fig. 1(b).

To obtain the total charged particle N_{ch} within a reference acceptance of $\Delta\eta = 1.0, \Delta\phi = 2\pi$ from the measured raw multiplicity, five corrections are applied. First is a correction of 3.74 to account for the fiducial acceptance in azimuth and pseudorapidity. The second correction is applied to account for DC and PC1 inefficiencies within the fiducial acceptance. The third correction is applied to account for particles with a transverse momentum below the 200 MeV/c minimum p_T cut applied to reconstructed tracks. This correction is determined using the average of results from the HIJING event generator [4] and the URQMD event generator [25] to estimate the fraction of the total charged particle multiplicity lying below $p_T = 200$ MeV/c. The collision energy cutoff for the HIJING event generator lies above $\sqrt{s_{NN}} = 7.7$ GeV, so only URQMD is used for Au + Au collisions at $\sqrt{s_{NN}} = 7.7$ GeV. This correction is 22% for Au + Au collisions at $\sqrt{s_{NN}} = 62.4$ GeV and 23% for Au + Au collisions at $\sqrt{s_{NN}} = 7.7$ GeV. There is an estimated 2% uncertainty for this correction. The fourth correction is a centrality-dependent correction for the track reconstruction efficiency.

The last correction is an in-flight decay correction that accounts for particle decays after the collision interaction

that can add or remove charged particles from the measured multiplicity. This includes primary charged particles that decay and miss the detector. It also includes feed-down from neutral primary particle decays that go into the detector. This correction is determined by processing simulated events from the HIJING [4] event generator for $\sqrt{s_{NN}}$ above 7.7 GeV and the URQMD [25] event generator at $\sqrt{s_{NN}} = 7.7$ GeV. Below $\sqrt{s_{NN}} = 62.4$ GeV, results from the two event generators are consistent with each other within the uncertainties. The event generator output is processed through a GEANT-based simulation of the PHENIX detector response. For Au + Au collisions, this correction varies from 0.99 at $\sqrt{s_{NN}} = 200$ GeV to 1.061 at $\sqrt{s_{NN}} = 7.7$ GeV. The energy dependence is primarily attributable to the decrease of the particle momenta and the narrowing of the width of the η distribution at lower energies that affects the number of tracks from the decay of particles coming from comparable rapidities.

There are several contributions to the systematic uncertainties for the $dN_{\text{ch}}/d\eta$ measurement which are added in quadrature to obtain the total uncertainty. A summary of the systematic uncertainties for the $dN_{\text{ch}}/d\eta$ analysis for all data sets is listed in Table III. There is an estimated uncertainty of 4% for the acceptance correction. There is an uncertainty for the estimate of the correction for in-flight decays that varies from 2.9% at $\sqrt{s_{NN}} = 200$ GeV to 5.9% at $\sqrt{s_{NN}} = 7.7$ GeV. There is a 2% uncertainty for the estimate of charged-particle multiplicity for low p_T below 200 MeV/c. There is a centrality-dependent uncertainty owing to the occupancy of the PC1 detector that varies from 3.5% to 1.2% for Au + Au central collisions from $\sqrt{s_{NN}} = 200$ to 7.7 GeV. There is an estimated 5% uncertainty for the tracking efficiency estimate. There is a centrality-dependent uncertainty for background owing to trigger effects and multiple interactions. Finally, there is an uncertainty for the determination of the trigger efficiency, which is estimated in the same manner as for the $dE_T/d\eta$ analysis.

TABLE III. Summary of the systematic uncertainties for charged-particle multiplicity for each data set given in percent (%). If a range is specified, the value for central collisions is listed first and the value for the most peripheral collisions presented for the data set is listed second. If no value is specified, then there is no contribution to the systematic uncertainty for that data set.

Data set	Acceptance	Decays	Low p_T	Occupancy	Tracking efficiency	Trigger background	Trigger efficiency
200-GeV Au + Au	2.3	2.9	2.0	3.5–0.10	—	1.0	0.3–16.0
130-GeV Au + Au	2.5	2.5	2.0	3.1–0.10	—	1.0	0.3–16.0
62.4-GeV Au + Au	4.0	5.0	2.0	3.5–0.10	5.0	0.001–0.03	0.2–16.1
39-GeV Au + Au	4.0	5.4	2.0	3.0–0.03	5.0	0.001–0.009	0.2–13.0
27-GeV Au + Au	4.0	5.6	2.0	2.0–0.01	5.0	0.01–0.03	0.2–13.3
19.6-GeV Au + Au	4.0	5.7	2.0	1.9–0.01	5.0	0.002–0.003	0.2–9.3
14.5-GeV Au + Au	4.0	5.8	2.0	1.9–0.01	5.0	0.001–0.007	0.3–9.8
7.7-GeV Au + Au	4.0	5.9	2.0	1.2–0.01	5.0	0.001–0.03	0.4–12.3
200-GeV Cu + Cu	4.0	2.9	2.0	1.5–0.01	5.0	0.03–0.08	0.3–8.0
62.4-GeV Cu + Cu	4.0	5.0	2.0	1.0–0.01	5.0	0.02–0.01	0.3–9.2
200-GeV Cu + Au	4.0	2.9	2.0	2.6–0.05	5.0	0.001–0.07	0.9–10.1
193-GeV U + U	4.0	2.9	2.0	3.5–0.10	5.0	0.001–0.01	0.4–9.3
200-GeV d + Au	4.0	2.9	2.0	0.1–0.01	5.0	0.001–0.001	0.3–7.2
200-GeV ^3He + Au	4.0	2.9	2.0	0.1–0.01	5.0	0.001–0.001	0.2–6.5
200-GeV p + p	4.0	2.9	2.0	0.01	5.0	0.0015	—

IV. Au + Au BEAM ENERGY SCAN RESULTS

This section presents $dE_T/d\eta$ and $dN_{\text{ch}}/d\eta$ measurements as a function of centrality expressed as the number of nucleon participants, N_{part} , from the RHIC beam energy scan that includes Au + Au collisions at $\sqrt{s_{NN}} = 200, 130, 62.4, 39, 27, 19.6, 14.5,$ and 7.7 GeV. A Monte Carlo Glauber model calculation is used to obtain estimates of N_{part} as a function of centrality using the procedure outlined in Ref. [26]. At each collision energy, the Glauber model is run using the inelastic nucleon-nucleon cross sections, $\sigma_{nn}^{\text{inel}}$, listed in Table IV.

When plotting $dE_T/d\eta$ and $dN_{\text{ch}}/d\eta$, systematic uncertainties are decomposed into two types. Type A uncertainties include point-to-point uncertainties that are uncorrelated between bins and include only statistical uncertainties in this analysis. The remaining uncertainties are classified as type B uncertainties that are correlated bin-by-bin such that all points move in the same direction, but not necessarily by the same factor. Because the magnitudes of the type A statistical uncertainties are small compared to the magnitudes of the type B uncertainties, the error bars in the plots presented below will represent the total statistical and systematic uncertainties added in quadrature. The trigger efficiency uncertainty is

represented separately by error bands bounding the points within which the points can be tilted, as described in Sec. III.

Examining the N_{part} dependence of $dE_T/d\eta$ and $dN_{\text{ch}}/d\eta$ normalized by the number of nucleon participant pairs at midrapidity is useful to determine if the data scales by N_{part} and if the scaling changes as a function of $\sqrt{s_{NN}}$. The results for Au + Au collisions for all beam energies at midrapidity are shown in Fig. 2 as a function of N_{part} . For all energies, $dE_T/d\eta$ and $dN_{\text{ch}}/d\eta$ do not scale with N_{part} ; the magnitudes of $dE_T/d\eta$ and $dN_{\text{ch}}/d\eta$ increase as N_{part} increases. It has been previously observed that the shape of the distributions as a function of N_{part} are preserved in Au + Au collisions from $\sqrt{s_{NN}} = 200$ GeV to $\sqrt{s_{NN}} = 19.6$ GeV [3,23]. Figure 3(a) shows the ratio of $(dE_T/d\eta)/(0.5N_{\text{part}})$ from Au + Au collisions at $\sqrt{s_{NN}} = 200$ GeV to $\sqrt{s_{NN}} = 7.7$ GeV, illustrating that the shapes of the distributions are preserved down to $\sqrt{s_{NN}} = 7.7$ GeV. Figure 3(b) shows the same for $(dN_{\text{ch}}/d\eta)/(0.5N_{\text{part}})$. Previous measurements in fixed target h + A collisions showed that the total charged-particle multiplicity does scale well as a function of N_{part} in the range of $10 \leq \sqrt{s_{NN}} \leq 20$ GeV [27]. However, this measurement was made over the full rapidity range rather than at midrapidity. For the midrapidity measurements presented here, the N_{part} scaling behavior does not change significantly from $\sqrt{s_{NN}} = 200$ GeV down to $\sqrt{s_{NN}} = 7.7$ GeV.

Excitation functions of $(dE_T/d\eta)/(0.5N_{\text{part}})$ and $(dN_{\text{ch}}/d\eta)/(0.5N_{\text{part}})$ are shown in Fig. 4. Shown are the PHENIX data along with results from other experiments. The data points for the lower energies are from estimates described in Ref. [3]. For $(dE_T/d\eta)/(0.5N_{\text{part}})$, data are shown from FOPI 0%–1% centrality Au + Au collisions [28], E802 0%–5% centrality Au + Au collisions [29], NA49 0%–7% centrality Pb + Pb collisions [30,31], STAR 0%–5% centrality Au + Au collisions [18], and CMS 0%–5% centrality Pb + Pb collisions [31]. For $(dN_{\text{ch}}/d\eta)/(0.5N_{\text{part}})$, data are shown from FOPI [28], E802 [29,32,33], NA49 [30], STAR [18,34], PHOBOS 0%–3% centrality Au + Au

TABLE IV. Summary of the cross sections as a function of $\sqrt{s_{NN}}$.

Energy	σ_{nn}^{tot} (mb)	$\sigma_{nn}^{\text{inel}}$ (mb)	$\sigma_{qq}^{\text{inel}}$ (mb)
200	52.5	42.3	8.17
130	48.7	39.6	7.54
62.4	43.6	36.0	6.56
39	41.2	34.3	6.15
27	39.8	33.2	5.86
19.6	39.0	32.5	5.70
15.0	38.5	32.0	5.58
7.7	38.6	31.2	5.35

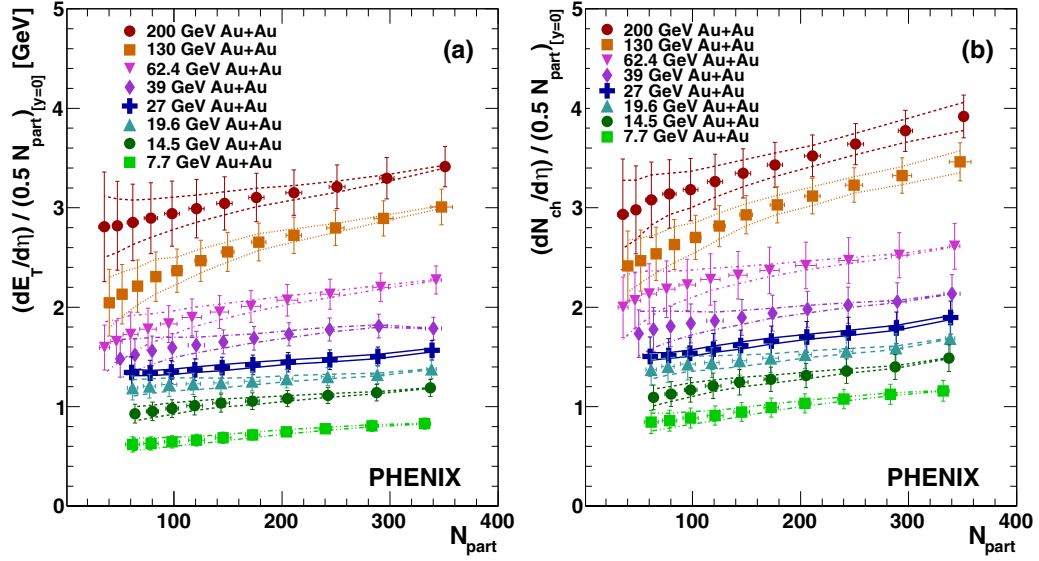


FIG. 2. $(dE_T/d\eta)/(0.5N_{\text{part}})$ (a) and $(dN_{\text{ch}}/d\eta)/(0.5N_{\text{part}})$ (b) at midrapidity as a function of N_{part} for Au + Au collisions 200, 130, 62.4, 39, 27, 19.6, 14.5, and 7.7 GeV. The lines bounding the points represent the trigger efficiency uncertainty within which the points can be tilted. The error bars represent the remaining total statistical and systematic uncertainty.

collisions [17], ALICE 0%–5% centrality Pb + Pb collisions [35], and ATLAS [36] Pb + Pb collisions interpolated to 0%–5% centrality. The data are plotted on a log-log scale to illustrate the power law behavior of both $(dE_T/d\eta)/(0.5N_{\text{part}})$ and $(dN_{\text{ch}}/d\eta)/(0.5N_{\text{part}})$ as a function of $\log(\sqrt{s_{NN}})$ for $\sqrt{s_{NN}}$ at or above 7.7 GeV. For $(dE_T/d\eta)/(0.5N_{\text{part}})$, the data between $\sqrt{s_{NN}} = 7.7$ and 200 GeV are described by $(dE_T/d\eta)/(0.5N_{\text{part}})(\sqrt{s_{NN}}) \propto e^{b \times \log(\sqrt{s_{NN}})}$, where $b = 0.428 \pm 0.021$. For $(dN_{\text{ch}}/d\eta)/(0.5N_{\text{part}})$, the data between $\sqrt{s_{NN}} = 7.7$ and 200 GeV are described by $(dN_{\text{ch}}/d\eta)/(0.5N_{\text{part}})(\sqrt{s_{NN}}) \propto e^{b \times \log(\sqrt{s_{NN}})}$, where $b = 0.374 \pm 0.028$. The data deviate from the power-law behavior below the lowest PHENIX measurement at $\sqrt{s_{NN}} = 7.7$ GeV.

The ratio of $dE_T/d\eta$ to $dN_{\text{ch}}/d\eta$, referred to here simply as E_T/N_{ch} , is a variable that is related to the average transverse mass of the produced particles [3]. In previous measurements, this ratio has been observed to be independent of centrality and independent of $\sqrt{s_{NN}}$ in Au + Au collisions from $\sqrt{s_{NN}} = 200$ to 19.6 GeV [3]. Figure 5 plots the E_T/N_{ch} ratio as a function of N_{part} for Au + Au collisions at various values of $\sqrt{s_{NN}}$. For all cases, the ratio is constant with N_{part} within the systematic uncertainties. The excitation function of E_T/N_{ch} is shown in Fig. 6. Here the Large Hadron Collider point has been obtained by taking the ratio of the CMS $dE_T/d\eta$ data [31] with the average of the ALICE [35] and ATLAS [36] data. The ratio increases below $\sqrt{s_{NN}} \approx 10$ GeV, levels off, and then increases at $\sqrt{s_{NN}} = 200$ GeV.

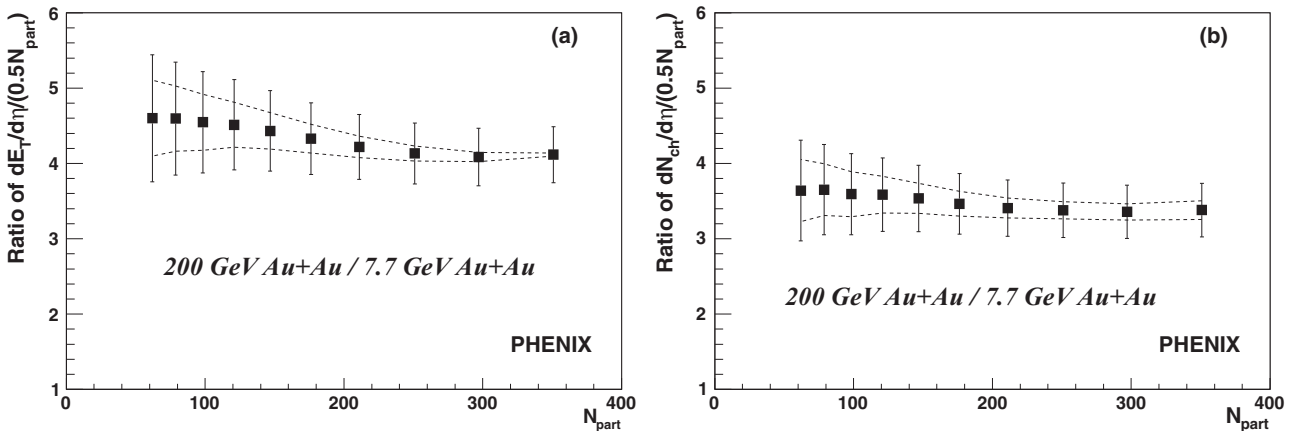


FIG. 3. The ratio of $\sqrt{s_{NN}} = 200$ GeV Au + Au collisions to $\sqrt{s_{NN}} = 7.7$ GeV Au + Au collisions for $(dE_T/d\eta)/(0.5N_{\text{part}})$ (a) and for $(dN_{\text{ch}}/d\eta)/(0.5N_{\text{part}})$ (b). The lines bounding the points represent the trigger efficiency uncertainty within which the points can be tilted. The error bars represent the total statistical and systematic uncertainties.

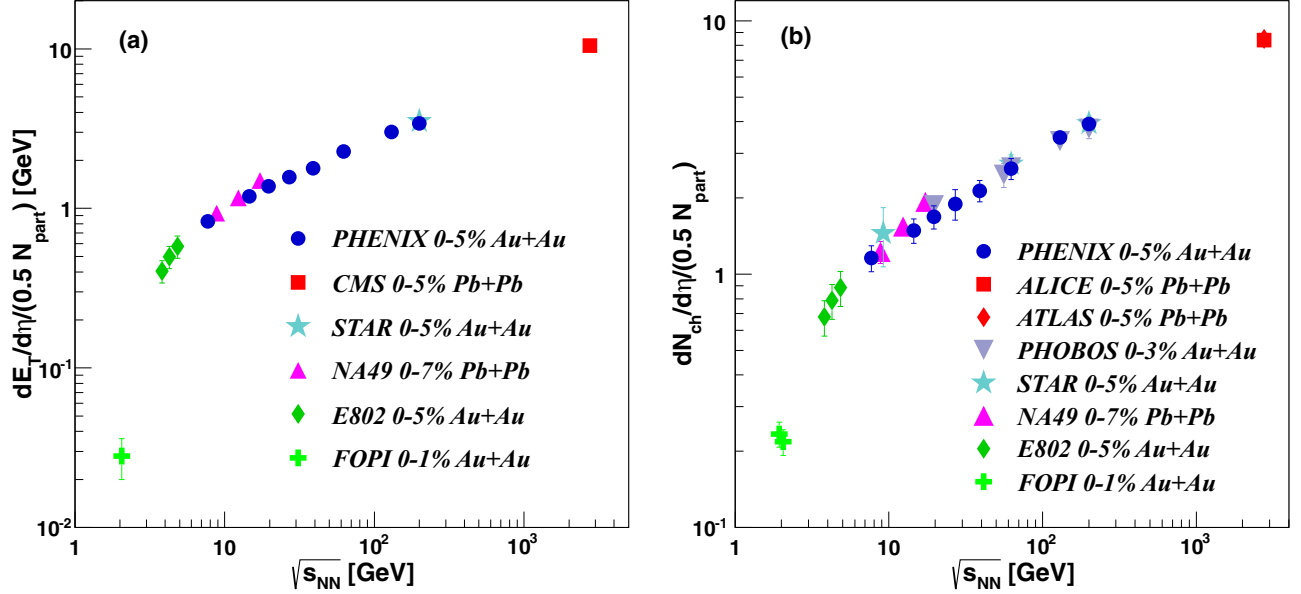


FIG. 4. The excitation function of $(dE_T/d\eta)/(0.5N_{\text{part}})$ (a) and $(dN_{\text{ch}}/d\eta)/(0.5N_{\text{part}})$ (b) for central collisions at midrapidity as a function of $\sqrt{s_{NN}}$. The error bars represent the total statistical and systematic uncertainties. For $(dE_T/d\eta)/(0.5N_{\text{part}})$ (a), data are shown from FOPI [28], E802 [29], NA49 [30,31], STAR [18], and CMS [31]. For $(dN_{\text{ch}}/d\eta)/(0.5N_{\text{part}})$ (b), data are shown from FOPI [28], E802 [29,32,33], NA49 [30], STAR [18,34], PHOBOS [17], ALICE [35], and ATLAS [36].

The energy density per unit volume in nuclear collisions can be estimated from the energy density per unit rapidity [37]. The Bjorken energy density can be calculated as

$$\varepsilon_{BJ} = \frac{1}{A_{\perp}\tau} J(y,\eta) \frac{dE_T}{d\eta}, \quad (2)$$

where A_{\perp} is the transverse overlap area of the nuclei determined from the Glauber model, τ is the formation time, and $J(y,\eta)$ is the Jacobian factor for converting pseudorapidity to rapidity.

The Jacobian factor depends on the momentum distributions of the produced particles, which are dependent on the beam energy. The Jacobian factor for each beam energy in the PHENIX acceptance has been estimated using the URQMD event generator, which well reproduces measured particle spectra over the RHIC beam energy range and, unlike HIJING, is valid at $\sqrt{s_{NN}} = 7.7$ GeV. Calculations of the Jacobian factor using URQMD are consistent with previous calculations using the HIJING event generator [3]. There is an estimated uncertainty of 3% for this calculation for all beam energies. The values of the Jacobian factors are summarized in Table V.

The transverse overlap area is estimated using a Monte Carlo Glauber model as $A_{\perp} \sim \sigma_x \sigma_y$, where σ_x and σ_y are the widths of the x - and y -position distributions of the participating nucleons in the transverse plane. A normalization to πR^2 , where R is the sum of the radius (r_n) and surface diffuseness (a) parameters of the Woods-Saxon parametrization,

$$\rho(r) = 1/(1 + e^{(r-r_n)/a}), \quad (3)$$

of the nuclear density profile, $\rho(r)$, was applied for the most central collisions at impact parameter $b = 0$.

A compilation of the Bjorken energy density multiplied by τ for Au + Au collisions at various collision energies is shown

in Fig. 7. The value of ε_{BJ} increases with increasing $\sqrt{s_{NN}}$ and also with increasing N_{part} . The value of ε_{BJ} for the most central Au + Au collisions at $\sqrt{s_{NN}} = 7.7$ GeV is 1.36 ± 0.14 , which is still above the value of 1.0 for a formation time of 1 fm/c that had been the proposed value above which the quark-gluon plasma can be formed in Bjorken's original paper [37]. It is also above the result of 0.7 ± 0.3 GeV/fm³ for the critical energy density obtained from lattice QCD calculations [38,39]. The excitation function of ε_{BJ} multiplied by τ is shown in Fig. 8. The results are shown on a log-log scale to illustrate that ε_{BJ} follows a power-law behavior from $\sqrt{s_{NN}} = 7.7$ GeV up to $\sqrt{s_{NN}} = 2760$ GeV, $\varepsilon_{BJ}\tau \propto e^{b \times \log(\sqrt{s_{NN}})}$, where $b = 0.422 \pm 0.035$.

V. RESULTS FOR Cu + Au AND Cu + Cu COLLISIONS

Measurements of $dN_{\text{ch}}/d\eta$ in systems lighter than Au have been published by PHOBOS for 200- and 62.4-GeV Cu + Cu collisions [17], showing that the Cu + Cu $dN_{\text{ch}}/d\eta$ distribution as a function of N_{part} exhibits similar features when compared to Au + Au collisions. Here those measurements are extended to include measurements of $dE_T/d\eta$ and the addition of measurements from the asymmetric Cu + Au system at $\sqrt{s_{NN}} = 200$ GeV.

Figure 9 shows $(dE_T/d\eta)/(0.5N_{\text{part}})$ and $(dN_{\text{ch}}/d\eta)/(0.5N_{\text{part}})$ at midrapidity as a function of N_{part} for Cu + Cu and Cu + Au collisions. Also shown for comparison are the data for Au + Au collisions at $\sqrt{s_{NN}} = 200$ GeV. Both plots exhibit the trend established in Au + Au collisions of increasing $(dE_T/d\eta)/(0.5N_{\text{part}})$ and $(dN_{\text{ch}}/d\eta)/(0.5N_{\text{part}})$ with increasing N_{part} and increasing $\sqrt{s_{NN}}$. The Cu + Cu and Cu + Au distributions at $\sqrt{s_{NN}} = 200$ GeV are consistent with each other within the uncertainties of the measurement. All of

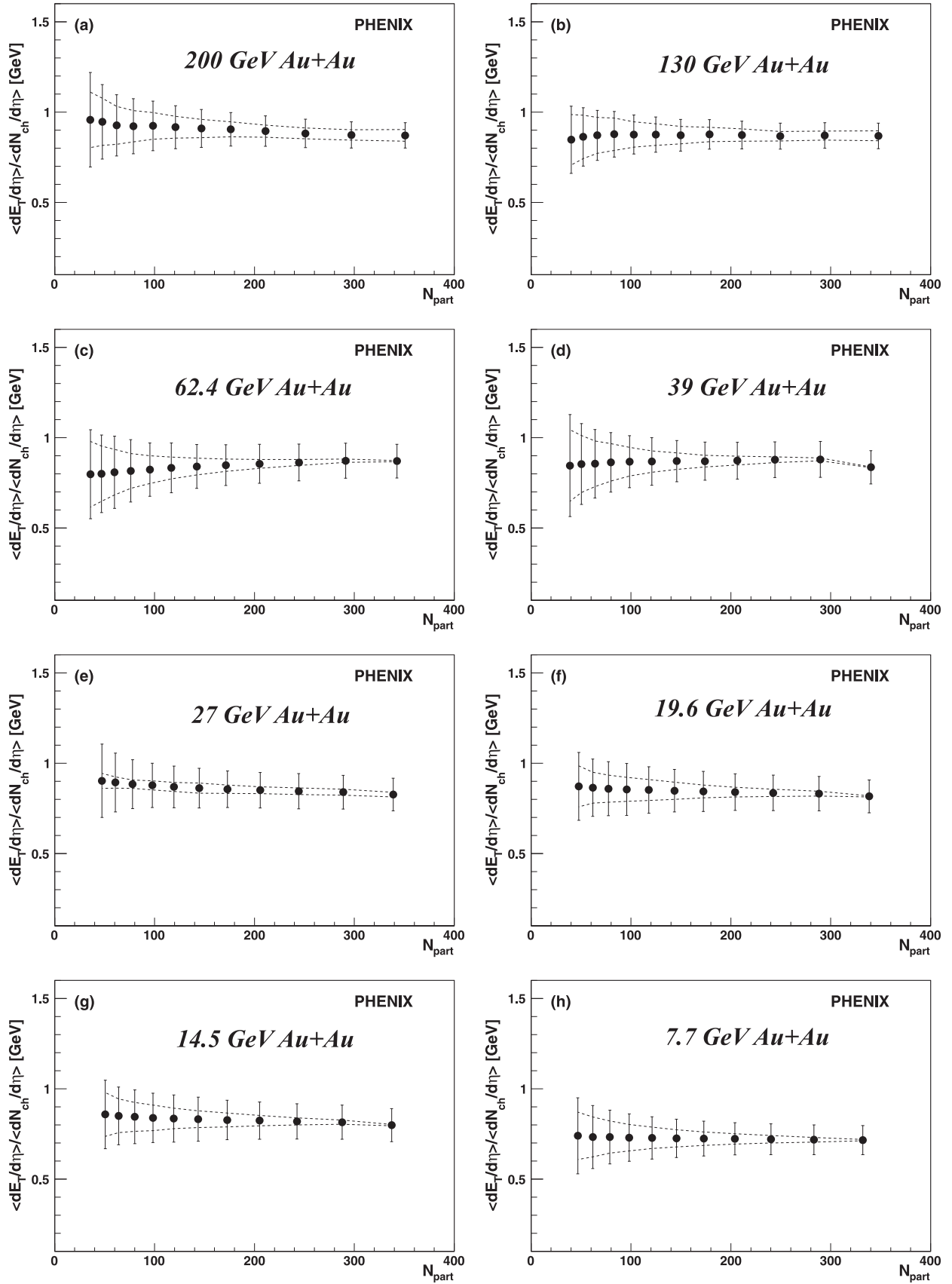


FIG. 5. The E_T/N_{ch} ratio as a function of N_{part} for Au + Au collisions at varying values of $\sqrt{s_{NN}}$. The lines bounding the points represent the trigger efficiency uncertainty within which the points can be tilted. The error bars represent the total statistical and systematic uncertainties.

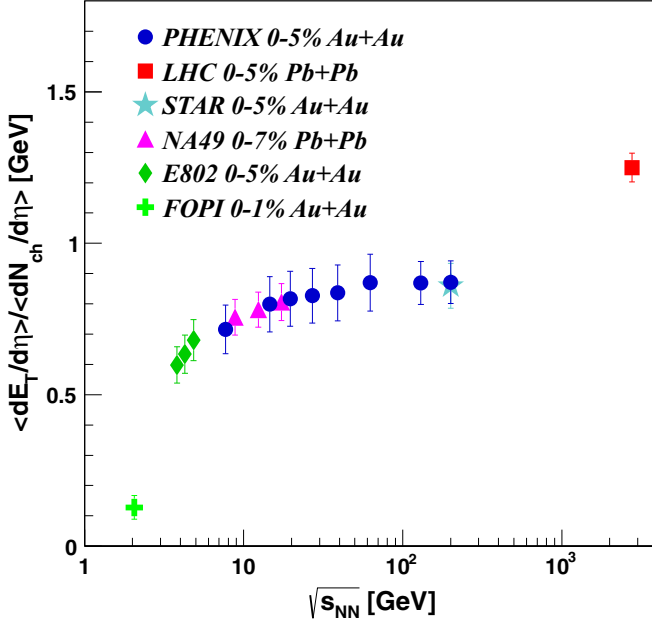


FIG. 6. The E_T/N_{ch} ratio as a function of $\sqrt{s_{NN}}$ for central Au + Au collisions and Pb + Pb collisions at midrapidity. The error bars represent the total statistical and systematic uncertainties. The Large Hadron Collider, LHC, data point has been obtained by taking the ratio of the CMS $dE_T/d\eta$ data [31] with the average of the ALICE [35] and the ATLAS [36] data. For $(dE_T/d\eta)/(0.5N_{part})$, data are taken from FOPI [28], E802 [29], NA49 [30,31], STAR [18], and CMS [31]. For $(dN_{ch}/d\eta)/(0.5N_{part})$, data are taken from FOPI [28], E802 [29,32,33], NA49 [30], STAR [18,34], PHOBOS [17], ALICE [35], and ATLAS [36].

the species (Au + Au, Cu + Au, and Cu + Cu) at $\sqrt{s_{NN}} = 200$ GeV are consistent with each other for all overlapping values of N_{part} . This behavior had been previously noted when comparing Au + Au and Cu + Cu data from PHOBOS [40] and is now extended to include Cu + Au collisions. Figure 10 shows that, as in the Au + Au collisions, the E_T/N_{ch} ratio in the lighter colliding system is consistent with being independent of N_{part} .

Figure 11 shows the N_{part} dependence of ϵ_{BJ} multiplied by τ for Cu + Cu and Cu + Au collisions. Both the Cu + Cu data at $\sqrt{s_{NN}} = 200$ GeV and the Cu + Cu data at $\sqrt{s_{NN}} = 62.4$ GeV increase with increasing N_{part} . For all values

TABLE V. Summary of the Jacobian scale factor estimated for each beam energy.

Dataset	$J(y, \eta)$
200-GeV Au + Au	1.25
130-GeV Au + Au	1.25
62.4-GeV Au + Au	1.25
39-GeV Au + Au	1.27
27-GeV Au + Au	1.27
19.6-GeV Au + Au	1.28
14.5-GeV Au + Au	1.30
7.7-GeV Au + Au	1.35

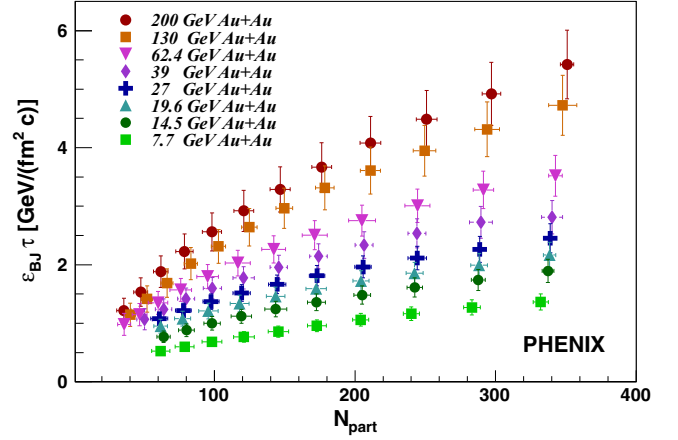


FIG. 7. The Bjorken energy density, ϵ_{BJ} , multiplied by τ as a function of N_{part} for Au + Au collisions at varying values of $\sqrt{s_{NN}}$. The error bars represent the total statistical and systematic uncertainties.

of N_{part} , ϵ_{BJ} for Cu + Cu collisions at $\sqrt{s_{NN}} = 200$ GeV and Cu + Au at $\sqrt{s_{NN}} = 200$ GeV are consistent with each other within the uncertainties of the measurement. With the different collision geometries taken into account, there is a more consistent agreement between the most central Cu + Cu and Cu + Au data points at $\sqrt{s_{NN}} = 200$ GeV than with $(dE_T/d\eta)/(0.5N_{part})$ alone. Also shown for comparison are the ϵ_{BJ} values for Au + Au collisions at $\sqrt{s_{NN}} = 200$ and 62.4 GeV, illustrating that ϵ_{BJ} is independent of the size of the system.

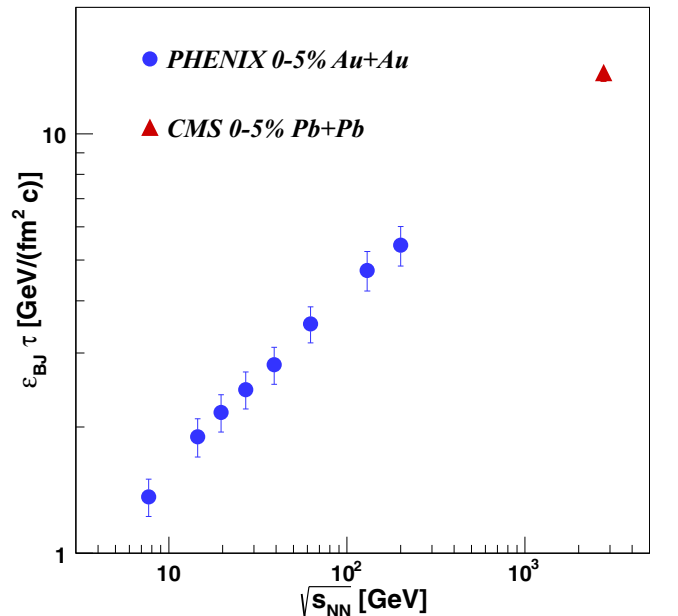


FIG. 8. The Bjorken energy density, ϵ_{BJ} , multiplied by τ as a function of $\sqrt{s_{NN}}$ for central Au + Au (PHENIX) and Pb + Pb (CMS) [31] collisions at midrapidity. The error bars represent the total statistical and systematic uncertainties.

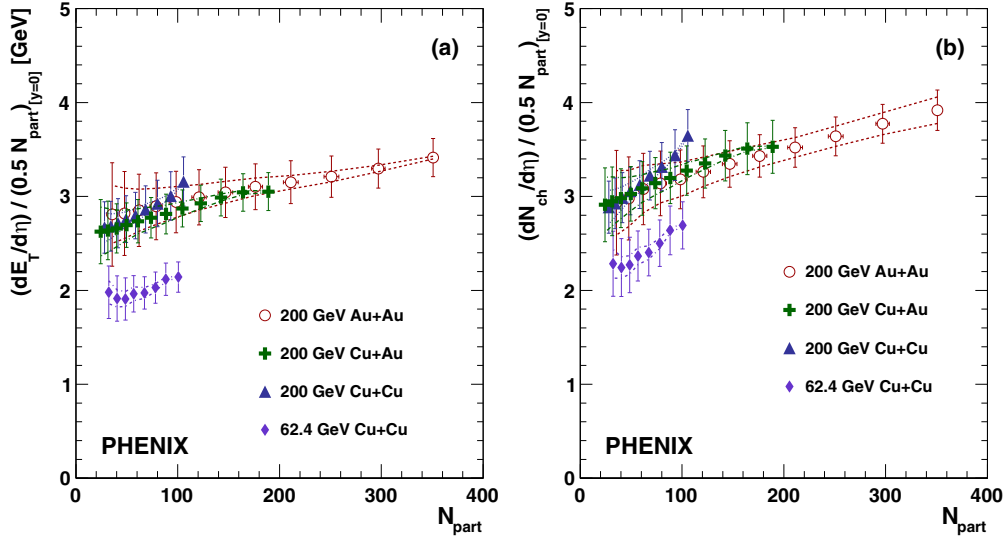


FIG. 9. $(dE_T/d\eta)/(0.5N_{\text{part}})$ (a) and $(dN_{\text{ch}}/d\eta)/(0.5N_{\text{part}})$ (b) at midrapidity as a function of N_{part} for Cu + Cu and Cu + Au collisions. Also shown are results from Au + Au collisions at $\sqrt{s_{NN}} = 200$ GeV for comparison. The lines bounding the points represent the trigger efficiency uncertainty within which the points can be tilted. The error bars represent the remaining total statistical and systematic uncertainty.

VI. RESULTS FOR U + U COLLISIONS

During the 2012 data-taking period, RHIC delivered U + U collisions at $\sqrt{s_{NN}} = 193$ GeV. U + U collisions can provide additional information about the dynamics of the system [41–44] by varying the collision geometry of the nonspherical prolate uranium nuclei [45]. However, for this study, there is no collision geometry selection applied to the data. The results presented here are integrated over all orientations of the colliding nuclei.

The estimate of N_{part} as a function of centrality for U + U collisions is made using the method described previously. However, the U + U collisions are now modeled in the Glauber Monte Carlo calculation using a deformed Woods-Saxon distribution for the uranium nucleus to describe its prolate shape,

$$\rho(r) = \rho_0 / (1 + e^{(r-R')/a}), \quad (4)$$

where ρ_0 is the normal nuclear density, a is the surface diffuseness parameter, and R' is a θ -dependent description of the nuclear radius,

$$R' = R[1 + \beta_2 Y_2^0(\theta) + \beta_4 Y_4^0(\theta)], \quad (5)$$

where Y^0 is a Legendre polynomial. The Woods-Saxon parameters used are taken from a previous study with $R = 6.81$ fm, $a = 0.6$ fm, $\beta_2 = 0.28$, and $\beta_4 = 0.093$ [46]. There is an additional study that presents a different set of parameters ($R = 6.86$ fm, $a = 0.42$ fm, $\beta_2 = 0.265$, and $\beta_4 = 0$) [47]. The two parametrizations result in N_{part} estimates that are consistent within the uncertainties, so the N_{part} values quoted here are from the former parametrization [46].

Figure 12 shows $(dE_T/d\eta)/(0.5N_{\text{part}})$ and $(dN_{\text{ch}}/d\eta)/(0.5N_{\text{part}})$ at midrapidity as a function of N_{part} for U + U collisions at $\sqrt{s_{NN}} = 193$ GeV. Also shown for comparison are the data for Au + Au collisions at

$\sqrt{s_{NN}} = 200$ GeV. Both the U + U and the Au + Au data are consistent with each other for all values of N_{part} . This behavior is also observed when comparing Au + Au, Cu + Au, and Cu + Cu data as discussed in the previous section.

VII. RESULTS FOR DEUTERON + Au AND ^3He + Au COLLISIONS

Measurements of $dN_{\text{ch}}/d\eta$ have been published by PHOBOS for $d + \text{Au}$ collisions at $\sqrt{s_{NN}} = 200$ GeV [17]. Here those measurements are extended to include measurements of $dE_T/d\eta$ and the addition of measurements from $^3\text{He} + \text{Au}$ collisions at $\sqrt{s_{NN}} = 200$ GeV.

A detailed description of the method used to define the centrality of 200 GeV $d + \text{Au}$ collisions using the PHENIX detector can be found elsewhere [48]. The same method was applied to define the centrality in $^3\text{He} + \text{Au}$ collisions. Figure 13 shows $(dE_T/d\eta)/(0.5N_{\text{part}})$ and $(dN_{\text{ch}}/d\eta)/(0.5N_{\text{part}})$ as a function of N_{part} for $d + \text{Au}$ and $^3\text{He} + \text{Au}$ collisions. Also shown are the most peripheral Au + Au points at $\sqrt{s_{NN}} = 200$ GeV for comparison. Within the uncertainties, the results for 200-GeV $d + \text{Au}$ and $^3\text{He} + \text{Au}$ collisions are consistent with each other for all values of N_{part} . As with the heavier systems, the E_T/N_{ch} ratio is consistent with being independent of N_{part} within the uncertainties of the measurement as shown in Fig. 14.

For minimum-bias $p + p$ collisions at $\sqrt{s_{NN}} = 200$ GeV, $(dE_T/d\eta)/(0.5N_{\text{part}})$ is 2.27 ± 0.19 GeV and $(dN_{\text{ch}}/d\eta)/(0.5N_{\text{part}})$ is 2.38 ± 0.17 , where the uncertainties represent the total statistical and systematic uncertainties. These measurements are consistent with the most peripheral results from both $^3\text{He} + \text{Au}$ and $d + \text{Au}$ collisions. The $(dN_{\text{ch}}/d\eta)/(0.5N_{\text{part}})$ measurement is also consistent with the PHOBOS measurement [17].

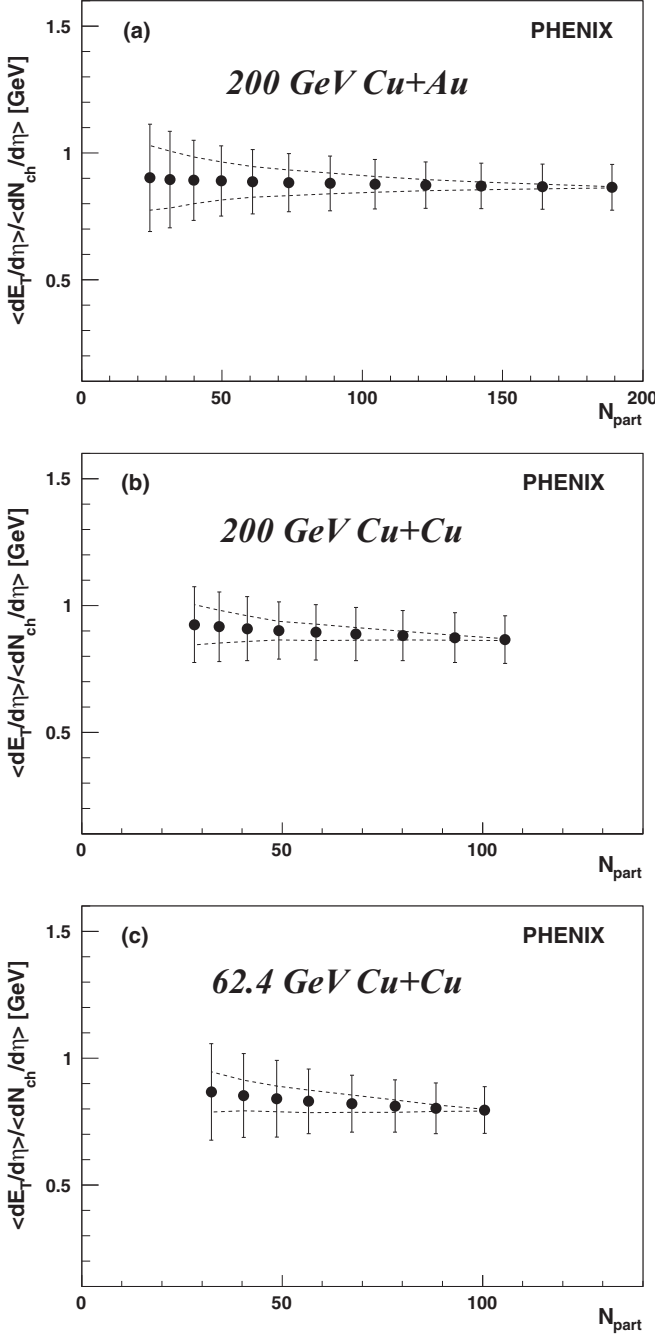


FIG. 10. The E_T/N_{ch} ratio as a function of N_{part} for Cu + Au collisions at $\sqrt{s_{NN}} = 200$ GeV (a), Cu + Cu collisions at $\sqrt{s_{NN}} = 200$ GeV (b), and Cu + Cu collisions at $\sqrt{s_{NN}} = 62.4$ GeV (c). The lines bounding the points represent the trigger efficiency uncertainty within which the points can be tilted. The error bars represent the total statistical and systematic uncertainties.

VIII. QUARK PARTICIPANT SCALING AT MIDRAPIDITY

Thus far, $dE_T/d\eta$ and $dN_{ch}/d\eta$ have been discussed in terms of the dependence on the number of nucleon participants in the collision. Here the behavior as a function of the number of quark participants, N_{qp} , will be examined. PHOBOS $dN_{ch}/d\eta$ data for Au + Au collisions at $\sqrt{s_{NN}} = 200$ and

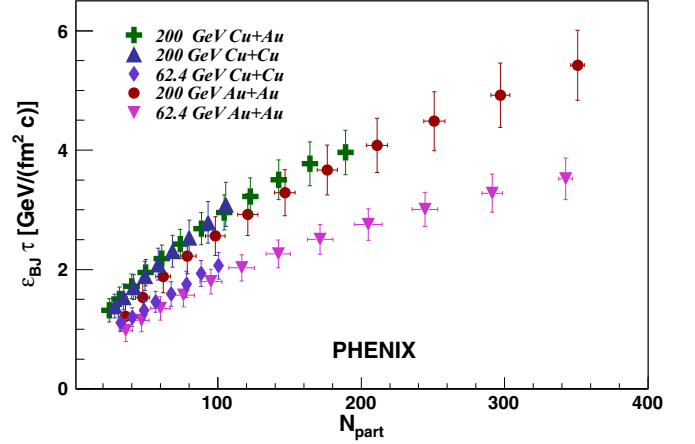


FIG. 11. The Bjorken energy density, ϵ_{BJ} , multiplied by τ as a function of N_{part} for Cu + Cu, Cu + Au, and Au + Au collisions. The error bars represent the total statistical and systematic uncertainties.

130 GeV have been analyzed as a function of N_{qp} [7]. This analysis shows that the data at midrapidity are better described by scaling with N_{qp} than with N_{part} at the top RHIC energies. A separate analysis of the PHOBOS $dN_{ch}/d\eta$ data for Au + Au collisions extended down to $\sqrt{s_{NN}} = 62.4$ and 19.6 GeV in terms of N_{qp} [40] concludes that N_{qp} scaling better describes the data than N_{part} scaling at those lower energies. PHENIX compared various models of particle production and verified that N_{qp} scaling best describes the midrapidity $dE_T/d\eta$ measurements in Au + Au collisions at $\sqrt{s_{NN}} = 200$ and 62.4 GeV [8]. Here these analyses are extended to include $dE_T/d\eta$ and $dN_{ch}/d\eta$ measurements down to $\sqrt{s_{NN}} = 7.7$ GeV.

The number of quark participants is estimated using a Monte Carlo Glauber model calculation method [26] that has been modified to replace nucleons with constituent quarks [8]. The nuclei are initially assembled by distributing the centers of the nucleons according to a Woods-Saxon distribution. After a nucleus is fully assembled, the nucleons are replaced by three quarks distributed around the center of each nucleon. The quarks are distributed radially by sampling an empirically determined function,

$$f(r) = r^2 e^{-4.27r} (1.21466 - 1.888r + 2.03r^2) \times (1 + 1.0/r - 0.03/r^2)(1 + 0.15r), \quad (6)$$

where r is the radial position of the quark in fm [49]. The azimuthal position of each quark is assigned randomly to achieve a spherically symmetric distribution. Once all of the quark coordinates are determined, the center of mass of the three-quark system is shifted to match the center position of the nucleon. The empirical function above is chosen such that after the center of mass is shifted, the radial distribution of the quark positions with respect to the nucleon center position reproduces the Fourier transform of the proton form factor as measured in electron-proton elastic scattering [50],

$$\rho^{\text{proton}}(r) = \rho_0^{\text{proton}} \times e^{-ar}, \quad (7)$$

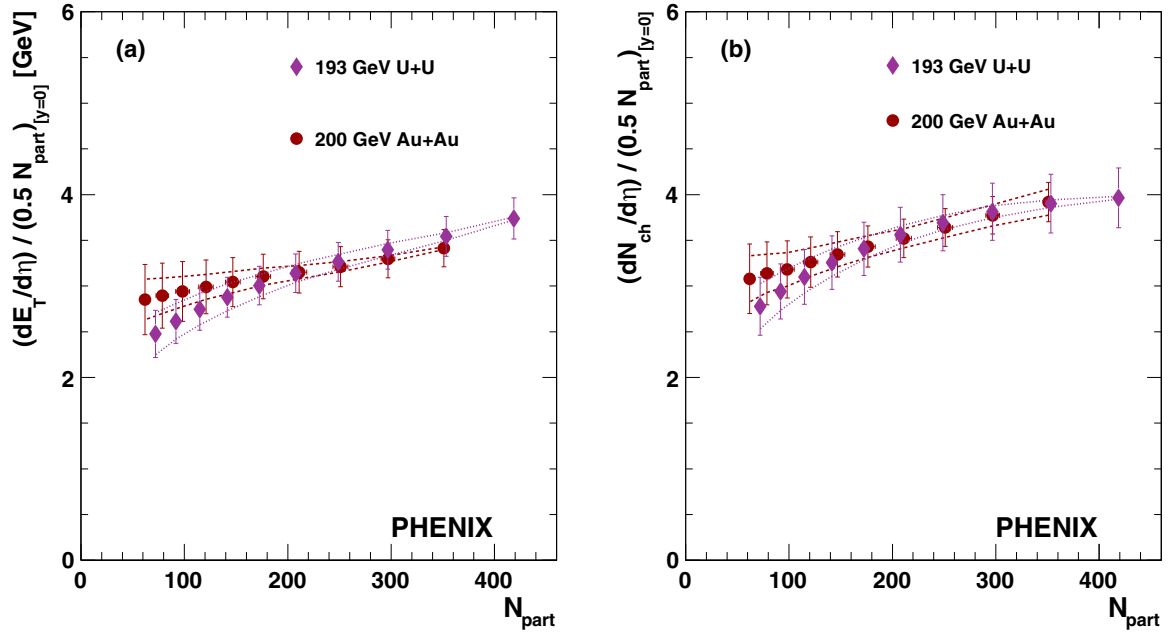


FIG. 12. $(dE_T/d\eta)/(0.5N_{\text{part}})$ (a) and $(dN_{\text{ch}}/d\eta)/(0.5N_{\text{part}})$ (b) at midrapidity as a function of N_{part} for U + U collisions. Also shown are results from Au + Au collisions at $\sqrt{s_{NN}} = 200$ GeV for comparison. The lines bounding the points represent the trigger efficiency uncertainty within which the points can be tilted. The error bars represent the remaining total statistical and systematic uncertainty.

where $a = \sqrt{12}/r_m = 4.27 \text{ fm}^{-1}$ and $r_m = 0.81 \text{ fm}$ is the rms charge radius of the proton.¹ Once all quarks in both nuclei are positioned, the coordinates of the two nuclei are shifted relative

¹This approach is necessary because if $\rho^{\text{proton}}(r)$ itself is simply sampled for the quark radial coordinates, the recentering of the three-

to each other at random uniformly in the impact parameter plane transverse to the beam axis. Interactions between a pair

quark system would result in a distortion of the radial distribution, which would then be calculated with respect to the center of mass of the generated system.

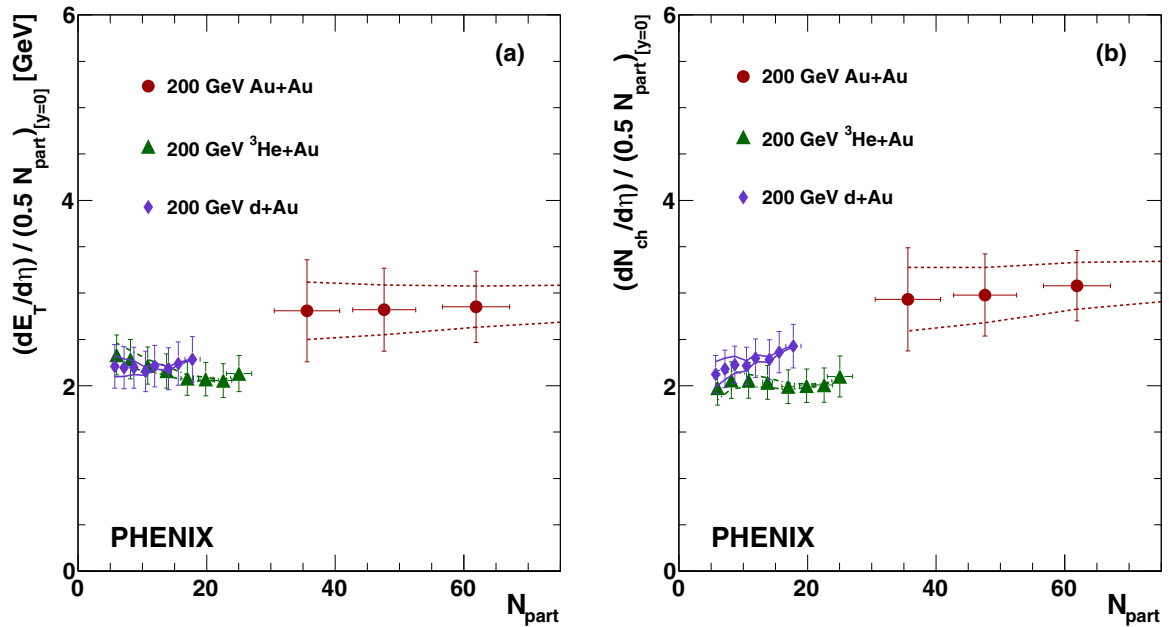


FIG. 13. $(dE_T/d\eta)/(0.5N_{\text{part}})$ (a) and $(dN_{\text{ch}}/d\eta)/(0.5N_{\text{part}})$ (b) at midrapidity as a function of N_{part} for $d + \text{Cu}$ and ${}^3\text{He} + \text{Au}$ collisions. Also shown are results from the most peripheral Au + Au collisions at $\sqrt{s_{NN}} = 200$ GeV for comparison. The lines bounding the points represent the trigger efficiency uncertainty within which the points can be tilted. The error bars represent the remaining total statistical and systematic uncertainty.

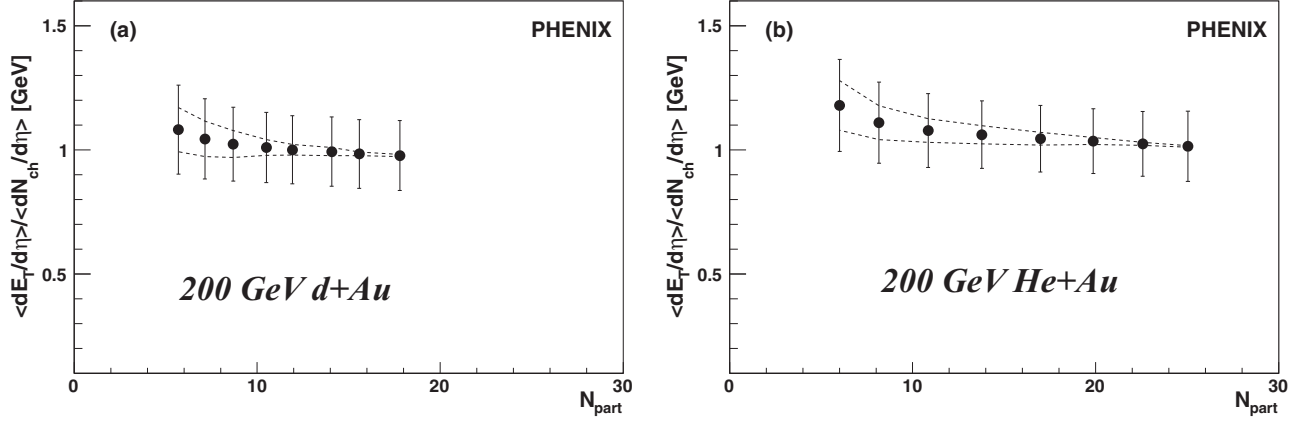


FIG. 14. The E_T/N_{ch} ratio as a function of N_{part} for 200-GeV $d + Au$ (a) and 200-GeV ${}^3\text{He} + Au$ (b) collisions. The error bars represent the total statistical and systematic uncertainties.

of quarks, one from each nucleus, occur if the distance d in this plane satisfies the condition

$$d < \sqrt{\frac{\sigma_{qq}^{inel}}{\pi}}, \quad (8)$$

where σ_{qq}^{inel} is the inelastic quark-quark cross section. The value of σ_{qq}^{inel} is set to reproduce the known inelastic nucleon-nucleon cross section when running the model for nucleon-nucleon collisions at a given collision energy. The inelastic cross sections as a function of $\sqrt{s_{NN}}$ are taken from parametrizations of cross section measurements [51]. A summary of σ_{qq}^{inel} as a function of $\sqrt{s_{NN}}$ is given in Table IV.

The values of midrapidity $dE_T/d\eta$ and $dN_{ch}/d\eta$ as a function of N_{qp} are shown in Fig. 15 for Au + Au collisions. For all collision energies, the dependence on N_{qp} is linear. When

$(dE_T/d\eta)/(0.5N_{qp})$ and $(dN_{ch}/d\eta)/(0.5N_{qp})$ are plotted as a function of N_{qp} as shown in Fig. 16, the distributions are constant within the uncertainties of the measurement, which is not the case when centrality is expressed in terms of N_{part} , shown in Fig. 2. For Au + Au collisions from $\sqrt{s_{NN}} = 200$ to 7.7 GeV, scaling with N_{qp} better describes the data than scaling with N_{part} .

Because there is a linear dependence of $dE_T/d\eta$ and $dN_{ch}/d\eta$ with N_{qp} , the data for each collision energy in Fig. 15 can be fit to a straight line $dE_T/d\eta = a_E N_{qp} + b_E$ and $dN_{ch}/d\eta = a_N N_{qp} + b_N$. The extracted slopes, a_E and a_N , represent the $dE_T/d\eta$ and $dN_{ch}/d\eta$ per quark participant, respectively. For all collision energies, the intercept of the fit at $\sqrt{s_{NN}} = 0$, which is kept as a free parameter in the fit, is consistent with zero within at most 1.3 standard deviations for all data sets. Figure 17 shows the excitation function of

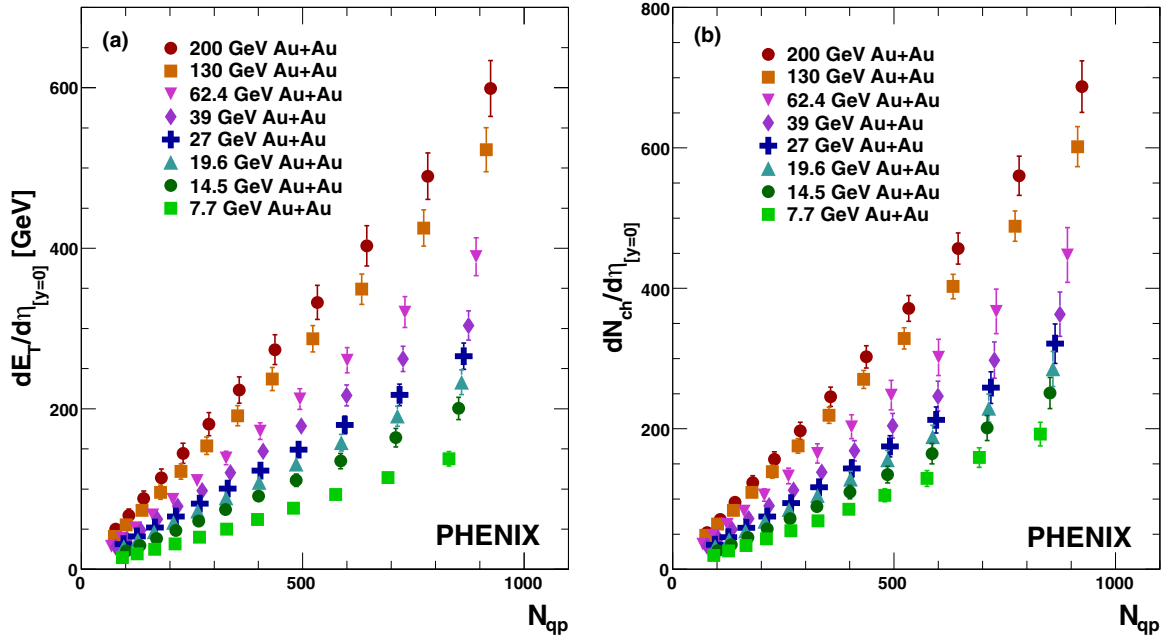


FIG. 15. $dE_T/d\eta$ (a) and $dN_{ch}/d\eta$ (b) at midrapidity as a function of N_{qp} for Au + Au collisions at $\sqrt{s_{NN}} = 200, 130, 62.4, 39, 27, 19.6, 14.5,$ and 7.7 GeV. The error bars represent the total statistical and systematic uncertainties.

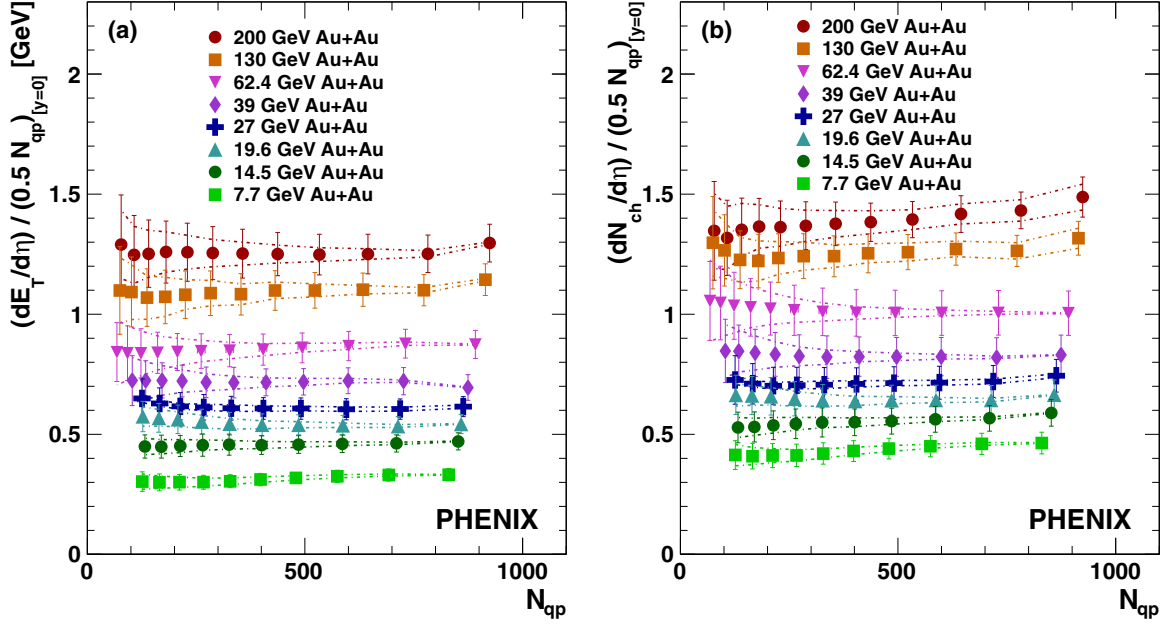


FIG. 16. $(dE_T/d\eta)/(0.5N_{qp})$ (a) and $(dN_{ch}/d\eta)/(0.5N_{qp})$ (b) at midrapidity as a function of N_{qp} for Au + Au collisions at $\sqrt{s_{NN}} = 200, 130, 62.4, 39, 27, 19.6, 14.5,$ and 7.7 GeV. The lines bounding the points represent the trigger efficiency uncertainty within which the points can be tilted. The error bars represent the remaining total statistical and systematic uncertainty.

the slopes for Au + Au collisions. The $dE_T/d\eta$ data can be described by a second-order polynomial: $a_E = 0.0408 + 0.0273 \times \log(\sqrt{s_{NN}}) + 0.0160 \times [\log(\sqrt{s_{NN}})]^2$. The $dN_{ch}/d\eta$ data can be described by a second-order polynomial: $a_N = 0.153 - 0.0096 \times \log(\sqrt{s_{NN}}) + 0.0221 \times [\log(\sqrt{s_{NN}})]^2$. The results of the linear fits for each collision energy are tabulated in Table VI.²

²Note that the method of generating constituent quarks in the present work is slightly different than that of Ref. [8], which did not preserve the center of mass of the three quarks. There is a small effect of the different methods indicated by the small difference of $\langle dE_T/d\eta \rangle / N_{qp} = 0.617 \pm 0.23$ GeV in Ref. [8] compared to the present $\langle dE_T/d\eta \rangle / N_{qp} = 0.629 \pm 0.021$ GeV.

The preference of the scaling with N_{qp} is also apparent in Cu + Cu and Cu + Au collisions. This is demonstrated in Fig. 18, which shows that $dE_T/d\eta$ and $dN_{ch}/d\eta$ increases linearly with increasing N_{qp} . As previously shown in Fig. 9, $(dE_T/d\eta)/(0.5N_{part})$ and $(dN_{ch}/d\eta)/(0.5N_{part})$ both exhibit a distinct increase as N_{part} increases for all three systems. This is not the case when comparing to Fig. 19, which shows that $(dE_T/d\eta)/(0.5N_{qp})$ and $(dN_{ch}/d\eta)/(0.5N_{qp})$ exhibit no significant dependence on N_{qp} for all three systems. Scaling with N_{qp} for $d + Au$ and ${}^3\text{He} + Au$ collisions at $\sqrt{s_{NN}} = 200$ GeV is shown in Fig. 20, along with a comparison to the most peripheral Au + Au collisions at $\sqrt{s_{NN}} = 200$ GeV. As seen when scaled with N_{part} in Fig. 13, $(dE_T/d\eta)/(0.5N_{qp})$ and $(dN_{ch}/d\eta)/(0.5N_{qp})$ are also consistent with N_{qp} scaling, with

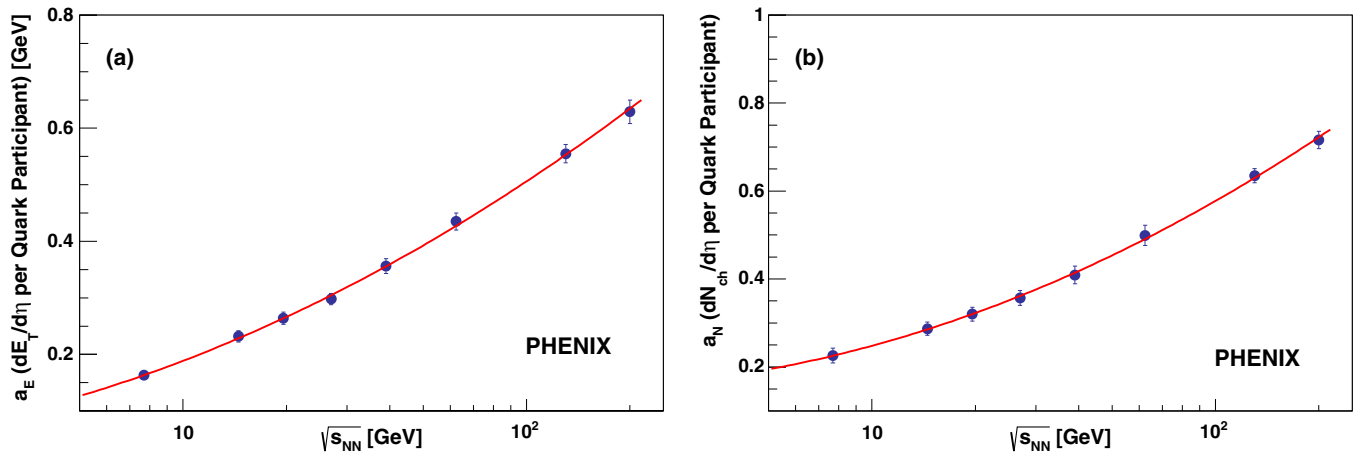


FIG. 17. The slopes of the fit to $dE_T/d\eta$, a_E (a), and $dN_{ch}/d\eta$, a_N (b), as a function of N_{qp} plotted as a function of $\sqrt{s_{NN}}$ for Au + Au collisions. The error bars are the uncertainties from the fit. The red line is a second-order polynomial fit to the data.

TABLE VI. Summary of the results of the linear fits to the functions $dE_T/d\eta = a_E N_{qp} + b_E$ and $dN_{ch}/d\eta = a_N N_{qp} + b_N$.

$\sqrt{s_{NN}}$	System	a_E (GeV)	b_E (GeV)	a_N	b_N
200 GeV	Au + Au	0.629 ± 0.021	-6.1 ± 5.4	0.716 ± 0.020	-6.0 ± 6.2
200 GeV	Cu + Au	0.612 ± 0.021	3.4 ± 2.7	0.706 ± 0.029	2.1 ± 3.7
200 GeV	Cu + Cu	0.632 ± 0.039	1.9 ± 3.9	0.735 ± 0.040	-1.1 ± 3.9
130 GeV	Au + Au	0.555 ± 0.017	-1.9 ± 4.3	0.635 ± 0.016	-1.6 ± 4.2
62.4 GeV	Au + Au	0.435 ± 0.015	-1.9 ± 3.7	0.499 ± 0.023	2.2 ± 5.2
62.4 GeV	Cu + Cu	0.449 ± 0.026	2.7 ± 2.8	0.578 ± 0.043	-0.9 ± 4.5
39 GeV	Au + Au	0.356 ± 0.013	0.8 ± 3.6	0.409 ± 0.020	1.5 ± 4.8
27 GeV	Au + Au	0.298 ± 0.010	2.9 ± 2.2	0.357 ± 0.017	0.3 ± 3.4
19.6 GeV	Au + Au	0.264 ± 0.011	3.0 ± 2.8	0.320 ± 0.016	1.5 ± 3.9
14.5 GeV	Au + Au	0.232 ± 0.010	-1.2 ± 2.5	0.287 ± 0.015	-3.2 ± 3.5
7.7 GeV	Au + Au	0.163 ± 0.007	-1.8 ± 1.8	0.226 ± 0.017	-2.9 ± 2.9

the exception of $(dN_{ch}/d\eta)/(0.5N_{qp})$ for $d + Au$ collisions. There is no significant evidence that either N_{part} or N_{qp} scaling is preferred in $d + Au$ and ${}^3\text{He} + Au$ collisions.

IX. SUMMARY

Midrapidity distributions of transverse energy, $dE_T/d\eta$, and charged-particle multiplicity, $dN_{ch}/d\eta$, have been measured for a variety of collision systems and energies, including Au + Au collisions from $\sqrt{s_{NN}} = 7.7$ to 200 GeV. The centrality-dependent distributions are presented in terms of the number of nucleon participants, N_{part} , and the number of constituent quark participants, N_{qp} . The data are better described by scaling with N_{qp} than scaling with N_{part} . This holds for Au + Au collisions from $\sqrt{s_{NN}} = 200$ GeV down to $\sqrt{s_{NN}} = 7.7$ GeV, for Cu + Au collisions at $\sqrt{s_{NN}} = 200$ GeV,

and for Cu + Cu collisions at $\sqrt{s_{NN}} = 62.4$ and 200 GeV. Although comparisons of the data to models such as HIJING, parton saturation models like EKRT and KLN, and multiphase transport models such as AMPT are met with some success, a simple description using N_{qp} scaling describes the data very well.

Some of the outstanding features of the data include the following. It is observed that measurements of $(dE_T/d\eta)/(0.5N_{part})$ and $(dN_{ch}/d\eta)/(0.5N_{part})$ from a variety of systems including Au + Au, Cu + Au, and Cu + Cu at $\sqrt{s_{NN}} = 200$ GeV are all consistent with each other as a function of N_{part} . The production of E_T and N_{ch} in collisions of symmetric nuclei depends only on the collision energy and is independent of the size of the colliding system. The centrality-dependent distributions of the Bjorken energy density ε_{BJ} show an increasing trend with both N_{part} and $\sqrt{s_{NN}}$.

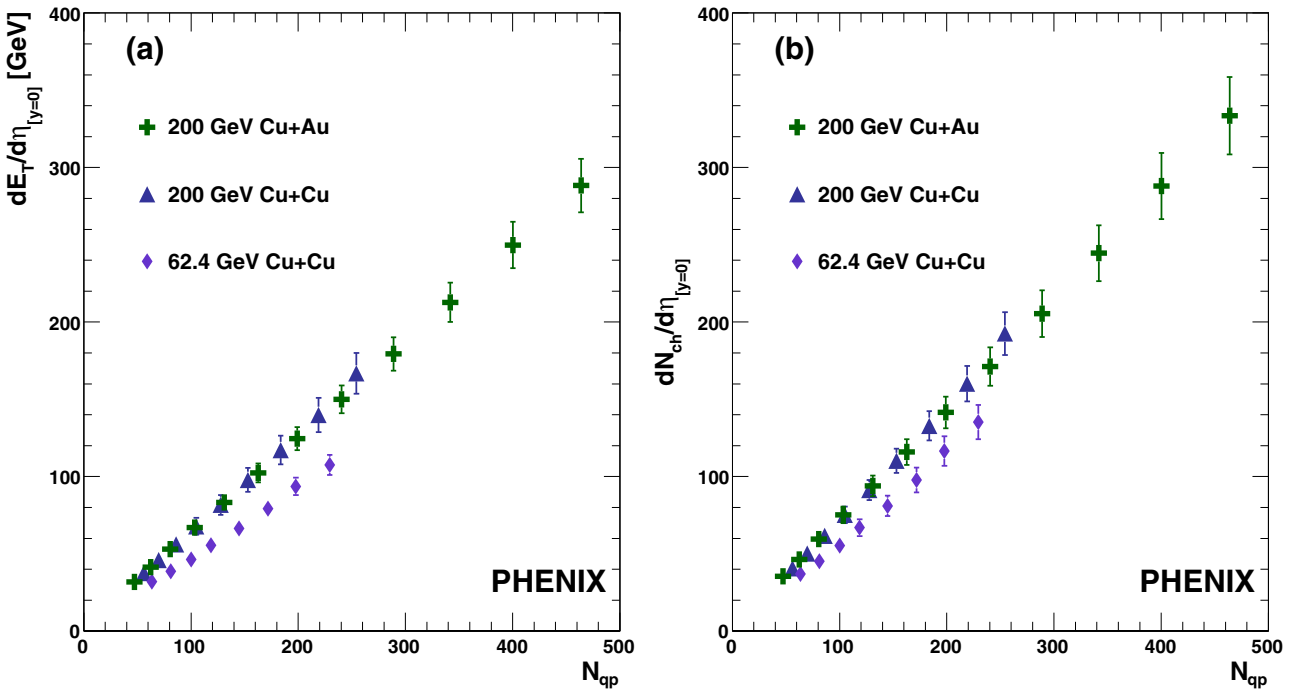


FIG. 18. $dE_T/d\eta$ (a) and $dN_{ch}/d\eta$ (b) at midrapidity as a function of N_{qp} for Cu + Cu and Cu + Au collisions. The error bars represent the total statistical and systematic uncertainties.

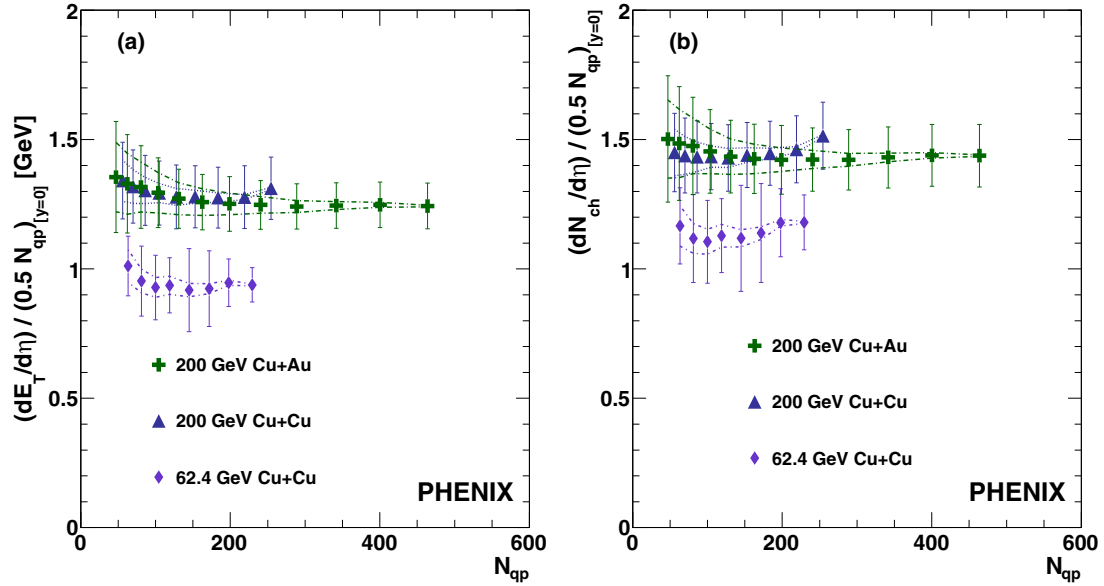


FIG. 19. $(dE_T/d\eta)/(0.5N_{qp})$ (a) and $(dN_{ch}/d\eta)/(0.5N_{qp})$ (b) at midrapidity as a function of N_{qp} for Cu + Cu and Cu + Au collisions. The lines bounding the points represent the trigger efficiency uncertainty within which the points can be tilted. The error bars represent the remaining total statistical and systematic uncertainty.

At $\sqrt{s_{NN}} = 200$ GeV, ε_{BJ} for Cu + Au and Cu + Cu collisions are consistent with each other for all N_{part} , again demonstrating that E_T production is independent of the system size. The ratio of $dE_T/d\eta$ to $dN_{ch}/d\eta$ is found to be constant as a function of centrality for all collision systems and energies. There is also only a weak dependence of this ratio as function of $\sqrt{s_{NN}}$ from $\sqrt{s_{NN}} = 7.7$ to 200 GeV. Taking the ratio of $(dE_T/d\eta)/(0.5N_{part})$ and $(dN_{ch}/d\eta)/(0.5N_{part})$ for $\sqrt{s_{NN}} = 200$ GeV to 7.7 GeV shows that the shape of the distributions

as a function of N_{part} does not change significantly over this collision energy range. For central Au + Au collisions from $\sqrt{s_{NN}} = 200$ to 7.7 GeV, the value of $(dE_T/d\eta)/(0.5N_{part})$ and $(dN_{ch}/d\eta)/(0.5N_{part})$ exhibits a power-law behavior as a function of $\sqrt{s_{NN}}$. Extending this observation, the Bjorken energy density also exhibits a power-law behavior in central Au + Au collisions from $\sqrt{s_{NN}} = 200$ to 7.7 GeV. Also, calculations of $dE_T/d\eta$ and $dN_{ch}/d\eta$ per quark participant are observed to increase as $\sqrt{s_{NN}}$ increases.

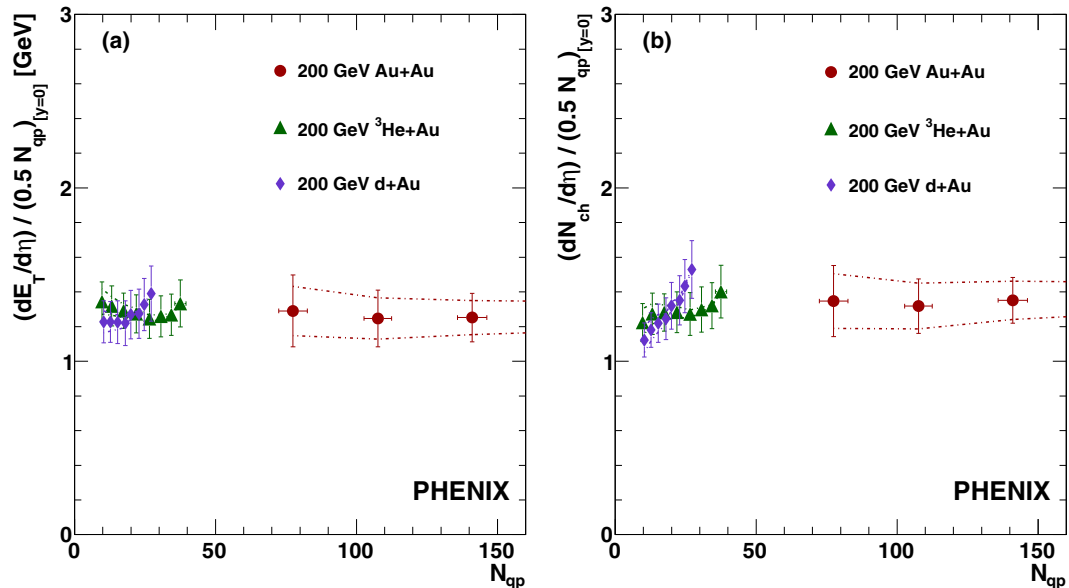


FIG. 20. $(dE_T/d\eta)/(0.5N_{qp})$ (a) and $(dN_{ch}/d\eta)/(0.5N_{qp})$ (b) at midrapidity as a function of N_{qp} for $d + Au$ and ${}^3\text{He} + Au$ collisions. Shown for comparison are data from the most peripheral Au + Au collisions at $\sqrt{s_{NN}} = 200$ GeV. The lines bounding the points represent the trigger efficiency uncertainty within which the points can be tilted. The error bars represent the remaining total statistical and systematic uncertainty.

TABLE VII. Transverse-energy results for 200-GeV Au + Au collisions. The uncertainties include the total statistical and systematic uncertainties.

Centrality	$\langle N_{\text{part}} \rangle$	$\langle N_{\text{qp}} \rangle$	$dE_T/d\eta$ (GeV)	$(dE_T/d\eta)/(0.5N_{\text{part}})$ (GeV)	$(dE_T/d\eta)/(0.5N_{\text{qp}})$ (GeV)
0%–5%	350.9 ± 4.7	924.1 ± 16.2	599.0 ± 34.7	3.41 ± 0.20	1.30 ± 0.08
5%–10%	297.0 ± 6.6	782.6 ± 15.3	498.7 ± 28.9	3.30 ± 0.21	1.25 ± 0.08
10%–15%	251.0 ± 7.3	644.6 ± 14.5	403.0 ± 25.0	3.21 ± 0.22	1.25 ± 0.08
15%–20%	211.0 ± 7.3	532.9 ± 12.3	332.5 ± 21.2	3.15 ± 0.23	1.25 ± 0.08
20%–25%	176.3 ± 7.0	437.5 ± 10.4	273.6 ± 18.6	3.10 ± 0.24	1.25 ± 0.09
25%–30%	146.8 ± 7.1	356.8 ± 12.2	223.4 ± 16.4	3.04 ± 0.27	1.25 ± 0.10
30%–35%	120.9 ± 7.0	288.3 ± 11.0	180.8 ± 14.3	2.99 ± 0.29	1.25 ± 0.11
35%–40%	98.3 ± 6.8	229.7 ± 9.2	144.5 ± 12.6	2.94 ± 0.33	1.26 ± 0.12
40%–45%	78.7 ± 6.1	181.0 ± 6.8	113.9 ± 10.9	2.89 ± 0.36	1.26 ± 0.13
45%–50%	61.9 ± 5.2	141.1 ± 5.3	88.3 ± 9.3	2.85 ± 0.38	1.25 ± 0.14
50%–55%	47.6 ± 4.9	107.6 ± 5.5	67.1 ± 8.1	2.82 ± 0.45	1.25 ± 0.16
55%–60%	35.6 ± 5.1	77.5 ± 6.8	50.0 ± 6.7	2.81 ± 0.55	1.29 ± 0.21

ACKNOWLEDGMENTS

We thank the staff of the Collider-Accelerator and Physics Departments at Brookhaven National Laboratory and the staff of the other PHENIX participating institutions for their vital contributions. We also thank Adam Bzdak for useful discussions. We acknowledge support from the Office of Nuclear Physics in the Office of Science of the Department of Energy, the National Science Foundation, Abilene Christian University Research Council, Research Foundation of SUNY, and Dean of the College of Arts and Sciences, Vanderbilt University (USA); Ministry of Education, Culture, Sports, Science, and Technology and the Japan Society for the Promotion of Science (Japan); Conselho Nacional de Desenvolvimento Científico e Tecnológico and Fundação de Amparo à Pesquisa do Estado de São Paulo (Brazil); Natural Science Foundation of China (People’s Republic of China); Croatian Science Foundation and Ministry of Science, Education, and Sports (Croatia); Ministry of Education, Youth and Sports (Czech Republic); Centre National de la Recherche Scientifique, Commissariat à l’Énergie Atomique, and Institut National de Physique Nucléaire et de Physique des Particules (France); Bundesmin-

isterium für Bildung und Forschung, Deutscher Akademischer Austausch Dienst, and Alexander von Humboldt Stiftung (Germany); National Science Fund, OTKA, Károly Róbert University College, and the Ch. Simonyi Fund (Hungary); Department of Atomic Energy and Department of Science and Technology (India); Israel Science Foundation (Israel); Basic Science Research Program through NRF of the Ministry of Education (Korea); Physics Department, Lahore University of Management Sciences (Pakistan); Ministry of Education and Science, Russian Academy of Sciences, Federal Agency of Atomic Energy (Russia); VR and Wallenberg Foundation (Sweden); the U.S. Civilian Research and Development Foundation for the Independent States of the Former Soviet Union, the Hungarian American Enterprise Scholarship Fund, and the US-Israel Binational Science Foundation.

APPENDIX

This appendix contains data tables for the $dE_T/d\eta$ and $dN_{\text{ch}}/d\eta$ measurements for each of the collision systems (see Tables VII–XXXIV).

TABLE VIII. Charged-particle multiplicity results for 200-GeV Au + Au collisions. The uncertainties include the total statistical and systematic uncertainties.

Centrality	$\langle N_{\text{part}} \rangle$	$\langle N_{\text{qp}} \rangle$	$dN_{\text{ch}}/d\eta$	$(dN_{\text{ch}}/d\eta)/(0.5N_{\text{part}})$	$(dN_{\text{ch}}/d\eta)/(0.5N_{\text{qp}})$
0%–5%	350.9 ± 4.7	924.1 ± 16.2	687.4 ± 36.6	3.92 ± 0.22	1.49 ± 0.08
5%–10%	297.9 ± 6.6	782.6 ± 15.3	560.4 ± 27.9	3.77 ± 0.21	1.43 ± 0.08
10%–15%	251.0 ± 7.3	644.6 ± 14.5	456.8 ± 22.3	3.64 ± 0.21	1.42 ± 0.08
15%–20%	211.0 ± 7.3	532.9 ± 12.3	371.5 ± 18.2	3.52 ± 0.21	1.39 ± 0.08
20%–25%	176.3 ± 7.0	437.5 ± 10.4	302.5 ± 15.8	3.43 ± 0.22	1.38 ± 0.08
25%–30%	146.8 ± 7.1	356.8 ± 12.2	245.6 ± 13.8	3.35 ± 0.25	1.38 ± 0.09
30%–35%	120.9 ± 7.0	288.3 ± 11.0	197.2 ± 12.2	3.26 ± 0.28	1.37 ± 0.10
35%–40%	98.3 ± 6.8	229.7 ± 9.2	156.4 ± 10.9	3.18 ± 0.31	1.36 ± 0.11
40%–45%	78.7 ± 6.1	181.0 ± 6.8	123.5 ± 9.6	3.14 ± 0.34	1.36 ± 0.12
45%–50%	61.9 ± 5.2	141.1 ± 5.3	95.3 ± 8.6	3.08 ± 0.38	1.35 ± 0.13
50%–55%	47.6 ± 4.9	107.6 ± 5.5	70.9 ± 7.6	2.98 ± 0.44	1.32 ± 0.16
55%–60%	35.6 ± 5.1	77.5 ± 6.8	52.2 ± 6.5	2.93 ± 0.56	1.35 ± 0.20

TABLE IX. Transverse-energy results for 130-GeV Au + Au collisions. The uncertainties include the total statistical and systematic uncertainties.

Centrality	$\langle N_{\text{part}} \rangle$	$\langle N_{\text{qp}} \rangle$	$dE_T/d\eta$ (GeV)	$(dE_T/d\eta)/(0.5N_{\text{part}})$ (GeV)	$(dE_T/d\eta)/(0.5N_{\text{qp}})$ (GeV)
0%–5%	347.7 ± 10.0	914.1 ± 22.6	522.8 ± 27.3	3.01 ± 0.18	1.14 ± 0.07
5%–10%	294.0 ± 8.9	773.3 ± 20.3	425.2 ± 22.5	2.89 ± 0.18	1.10 ± 0.07
10%–15%	249.5 ± 8.0	633.4 ± 19.4	349.0 ± 19.0	2.80 ± 0.18	1.10 ± 0.07
15%–20%	211.0 ± 7.2	522.6 ± 18.3	287.2 ± 16.5	2.72 ± 0.18	1.10 ± 0.07
20%–25%	178.6 ± 6.6	431.5 ± 19.0	237.1 ± 14.5	2.66 ± 0.19	1.10 ± 0.08
25%–30%	149.7 ± 6.0	353.3 ± 15.9	191.3 ± 12.5	2.56 ± 0.20	1.08 ± 0.09
30%–35%	124.8 ± 5.5	283.0 ± 13.2	153.9 ± 11.0	2.47 ± 0.21	1.09 ± 0.09
35%–40%	102.9 ± 5.1	225.3 ± 11.0	121.8 ± 9.4	2.37 ± 0.22	1.08 ± 0.10
40%–45%	83.2 ± 4.7	179.1 ± 8.8	96.0 ± 8.8	2.31 ± 0.25	1.07 ± 0.11
45%–50%	66.3 ± 4.3	137.1 ± 7.1	73.3 ± 7.3	2.21 ± 0.26	1.07 ± 0.12
50%–55%	52.1 ± 4.0	101.6 ± 6.5	55.5 ± 6.5	2.13 ± 0.30	1.09 ± 0.15
55%–60%	40.1 ± 3.8	74.6 ± 7.3	41.0 ± 5.5	2.04 ± 0.34	1.10 ± 0.18

TABLE X. Charged-particle multiplicity results for 130-GeV Au + Au collisions. The uncertainties include the total statistical and systematic uncertainties.

Centrality	$\langle N_{\text{part}} \rangle$	$\langle N_{\text{qp}} \rangle$	$dN_{\text{ch}}/d\eta$	$(dN_{\text{ch}}/d\eta)/(0.5N_{\text{part}})$	$(dN_{\text{ch}}/d\eta)/(0.5N_{\text{qp}})$
0%–5%	347.7 ± 10.0	914.1 ± 22.6	601.8 ± 28.4	3.46 ± 0.19	1.32 ± 0.07
5%–10%	294.0 ± 8.9	773.3 ± 20.3	488.5 ± 21.6	3.32 ± 0.18	1.26 ± 0.07
10%–15%	249.5 ± 8.0	633.4 ± 19.4	402.7 ± 17.4	3.23 ± 0.17	1.27 ± 0.07
15%–20%	211.0 ± 7.2	522.6 ± 18.3	328.8 ± 15.2	3.12 ± 0.18	1.26 ± 0.07
20%–25%	178.6 ± 6.6	431.5 ± 19.0	270.5 ± 12.8	3.03 ± 0.18	1.25 ± 0.08
25%–30%	149.7 ± 6.0	353.3 ± 15.9	219.3 ± 11.4	2.93 ± 0.19	1.24 ± 0.09
30%–35%	124.8 ± 5.5	283.0 ± 13.2	175.7 ± 10.3	2.82 ± 0.21	1.24 ± 0.09
35%–40%	102.9 ± 5.1	225.3 ± 11.0	139.0 ± 9.1	2.70 ± 0.22	1.23 ± 0.10
40%–45%	83.2 ± 4.7	179.1 ± 8.8	109.4 ± 8.4	2.63 ± 0.25	1.22 ± 0.11
45%–50%	66.3 ± 4.3	137.1 ± 7.1	84.1 ± 7.0	2.54 ± 0.27	1.23 ± 0.12
50%–55%	52.1 ± 4	101.6 ± 6.5	64.3 ± 6.3	2.47 ± 0.31	1.27 ± 0.15
55%–60%	40.1 ± 3.8	74.6 ± 7.3	48.4 ± 5.4	2.41 ± 0.35	1.30 ± 0.19

TABLE XI. Transverse-energy results for 62.4-GeV Au + Au collisions. The uncertainties include the total statistical and systematic uncertainties.

Centrality	$\langle N_{\text{part}} \rangle$	$\langle N_{\text{qp}} \rangle$	$dE_T/d\eta$ (GeV)	$(dE_T/d\eta)/(0.5N_{\text{part}})$ (GeV)	$(dE_T/d\eta)/(0.5N_{\text{qp}})$ (GeV)
0%–5%	342.6 ± 4.9	891.7 ± 26.6	389.7 ± 23.5	2.27 ± 0.14	0.87 ± 0.06
5%–10%	291.3 ± 7.3	730.7 ± 24.1	320.5 ± 19.3	2.20 ± 0.14	0.88 ± 0.06
10%–15%	244.5 ± 8.9	600.6 ± 21.5	260.6 ± 15.7	2.13 ± 0.15	0.87 ± 0.06
15%–20%	205.0 ± 9.6	493.4 ± 19.6	212.1 ± 12.8	2.07 ± 0.16	0.86 ± 0.06
20%–25%	171.3 ± 8.9	403.8 ± 18.5	171.9 ± 10.4	2.01 ± 0.16	0.85 ± 0.06
25%–30%	142.2 ± 8.5	327.0 ± 16.7	138.6 ± 8.36	1.95 ± 0.17	0.85 ± 0.07
30%–35%	116.7 ± 8.9	261.7 ± 15.7	110.4 ± 6.67	1.90 ± 0.18	0.85 ± 0.07
35%–40%	95.2 ± 7.7	206.9 ± 14.3	86.9 ± 5.25	1.83 ± 0.19	0.84 ± 0.08
40%–45%	76.1 ± 7.7	161.4 ± 13.3	67.3 ± 4.08	1.78 ± 0.21	0.84 ± 0.09
45%–50%	59.9 ± 6.9	123.5 ± 13.2	51.2 ± 3.12	1.73 ± 0.22	0.84 ± 0.10
50%–55%	46.8 ± 5.2	92.4 ± 11.2	38.4 ± 2.33	1.65 ± 0.21	0.84 ± 0.11
55%–60%	35.8 ± 4.6	67.8 ± 9.0	28.5 ± 1.72	1.59 ± 0.23	0.84 ± 0.12

TABLE XII. Charged-particle multiplicity results for 62.4-GeV Au + Au collisions. The uncertainties include the total statistical and systematic uncertainties.

Centrality	$\langle N_{\text{part}} \rangle$	$\langle N_{\text{qp}} \rangle$	$dN_{\text{ch}}/d\eta$	$(dN_{\text{ch}}/d\eta)/(0.5N_{\text{part}})$	$(dN_{\text{ch}}/d\eta)/(0.5N_{\text{qp}})$
0%–5%	342.6 ± 4.9	891.7 ± 26.6	447.5 ± 38.9	2.61 ± 0.23	1.00 ± 0.09
5%–10%	291.3 ± 7.3	730.7 ± 24.1	367.4 ± 31.6	2.52 ± 0.23	1.01 ± 0.09
10%–15%	244.5 ± 8.9	600.6 ± 21.5	301.8 ± 25.8	2.47 ± 0.23	1.01 ± 0.09
15%–20%	205.0 ± 9.6	493.4 ± 19.6	248.0 ± 21.0	2.42 ± 0.23	1.01 ± 0.09
20%–25%	171.3 ± 8.9	403.8 ± 18.5	203.0 ± 17.1	2.37 ± 0.24	1.01 ± 0.10
25%–30%	142.2 ± 8.5	327.0 ± 16.7	165.1 ± 13.8	2.32 ± 0.24	1.01 ± 0.10
30%–35%	116.7 ± 8.9	261.7 ± 15.7	133.0 ± 11.1	2.28 ± 0.26	1.02 ± 0.10
35%–40%	95.2 ± 7.7	206.9 ± 14.3	105.9 ± 8.76	2.22 ± 0.26	1.02 ± 0.11
40%–45%	76.1 ± 7.7	161.4 ± 13.3	83.0 ± 6.83	2.18 ± 0.28	1.03 ± 0.12
45%–50%	59.9 ± 6.9	123.5 ± 13.2	63.9 ± 5.24	2.13 ± 0.30	1.03 ± 0.14
50%–55%	46.8 ± 5.2	92.4 ± 11.2	48.4 ± 3.95	2.07 ± 0.29	1.05 ± 0.15
55%–60%	35.8 ± 4.6	67.8 ± 9.0	35.8 ± 2.92	2.00 ± 0.30	1.06 ± 0.16

TABLE XIII. Transverse-energy results for 39-GeV Au + Au collisions. The uncertainties include the total statistical and systematic uncertainties.

Centrality	$\langle N_{\text{part}} \rangle$	$\langle N_{\text{qp}} \rangle$	$dE_T/d\eta$ (GeV)	$(dE_T/d\eta)/(0.5N_{\text{part}})$ (GeV)	$(dE_T/d\eta)/(0.5N_{\text{qp}})$ (GeV)
0%–5%	340.0 ± 7.4	874.6 ± 42.0	303.8 ± 18.2	1.79 ± 0.11	0.69 ± 0.05
5%–10%	289.6 ± 8.1	726.7 ± 36.7	262.1 ± 15.7	1.81 ± 0.12	0.72 ± 0.06
10%–15%	244.1 ± 6.4	599.1 ± 26.8	216.6 ± 13.0	1.77 ± 0.12	0.72 ± 0.05
15%–20%	206.5 ± 6.3	496.9 ± 23.7	178.5 ± 10.7	1.73 ± 0.12	0.72 ± 0.06
20%–25%	174.1 ± 6.3	410.4 ± 20.9	146.9 ± 8.8	1.69 ± 0.12	0.72 ± 0.06
25%–30%	145.8 ± 6.2	336.8 ± 22.2	120.4 ± 7.2	1.65 ± 0.12	0.72 ± 0.06
30%–35%	120.8 ± 7.5	273.0 ± 18.1	97.7 ± 5.8	1.62 ± 0.14	0.72 ± 0.06
35%–40%	98.6 ± 6.4	217.6 ± 15.1	78.5 ± 4.7	1.59 ± 0.14	0.72 ± 0.07
40%–45%	79.8 ± 6.0	172.0 ± 14.1	62.3 ± 3.7	1.56 ± 0.15	0.72 ± 0.07
45%–50%	63.9 ± 5.8	134.3 ± 13.1	48.6 ± 2.9	1.52 ± 0.17	0.72 ± 0.08
50%–55%	50.3 ± 5.5	103.1 ± 13.5	37.3 ± 2.2	1.48 ± 0.18	0.72 ± 0.10

TABLE XIV. Charged-particle multiplicity results for 39-GeV Au + Au collisions. The uncertainties include the total statistical and systematic uncertainties.

Centrality	$\langle N_{\text{part}} \rangle$	$\langle N_{\text{qp}} \rangle$	$dN_{\text{ch}}/d\eta$	$(dN_{\text{ch}}/d\eta)/(0.5N_{\text{part}})$	$(dN_{\text{ch}}/d\eta)/(0.5N_{\text{qp}})$
0%–5%	340.0 ± 7.4	874.6 ± 42.0	363.2 ± 31.6	2.14 ± 0.19	0.83 ± 0.08
5%–10%	289.6 ± 8.1	726.7 ± 36.7	297.8 ± 25.8	2.06 ± 0.19	0.82 ± 0.08
10%–15%	244.1 ± 6.4	599.1 ± 26.8	246.6 ± 21.3	2.02 ± 0.18	0.82 ± 0.08
15%–20%	206.5 ± 6.3	496.9 ± 23.7	204.4 ± 17.5	1.98 ± 0.18	0.82 ± 0.08
20%–25%	174.1 ± 6.3	410.4 ± 20.9	168.9 ± 14.4	1.94 ± 0.18	0.82 ± 0.08
25%–30%	145.8 ± 6.2	336.8 ± 22.2	138.3 ± 11.8	1.90 ± 0.18	0.82 ± 0.09
30%–35%	120.8 ± 7.5	273.0 ± 18.1	112.6 ± 9.6	1.86 ± 0.20	0.83 ± 0.09
35%–40%	98.6 ± 6.4	217.6 ± 15.1	90.6 ± 7.7	1.84 ± 0.20	0.83 ± 0.09
40%–45%	79.8 ± 6.0	172.0 ± 14.1	72.1 ± 6.1	1.81 ± 0.20	0.84 ± 0.10
45%–50%	63.9 ± 5.8	134.3 ± 13.1	56.8 ± 4.8	1.78 ± 0.22	0.85 ± 0.11
50%–55%	50.3 ± 5.5	103.1 ± 13.5	43.7 ± 3.7	1.73 ± 0.24	0.85 ± 0.13

TABLE XV. Transverse-energy results for 27-GeV Au + Au collisions. The uncertainties include the total statistical and systematic uncertainties.

Centrality	$\langle N_{\text{part}} \rangle$	$\langle N_{\text{qp}} \rangle$	$dE_T/d\eta$ (GeV)	$(dE_T/d\eta)/(0.5N_{\text{part}})$ (GeV)	$(dE_T/d\eta)/(0.5N_{\text{qp}})$ (GeV)
0%–5%	338.9 ± 3.1	863.7 ± 23.5	265.6 ± 16.4	1.57 ± 0.10	0.62 ± 0.04
5%–10%	288.8 ± 4.7	718.8 ± 22.7	217.3 ± 13.4	1.50 ± 0.10	0.61 ± 0.04
10%–15%	244.3 ± 6.5	595.0 ± 23.7	179.7 ± 11.1	1.47 ± 0.10	0.60 ± 0.04
15%–20%	205.7 ± 5.8	490.7 ± 19.4	148.9 ± 9.2	1.45 ± 0.10	0.61 ± 0.04
20%–25%	173.0 ± 5.5	404.6 ± 16.7	122.8 ± 7.6	1.42 ± 0.10	0.61 ± 0.05
25%–30%	144.6 ± 6.2	330.8 ± 17.7	100.7 ± 6.2	1.39 ± 0.10	0.61 ± 0.05
30%–35%	119.4 ± 6.1	267.4 ± 16.2	81.9 ± 5.1	1.37 ± 0.11	0.61 ± 0.05
35%–40%	97.6 ± 5.8	213.6 ± 14.6	65.8 ± 4.1	1.35 ± 0.12	0.62 ± 0.06
40%–45%	77.9 ± 5.7	166.0 ± 13.7	52.1 ± 3.2	1.34 ± 0.13	0.63 ± 0.06
45%–50%	60.8 ± 6.0	125.9 ± 13.8	40.8 ± 2.5	1.34 ± 0.16	0.65 ± 0.08

TABLE XVI. Charged-particle multiplicity results for 27 GeV Au + Au collisions. The uncertainties include the total statistical and systematic uncertainties.

Centrality	$\langle N_{\text{part}} \rangle$	$\langle N_{\text{qp}} \rangle$	$dN_{\text{ch}}/d\eta$	$(dN_{\text{ch}}/d\eta)/(0.5N_{\text{part}})$	$(dN_{\text{ch}}/d\eta)/(0.5N_{\text{qp}})$
0%–5%	338.9 ± 3.1	863.7 ± 23.5	321.2 ± 28.1	1.90 ± 0.17	0.74 ± 0.07
5%–10%	288.8 ± 4.7	718.8 ± 22.7	258.7 ± 22.5	1.79 ± 0.16	0.72 ± 0.07
10%–15%	244.3 ± 6.5	595.0 ± 23.7	212.6 ± 18.5	1.74 ± 0.16	0.72 ± 0.07
15%–20%	205.7 ± 5.8	490.7 ± 19.4	175.0 ± 15.1	1.70 ± 0.16	0.71 ± 0.07
20%–25%	173.0 ± 5.5	404.6 ± 16.7	143.5 ± 12.4	1.66 ± 0.15	0.71 ± 0.07
25%–30%	144.6 ± 6.2	330.8 ± 17.7	116.7 ± 10.0	1.61 ± 0.16	0.71 ± 0.07
30%–35%	119.4 ± 6.1	267.4 ± 16.2	94.2 ± 8.1	1.58 ± 0.16	0.70 ± 0.07
35%–40%	97.6 ± 5.8	213.6 ± 14.6	75.0 ± 6.4	1.54 ± 0.16	0.70 ± 0.08
40%–45%	77.9 ± 5.7	166.0 ± 13.7	59.0 ± 5.0	1.51 ± 0.17	0.71 ± 0.08
45%–50%	60.8 ± 6.0	125.9 ± 13.8	45.7 ± 3.9	1.50 ± 0.20	0.73 ± 0.10

TABLE XVII. Transverse-energy results for 19.6-GeV Au + Au collisions. The uncertainties include the total statistical and systematic uncertainties.

Centrality	$\langle N_{\text{part}} \rangle$	$\langle N_{\text{qp}} \rangle$	$dE_T/d\eta$ (GeV)	$(dE_T/d\eta)/(0.5N_{\text{part}})$ (GeV)	$(dE_T/d\eta)/(0.5N_{\text{qp}})$ (GeV)
0%–5%	338.5 ± 4.4	858.8 ± 27.7	233.1 ± 15.3	1.38 ± 0.09	0.54 ± 0.04
5%–10%	288.3 ± 6.0	714.1 ± 25.0	190.7 ± 12.5	1.32 ± 0.09	0.53 ± 0.04
10%–15%	242.4 ± 6.1	587.3 ± 23.2	157.8 ± 10.3	1.30 ± 0.09	0.54 ± 0.04
15%–20%	204.3 ± 5.7	485.0 ± 20.0	130.8 ± 8.6	1.28 ± 0.09	0.54 ± 0.04
20%–25%	172.4 ± 7.3	401.4 ± 22.0	108.2 ± 7.1	1.25 ± 0.10	0.54 ± 0.05
25%–30%	143.5 ± 6.6	326.9 ± 18.4	88.9 ± 5.8	1.24 ± 0.10	0.54 ± 0.05
30%–35%	117.9 ± 6.7	262.5 ± 17.7	72.5 ± 4.8	1.23 ± 0.11	0.55 ± 0.05
35%–40%	95.7 ± 6.9	208.0 ± 17.0	58.5 ± 3.8	1.22 ± 0.12	0.56 ± 0.06
40%–45%	77.4 ± 5.7	164.2 ± 13.5	46.6 ± 3.1	1.21 ± 0.12	0.57 ± 0.06
45%–50%	61.7 ± 4.8	127.7 ± 11.3	36.6 ± 2.4	1.19 ± 0.12	0.57 ± 0.06

TABLE XVIII. Charged-particle multiplicity results for 19.6-GeV Au + Au collisions. The uncertainties include the total statistical and systematic uncertainties.

Centrality	$\langle N_{\text{part}} \rangle$	$\langle N_{\text{qp}} \rangle$	$dN_{\text{ch}}/d\eta$	$(dN_{\text{ch}}/d\eta)/(0.5N_{\text{part}})$	$(dN_{\text{ch}}/d\eta)/(0.5N_{\text{qp}})$
0%–5%	338.5 ± 4.4	858.8 ± 27.7	285.3 ± 25.1	1.69 ± 0.15	0.66 ± 0.06
5%–10%	288.3 ± 6.0	714.1 ± 25.0	229.3 ± 20.1	1.59 ± 0.14	0.64 ± 0.06
10%–15%	242.4 ± 6.1	587.3 ± 23.2	188.8 ± 16.5	1.56 ± 0.14	0.64 ± 0.06
15%–20%	204.3 ± 5.7	485.0 ± 20.0	155.7 ± 13.5	1.52 ± 0.14	0.64 ± 0.06
20%–25%	172.4 ± 7.3	401.4 ± 22.0	128.2 ± 11.1	1.49 ± 0.14	0.64 ± 0.07
25%–30%	143.5 ± 6.6	326.9 ± 18.4	104.8 ± 9.1	1.46 ± 0.14	0.64 ± 0.07
30%–35%	117.9 ± 6.7	262.5 ± 17.7	85.1 ± 7.4	1.44 ± 0.15	0.65 ± 0.07
35%–40%	95.7 ± 6.9	208.0 ± 17.0	68.4 ± 5.9	1.43 ± 0.16	0.66 ± 0.08
40%–45%	77.4 ± 5.7	164.2 ± 13.5	54.3 ± 4.7	1.40 ± 0.16	0.66 ± 0.08
45%–50%	61.7 ± 4.8	127.7 ± 11.3	42.4 ± 3.7	1.37 ± 0.16	0.66 ± 0.08

TABLE XIX. Transverse-energy results for 14.5-GeV Au + Au collisions. The uncertainties include the total statistical and systematic uncertainties.

Centrality	$\langle N_{\text{part}} \rangle$	$\langle N_{\text{qp}} \rangle$	$dE_T/d\eta$ (GeV)	$(dE_T/d\eta)/(0.5N_{\text{part}})$ (GeV)	$(dE_T/d\eta)/(0.5N_{\text{qp}})$ (GeV)
0%–5%	337.3 ± 4.2	852.0 ± 27.5	200.4 ± 14.0	1.19 ± 0.08	0.47 ± 0.04
5%–10%	287.7 ± 4.9	710.1 ± 23.4	164.0 ± 11.5	1.14 ± 0.08	0.46 ± 0.04
10%–15%	242.5 ± 5.5	585.6 ± 22.0	134.9 ± 9.4	1.11 ± 0.08	0.46 ± 0.04
15%–20%	205.1 ± 5.9	485.5 ± 19.7	111.0 ± 7.8	1.08 ± 0.08	0.46 ± 0.04
20%–25%	172.6 ± 6.4	400.4 ± 19.6	91.1 ± 6.4	1.06 ± 0.08	0.46 ± 0.04
25%–30%	143.6 ± 7.8	325.9 ± 21.7	74.4 ± 5.2	1.04 ± 0.09	0.46 ± 0.04
30%–35%	119.2 ± 7.2	264.9 ± 19.2	60.2 ± 4.2	1.01 ± 0.09	0.45 ± 0.05
35%–40%	98.3 ± 5.8	213.7 ± 14.8	48.2 ± 3.4	0.98 ± 0.09	0.45 ± 0.04
40%–45%	80.2 ± 5.6	170.2 ± 13.6	38.2 ± 2.7	0.95 ± 0.09	0.45 ± 0.05
45%–50%	63.9 ± 4.7	132.2 ± 11.0	29.7 ± 2.1	0.93 ± 0.09	0.45 ± 0.05

TABLE XX. Charged-particle multiplicity results for 14.5-GeV Au + Au collisions. The uncertainties include the total statistical and systematic uncertainties.

Centrality	$\langle N_{\text{part}} \rangle$	$\langle N_{\text{qp}} \rangle$	$dN_{\text{ch}}/d\eta$	$(dN_{\text{ch}}/d\eta)/(0.5N_{\text{part}})$	$(dN_{\text{ch}}/d\eta)/(0.5N_{\text{qp}})$
0%–5%	337.3 ± 4.2	852.0 ± 27.5	250.9 ± 22.2	1.49 ± 0.13	0.59 ± 0.06
5%–10%	287.7 ± 4.9	710.1 ± 23.4	201.2 ± 17.7	1.40 ± 0.13	0.57 ± 0.05
10%–15%	242.5 ± 5.5	585.6 ± 22.0	164.5 ± 14.5	1.36 ± 0.12	0.56 ± 0.05
15%–20%	205.1 ± 5.9	485.5 ± 19.7	134.7 ± 11.8	1.31 ± 0.12	0.56 ± 0.05
20%–25%	172.6 ± 6.4	400.4 ± 19.6	110.0 ± 9.6	1.28 ± 0.12	0.55 ± 0.06
25%–30%	143.6 ± 7.8	325.9 ± 21.7	89.4 ± 7.8	1.25 ± 0.13	0.55 ± 0.06
30%–35%	119.2 ± 7.2	264.9 ± 19.2	72.0 ± 6.3	1.21 ± 0.13	0.54 ± 0.06
35%–40%	98.3 ± 5.8	213.7 ± 14.8	57.4 ± 5.0	1.17 ± 0.12	0.55 ± 0.06
40%–45%	80.2 ± 5.6	170.2 ± 13.6	45.2 ± 3.9	1.13 ± 0.13	0.53 ± 0.06
45%–50%	63.9 ± 4.7	132.2 ± 11.0	34.9 ± 3.0	1.09 ± 0.12	0.53 ± 0.06

TABLE XXI. Transverse-energy results for 7.7-GeV Au + Au collisions. The uncertainties include the total statistical and systematic uncertainties.

Centrality	$\langle N_{\text{part}} \rangle$	$\langle N_{\text{qp}} \rangle$	$dE_T/d\eta$ (GeV)	$(dE_T/d\eta)/(0.5N_{\text{part}})$ (GeV)	$(dE_T/d\eta)/(0.5N_{\text{qp}})$ (GeV)
0%–5%	332.1 ± 5.4	830.4 ± 33.9	137.7 ± 9.1	0.83 ± 0.06	0.33 ± 0.03
5%–10%	283.2 ± 5.9	692.3 ± 27.0	114.3 ± 7.5	0.81 ± 0.06	0.33 ± 0.03
10%–15%	240.1 ± 5.7	574.4 ± 24.0	93.3 ± 6.2	0.78 ± 0.05	0.33 ± 0.03
15%–20%	204.1 ± 5.7	479.0 ± 20.6	76.2 ± 5.0	0.75 ± 0.05	0.32 ± 0.03
20%–25%	172.9 ± 6.7	398.0 ± 19.8	62.0 ± 4.1	0.72 ± 0.05	0.31 ± 0.03
25%–30%	145.5 ± 7.2	328.1 ± 19.8	50.0 ± 3.3	0.69 ± 0.06	0.30 ± 0.03
30%–35%	121.0 ± 7.3	267.1 ± 19.0	40.1 ± 2.6	0.66 ± 0.06	0.30 ± 0.03
35%–40%	98.2 ± 7.0	211.6 ± 17.8	31.8 ± 2.1	0.66 ± 0.06	0.30 ± 0.03
40%–45%	78.8 ± 6.7	165.6 ± 16.3	24.8 ± 1.6	0.63 ± 0.07	0.30 ± 0.04
45%–50%	61.8 ± 6.5	126.4 ± 14.7	19.2 ± 1.3	0.62 ± 0.08	0.30 ± 0.04

TABLE XXII. Charged-particle multiplicity results for 7.7-GeV Au + Au collisions. The uncertainties include the total statistical and systematic uncertainties.

Centrality	$\langle N_{\text{part}} \rangle$	$\langle N_{\text{qp}} \rangle$	$dN_{\text{ch}}/d\eta$	$(dN_{\text{ch}}/d\eta)/(0.5N_{\text{part}})$	$(dN_{\text{ch}}/d\eta)/(0.5N_{\text{qp}})$
0%–5%	332.1 ± 5.4	830.4 ± 33.9	192.4 ± 16.9	1.16 ± 0.10	0.46 ± 0.04
5%–10%	283.2 ± 5.9	692.3 ± 27.0	159.2 ± 14.0	1.12 ± 0.10	0.46 ± 0.04
10%–15%	240.1 ± 5.7	574.4 ± 24.0	129.3 ± 11.3	1.08 ± 0.10	0.45 ± 0.04
15%–20%	204.1 ± 5.7	479.0 ± 20.6	105.4 ± 9.2	1.03 ± 0.09	0.44 ± 0.04
20%–25%	172.9 ± 6.7	398.0 ± 19.8	85.6 ± 7.5	0.99 ± 0.09	0.43 ± 0.04
25%–30%	145.5 ± 7.2	328.1 ± 19.8	68.8 ± 6.0	0.95 ± 0.09	0.42 ± 0.04
30%–35%	121.0 ± 7.3	267.1 ± 19.0	55.0 ± 4.8	0.91 ± 0.10	0.41 ± 0.05
35%–40%	98.2 ± 7.0	211.6 ± 17.8	43.5 ± 3.8	0.89 ± 0.10	0.41 ± 0.05
40%–45%	78.8 ± 6.7	165.6 ± 16.3	33.9 ± 3.0	0.86 ± 0.11	0.41 ± 0.05
45%–50%	61.8 ± 6.5	126.4 ± 14.7	26.1 ± 2.3	0.85 ± 0.11	0.41 ± 0.06

TABLE XXIII. Transverse-energy results for 200-GeV Cu + Cu collisions. The uncertainties include the total statistical and systematic uncertainties.

Centrality	$\langle N_{\text{part}} \rangle$	$\langle N_{\text{qp}} \rangle$	$dE_T/d\eta$ (GeV)	$(dE_T/d\eta)/(0.5N_{\text{part}})$ (GeV)	$(dE_T/d\eta)/(0.5N_{\text{qp}})$ (GeV)
0%–5%	105.6 ± 2.5	254.3 ± 11.8	166.8 ± 13.2	3.16 ± 0.26	1.31 ± 0.12
5%–10%	93.1 ± 3.0	219.0 ± 11.4	139.9 ± 11.1	3.01 ± 0.26	1.28 ± 0.12
10%–15%	80.1 ± 2.4	183.6 ± 8.6	117.1 ± 9.3	2.92 ± 0.25	1.28 ± 0.12
15%–20%	68.4 ± 2.5	153.0 ± 7.7	97.9 ± 7.8	2.86 ± 0.25	1.28 ± 0.12
20%–25%	58.4 ± 2.3	127.7 ± 7.0	81.6 ± 6.5	2.80 ± 0.25	1.28 ± 0.12
25%–30%	49.2 ± 2.1	104.9 ± 5.7	67.8 ± 5.4	2.76 ± 0.25	1.29 ± 0.12
30%–35%	41.3 ± 2.2	86.0 ± 5.8	56.1 ± 4.4	2.72 ± 0.26	1.30 ± 0.13
35%–40%	34.3 ± 2.0	69.8 ± 5.0	46.0 ± 3.6	2.68 ± 0.26	1.32 ± 0.14
40%–45%	28.1 ± 1.8	55.9 ± 4.3	37.5 ± 3.0	2.67 ± 0.27	1.34 ± 0.15

TABLE XXIV. Charged-particle multiplicity results for 200-GeV Cu + Cu collisions. The uncertainties include the total statistical and systematic uncertainties.

Centrality	$\langle N_{\text{part}} \rangle$	$\langle N_{\text{qp}} \rangle$	$dN_{\text{ch}}/d\eta$	$(dN_{\text{ch}}/d\eta)/(0.5N_{\text{part}})$	$(dN_{\text{ch}}/d\eta)/(0.5N_{\text{qp}})$
0%–5%	105.6 ± 2.5	254.3 ± 11.8	192.6 ± 13.9	3.65 ± 0.28	1.51 ± 0.13
5%–10%	93.1 ± 3.0	219.0 ± 11.4	160.1 ± 11.5	3.44 ± 0.27	1.46 ± 0.13
10%–15%	80.1 ± 2.4	183.6 ± 8.6	132.8 ± 9.5	3.32 ± 0.26	1.45 ± 0.12
15%–20%	68.4 ± 2.5	153.0 ± 7.7	110.2 ± 7.9	3.22 ± 0.26	1.44 ± 0.12
20%–25%	58.4 ± 2.3	127.7 ± 7.0	91.3 ± 6.5	3.13 ± 0.25	1.43 ± 0.13
25%–30%	49.2 ± 2.1	104.9 ± 5.7	75.2 ± 5.3	3.06 ± 0.25	1.43 ± 0.13
30%–35%	41.3 ± 2.2	86.0 ± 5.8	61.7 ± 4.4	2.99 ± 0.27	1.43 ± 0.14
35%–40%	34.3 ± 2.0	69.8 ± 5.0	50.2 ± 3.5	2.93 ± 0.27	1.44 ± 0.14
40%–45%	28.1 ± 1.8	55.9 ± 4.3	40.6 ± 2.9	2.89 ± 0.28	1.45 ± 0.15

TABLE XXV. Transverse-energy results for 62.4-GeV Cu + Cu collisions. The uncertainties include the total statistical and systematic uncertainties.

Centrality	$\langle N_{\text{part}} \rangle$	$\langle N_{\text{qp}} \rangle$	$dE_T/d\eta$ (GeV)	$(dE_T/d\eta)/(0.5N_{\text{part}})$ (GeV)	$(dE_T/d\eta)/(0.5N_{\text{qp}})$ (GeV)
0%–5%	100.5 ± 4.5	229.3 ± 8.5	107.6 ± 6.5	2.14 ± 0.16	0.94 ± 0.07
5%–10%	88.3 ± 4.8	197.8 ± 15.0	93.6 ± 5.6	2.12 ± 0.17	0.95 ± 0.09
10%–15%	78.2 ± 4.3	171.7 ± 25.2	79.3 ± 4.8	2.03 ± 0.17	0.92 ± 0.15
15%–20%	67.4 ± 4.3	144.8 ± 23.8	66.5 ± 4.0	1.97 ± 0.17	0.92 ± 0.16
20%–25%	56.6 ± 4.4	118.7 ± 11.5	55.6 ± 3.3	1.96 ± 0.19	0.94 ± 0.11
25%–30%	48.7 ± 4.9	100.0 ± 12.0	46.4 ± 2.8	1.91 ± 0.22	0.93 ± 0.12
30%–35%	40.4 ± 4.5	81.1 ± 10.4	38.6 ± 2.3	1.91 ± 0.24	0.95 ± 0.13
35%–40%	32.3 ± 4.1	63.3 ± 6.1	32.0 ± 1.9	1.98 ± 0.28	1.01 ± 0.11

TABLE XXVI. Charged-particle multiplicity results for 62.4-GeV Cu + Cu collisions. The uncertainties include the total statistical and systematic uncertainties.

Centrality	$\langle N_{\text{part}} \rangle$	$\langle N_{\text{qp}} \rangle$	$dN_{\text{ch}}/d\eta$	$(dN_{\text{ch}}/d\eta)/(0.5N_{\text{part}})$	$(dN_{\text{ch}}/d\eta)/(0.5N_{\text{qp}})$
0%–5%	100.5 ± 4.5	229.3 ± 8.5	135.3 ± 11.1	2.69 ± 0.25	1.18 ± 0.11
5%–10%	88.3 ± 4.8	197.8 ± 15.0	116.6 ± 9.5	2.64 ± 0.26	1.18 ± 0.13
10%–15%	78.2 ± 4.3	171.7 ± 25.2	97.8 ± 8.0	2.50 ± 0.25	1.14 ± 0.19
15%–20%	67.4 ± 4.3	144.8 ± 23.8	81.0 ± 6.6	2.40 ± 0.25	1.12 ± 0.20
20%–25%	56.6 ± 4.4	118.7 ± 11.5	67.0 ± 5.5	2.37 ± 0.27	1.13 ± 0.14
25%–30%	48.7 ± 4.9	100.0 ± 12.0	55.3 ± 4.5	2.27 ± 0.30	1.11 ± 0.16
30%–35%	40.4 ± 4.5	81.1 ± 10.4	45.3 ± 3.7	2.24 ± 0.31	1.12 ± 0.17
35%–40%	32.3 ± 4.1	63.3 ± 6.11	36.9 ± 3.0	2.28 ± 0.35	1.17 ± 0.15

TABLE XXVII. Transverse-energy results for 200-GeV Cu + Au collisions. The uncertainties include the total statistical and systematic uncertainties.

Centrality	$\langle N_{\text{part}} \rangle$	$\langle N_{\text{qp}} \rangle$	$dE_T/d\eta$ (GeV)	$(dE_T/d\eta)/(0.5N_{\text{part}})$ (GeV)	$(dE_T/d\eta)/(0.5N_{\text{qp}})$ (GeV)
0%–5%	189.0 ± 5.2	463.8 ± 17.6	288.3 ± 17.3	3.05 ± 0.20	1.24 ± 0.09
5%–10%	164.2 ± 4.3	400.3 ± 14.8	249.8 ± 15.0	3.04 ± 0.20	1.25 ± 0.09
10%–15%	142.4 ± 3.7	341.7 ± 12.7	212.8 ± 12.8	2.99 ± 0.20	1.25 ± 0.09
15%–20%	122.6 ± 3.3	288.9 ± 10.7	179.4 ± 10.8	2.93 ± 0.19	1.24 ± 0.09
20%–25%	104.5 ± 3.5	240.5 ± 11.0	150.0 ± 9.0	2.87 ± 0.20	1.25 ± 0.09
25%–30%	88.5 ± 4.0	199.0 ± 11.8	124.5 ± 7.5	2.81 ± 0.21	1.25 ± 0.11
30%–35%	73.8 ± 3.6	162.6 ± 9.8	102.3 ± 6.1	2.77 ± 0.21	1.26 ± 0.11
35%–40%	60.9 ± 3.6	131.0 ± 8.8	83.3 ± 5.0	2.74 ± 0.23	1.27 ± 0.11
40%–45%	49.7 ± 3.2	103.4 ± 8.8	67.0 ± 4.0	2.69 ± 0.24	1.29 ± 0.13
45%–50%	39.9 ± 3.1	80.6 ± 8.5	53.1 ± 3.2	2.66 ± 0.26	1.32 ± 0.16
50%–55%	31.4 ± 3.2	62.3 ± 8.1	41.4 ± 2.5	2.64 ± 0.31	1.33 ± 0.19
55%–60%	24.3 ± 2.8	47.1 ± 6.9	31.9 ± 1.9	2.63 ± 0.34	1.36 ± 0.21

TABLE XXVIII. Charged-particle multiplicity results for 200-GeV Cu + Au collisions. The uncertainties include the total statistical and systematic uncertainties.

Centrality	$\langle N_{\text{part}} \rangle$	$\langle N_{\text{qp}} \rangle$	$dN_{\text{ch}}/d\eta$	$(dN_{\text{ch}}/d\eta)/(0.5N_{\text{part}})$	$(dN_{\text{ch}}/d\eta)/(0.5N_{\text{qp}})$
0%–5%	189.0 ± 5.2	463.8 ± 17.6	333.5 ± 25.0	3.53 ± 0.28	1.44 ± 0.12
5%–10%	164.2 ± 4.3	400.3 ± 14.8	288.0 ± 21.4	3.51 ± 0.28	1.44 ± 0.12
10%–15%	142.4 ± 3.7	341.7 ± 12.7	244.5 ± 18.1	3.43 ± 0.27	1.43 ± 0.11
15%–20%	122.6 ± 3.3	288.9 ± 10.7	205.4 ± 15.1	3.35 ± 0.26	1.42 ± 0.11
20%–25%	104.5 ± 3.5	240.5 ± 11.0	171.2 ± 12.5	3.28 ± 0.26	1.42 ± 0.12
25%–30%	88.5 ± 4.0	199.0 ± 11.8	141.5 ± 10.2	3.20 ± 0.27	1.42 ± 0.13
30%–35%	73.8 ± 3.6	162.6 ± 9.8	115.9 ± 8.3	3.14 ± 0.27	1.43 ± 0.13
35%–40%	60.9 ± 3.6	131.0 ± 8.8	94.0 ± 6.7	3.09 ± 0.29	1.43 ± 0.14
40%–45%	49.7 ± 3.2	103.4 ± 8.8	75.2 ± 5.4	3.03 ± 0.29	1.45 ± 0.16
45%–50%	39.9 ± 3.1	80.6 ± 8.5	59.5 ± 4.2	2.98 ± 0.31	1.48 ± 0.19
50%–55%	31.4 ± 3.2	62.3 ± 8.1	46.3 ± 3.3	2.95 ± 0.37	1.48 ± 0.22
55%–60%	24.3 ± 2.8	47.1 ± 6.9	35.4 ± 2.5	2.91 ± 0.39	1.50 ± 0.24

TABLE XXIX. Transverse-energy results for 193-GeV U + U collisions. The uncertainties include the total statistical and systematic errors.

Centrality	$\langle N_{\text{part}} \rangle$	$dE_T/d\eta$ (GeV)	$(dE_T/d\eta)/(0.5N_{\text{part}})$ (GeV)
0%–5%	418.8 ± 5.0	783.0 ± 46.1	3.74 ± 0.22
5%–10%	353.2 ± 6.0	625.6 ± 36.9	3.54 ± 0.22
10%–15%	296.7 ± 6.1	504.0 ± 29.7	3.40 ± 0.21
15%–20%	248.9 ± 6.8	406.2 ± 23.9	3.26 ± 0.21
20%–25%	207.6 ± 6.7	325.9 ± 19.2	3.14 ± 0.21
25%–30%	172.5 ± 6.5	259.2 ± 15.3	3.00 ± 0.21
30%–35%	141.6 ± 6.8	203.7 ± 12.0	2.88 ± 0.22
35%–40%	114.9 ± 6.9	157.8 ± 9.3	2.75 ± 0.23
40%–45%	91.8 ± 6.4	119.9 ± 7.1	2.61 ± 0.24
45%–50%	72.0 ± 6.2	89.16 ± 5.3	2.48 ± 0.26

TABLE XXX. Charged-particle multiplicity results for 193-GeV U + U collisions. The uncertainties include the total statistical and systematic errors.

Centrality	$\langle N_{\text{part}} \rangle$	$dN_{\text{ch}}/d\eta$	$(dN_{\text{ch}}/d\eta)/(0.5N_{\text{part}})$
0%–5%	418.8 ± 5.0	830.4 ± 67.8	3.97 ± 0.33
5%–10%	353.2 ± 6.0	689.2 ± 55.5	3.90 ± 0.32
10%–15%	296.7 ± 6.1	565.5 ± 44.9	3.81 ± 0.31
15%–20%	248.9 ± 6.8	459.6 ± 36.1	3.69 ± 0.31
20%–25%	207.6 ± 6.7	369.7 ± 28.7	3.56 ± 0.30
25%–30%	172.5 ± 6.5	293.9 ± 22.6	3.41 ± 0.29
30%–35%	141.6 ± 6.8	230.6 ± 17.5	3.26 ± 0.29
35%–40%	114.9 ± 6.9	178.1 ± 13.4	3.10 ± 0.30
40%–45%	91.8 ± 6.4	135.0 ± 10.1	2.94 ± 0.30
45%–50%	72.0 ± 6.2	100.0 ± 7.4	2.78 ± 0.32

TABLE XXXI. Transverse-energy results for 200-GeV d + Au collisions. The uncertainties include the total statistical and systematic uncertainties.

Centrality	$\langle N_{\text{part}} \rangle$	$\langle N_{\text{qp}} \rangle$	$dE_T/d\eta$ (GeV)	$(dE_T/d\eta)/(0.5N_{\text{part}})$ (GeV)	$(dE_T/d\eta)/(0.5N_{\text{qp}})$ (GeV)
0%–5%	17.8 ± 1.2	27.2 ± 2.3	20.3 ± 1.7	2.29 ± 0.24	1.39 ± 0.16
5%–10%	15.6 ± 1.0	24.7 ± 2.0	17.4 ± 1.5	2.24 ± 0.23	1.33 ± 0.15
10%–20%	14.1 ± 0.9	22.9 ± 1.8	15.4 ± 1.3	2.18 ± 0.23	1.27 ± 0.14
20%–30%	11.9 ± 0.7	20.0 ± 1.5	13.2 ± 1.1	2.21 ± 0.22	1.27 ± 0.14
30%–40%	10.5 ± 0.6	18.0 ± 1.2	11.3 ± 0.9	2.16 ± 0.22	1.22 ± 0.13
40%–50%	8.7 ± 0.5	15.3 ± 0.9	9.5 ± 0.8	2.20 ± 0.22	1.23 ± 0.12
50%–60%	7.1 ± 0.4	12.7 ± 0.6	7.8 ± 0.7	2.19 ± 0.23	1.23 ± 0.12
60%–70%	5.7 ± 0.4	10.4 ± 0.5	6.3 ± 0.5	2.21 ± 0.23	1.23 ± 0.12

TABLE XXXII. Charged-particle multiplicity results for 200-GeV d + Au collisions. The uncertainties include the total statistical and systematic uncertainties.

Centrality	$\langle N_{\text{part}} \rangle$	$\langle N_{\text{qp}} \rangle$	$dN_{\text{ch}}/d\eta$	$(dN_{\text{ch}}/d\eta)/(0.5N_{\text{part}})$	$(dN_{\text{ch}}/d\eta)/(0.5N_{\text{qp}})$
0%–5%	17.8 ± 1.2	27.2 ± 2.3	20.8 ± 1.5	2.43 ± 0.23	1.53 ± 0.17
5%–10%	15.6 ± 1.0	24.7 ± 2.0	17.7 ± 1.2	2.36 ± 0.22	1.43 ± 0.15
10%–20%	14.1 ± 0.9	22.9 ± 1.8	15.5 ± 1.1	2.28 ± 0.21	1.35 ± 0.14
20%–30%	11.9 ± 0.7	20.0 ± 1.5	13.2 ± 0.9	2.30 ± 0.21	1.32 ± 0.13
30%–40%	10.5 ± 0.6	18.0 ± 1.2	11.2 ± 0.8	2.22 ± 0.20	1.25 ± 0.12
40%–50%	8.7 ± 0.5	15.3 ± 0.9	9.3 ± 0.7	2.23 ± 0.20	1.22 ± 0.11
50%–60%	7.1 ± 0.4	12.7 ± 0.6	7.5 ± 0.5	2.18 ± 0.20	1.18 ± 0.10
60%–70%	5.7 ± 0.4	10.4 ± 0.5	5.8 ± 0.4	2.12 ± 0.20	1.12 ± 0.10

TABLE XXXIII. Transverse-energy results for 200-GeV ^3He + Au collisions. The uncertainties include the total statistical and systematic uncertainties.

Centrality	$\langle N_{\text{part}} \rangle$	$\langle N_{\text{qp}} \rangle$	$dE_T/d\eta$ (GeV)	$(dE_T/d\eta)/(0.5N_{\text{part}})$ (GeV)	$(dE_T/d\eta)/(0.5N_{\text{qp}})$ (GeV)
0%–5%	25.0 ± 2.0	37.5 ± 3.1	26.7 ± 1.8	2.13 ± 0.19	1.33 ± 0.14
5%–10%	22.6 ± 1.3	34.3 ± 2.4	23.2 ± 1.5	2.06 ± 0.18	1.27 ± 0.12
10%–20%	19.9 ± 1.1	30.6 ± 2.2	20.6 ± 1.4	2.07 ± 0.18	1.26 ± 0.12
20%–30%	17.0 ± 1.0	26.6 ± 1.8	17.7 ± 1.2	2.08 ± 0.18	1.25 ± 0.11
30%–40%	13.8 ± 0.7	21.9 ± 1.3	14.9 ± 1.0	2.16 ± 0.18	1.27 ± 0.11
40%–50%	10.9 ± 0.7	17.4 ± 0.8	12.0 ± 0.8	2.22 ± 0.20	1.29 ± 0.10
50%–60%	8.16 ± 0.5	13.2 ± 0.8	9.3 ± 0.6	2.29 ± 0.21	1.32 ± 0.12
60%–70%	6.01 ± 0.4	9.7 ± 0.5	7.0 ± 0.5	2.33 ± 0.21	1.34 ± 0.11

TABLE XXXIV. Charged-particle multiplicity results for 200-GeV $^3\text{He} + \text{Au}$ collisions. The uncertainties include the total statistical and systematic uncertainties.

Centrality	$\langle N_{\text{part}} \rangle$	$\langle N_{\text{qp}} \rangle$	$dN_{\text{ch}}/d\eta$	$(dN_{\text{ch}}/d\eta)/(0.5N_{\text{part}})$	$(dN_{\text{ch}}/d\eta)/(0.5N_{\text{qp}})$
0%–5%	25.0 ± 2.0	37.5 ± 3.1	26.3 ± 1.8	2.10 ± 0.22	1.40 ± 0.15
5%–10%	22.6 ± 1.3	34.3 ± 2.4	22.7 ± 1.6	2.01 ± 0.18	1.32 ± 0.13
10%–20%	19.9 ± 1.1	30.6 ± 2.2	19.9 ± 1.4	2.00 ± 0.18	1.30 ± 0.13
20%–30%	17.0 ± 1.0	26.6 ± 1.8	16.9 ± 1.2	1.99 ± 0.18	1.27 ± 0.12
30%–40%	13.8 ± 0.8	21.9 ± 1.3	14.0 ± 1.0	2.04 ± 0.18	1.28 ± 0.12
40%–50%	10.9 ± 0.7	17.4 ± 0.8	11.2 ± 0.8	2.06 ± 0.19	1.28 ± 0.11
50%–60%	8.16 ± 0.5	13.2 ± 0.8	8.4 ± 0.6	2.06 ± 0.20	1.27 ± 0.12
60%–70%	6.01 ± 0.4	9.72 ± 0.5	5.9 ± 0.4	1.98 ± 0.19	1.22 ± 0.11

- [1] X.-N. Wang and M. Gyulassy, Energy and Centrality Dependence of Rapidity Densities at RHIC, *Phys. Rev. Lett.* **86**, 3496 (2001).
- [2] D. Kharzeev and M. Nardi, Hadron production in nuclear collisions at RHIC and high density QCD, *Phys. Lett. B* **507**, 121 (2001).
- [3] S. S. Adler *et al.* (PHENIX Collaboration), Systematic studies of the centrality and $\sqrt{s_{NN}}$ dependence of the $dE_T/d\eta$ and $dN_{\text{ch}}/d\eta$ in heavy ion collisions at mid-rapidity, *Phys. Rev. C* **71**, 034908 (2005); **71**, 049901(E) (2005).
- [4] X.-N. Wang and M. Gyulassy, HIJING: A Monte Carlo Model for Multiple Jet Production in pp , pA and AA Collisions, *Phys. Rev. D* **44**, 3501 (1991).
- [5] K. J. Eskola, K. Kajantie, P. V. Ruuskanen, and K. Tuominen, Scaling of transverse energies and multiplicities with atomic number and energy in ultrarelativistic nuclear collisions, *Nucl. Phys. B* **570**, 379 (2000).
- [6] Z.-W. Lin, S. Pal, C. M. Ko, B.-A. Li, and Bin Zhang, Charged particle rapidity distributions at relativistic energies, *Phys. Rev. C* **64**, 011902 (2001).
- [7] S. Eremín and S. Voloshin, Nucleon participants or quark participants?, *Phys. Rev. C* **67**, 064905 (2003).
- [8] S. S. Adler *et al.* (PHENIX Collaboration), Transverse-energy distributions at midrapidity in $p+p$, $d+\text{Au}$, and $\text{Au}+\text{Au}$ collisions at $\sqrt{s_{NN}} = 62.4200$ GeV and implications for particle-production models, *Phys. Rev. C* **89**, 044905 (2014).
- [9] A. Bialas, M. Bleszynski, and W. Czyz, Multiplicity distributions in nucleus-nucleus collisions at high-energies, *Nucl. Phys. B* **111**, 461 (1976).
- [10] Y. Aoki, G. Endrodi, Z. Fodor, S. D. Katz, and K. K. Szabo, The order of the quantum chromodynamics transition predicted by the standard model of particle physics, *Nature (London)* **443**, 675 (2006).
- [11] S. Ejiri, Canonical Partition Function and Finite Density Phase Transition in Lattice QCD, *Phys. Rev. D* **78**, 074507 (2008).
- [12] M. A. Stephanov, K. Rajagopal, and E. V. Shuryak, Signatures of the Tricritical Point in QCD, *Phys. Rev. Lett.* **81**, 4816 (1998).
- [13] K. Adcox *et al.* (PHENIX Collaboration), Centrality Dependence of Charged Particle Multiplicity in $\text{Au}-\text{Au}$ Collisions at $\sqrt{s_{NN}} = 130$ GeV, *Phys. Rev. Lett.* **86**, 3500 (2001).
- [14] K. Adcox *et al.* (PHENIX Collaboration), Measurement of the Midrapidity Transverse Energy Distribution from $\sqrt{s_{NN}} = 130$ GeV $\text{Au} + \text{Au}$ Collisions at RHIC, *Phys. Rev. Lett.* **87**, 052301 (2001).
- [15] I. Arsene *et al.* (BRAHMS Collaboration), Quark gluon plasma and color glass condensate at RHIC? The Perspective from the BRAHMS experiment, *Nucl. Phys. A* **757**, 1 (2005).
- [16] C. Adler *et al.* (STAR Collaboration), Multiplicity Distribution and Spectra of Negatively Charged Hadrons in $\text{Au} + \text{Au}$ Collisions at $\sqrt{s_{NN}} = 130$ GeV, *Phys. Rev. Lett.* **87**, 112303 (2001).
- [17] B. Alver *et al.* (PHOBOS Collaboration), Phobos results on charged particle multiplicity and pseudorapidity distributions in $\text{Au} + \text{Au}$, $\text{Cu} + \text{Cu}$, $d + \text{Au}$, and $p + p$ collisions at ultra-relativistic energies, *Phys. Rev. C* **83**, 024913 (2011).
- [18] J. Adams *et al.* (STAR Collaboration), Measurements of transverse energy distributions in $\text{Au} + \text{Au}$ collisions at $\sqrt{s_{NN}} = 200$ GeV, *Phys. Rev. C* **70**, 054907 (2004).
- [19] K. Adcox *et al.* (PHENIX Collaboration), PHENIX detector overview, *Nucl. Instrum. Methods Phys. Res., Sec. A* **499**, 469 (2003).
- [20] K. Adcox *et al.* (PHENIX Collaboration), PHENIX central arm tracking detectors, *Nucl. Instrum. Methods Phys. Res., Sec. A* **499**, 489 (2003).
- [21] L. Aphecetche *et al.* (PHENIX Collaboration), PHENIX calorimeter, *Nucl. Instrum. Methods Phys. Res., Sec. A* **499**, 521 (2003).
- [22] M. Allen *et al.* (PHENIX Collaboration), PHENIX inner detectors, *Nucl. Instrum. Methods Phys. Res., Sec. A* **499**, 549 (2003).
- [23] B. B. Back *et al.* (PHOBOS Collaboration), Collision geometry scaling of $\text{Au} + \text{Au}$ pseudorapidity density from $\sqrt{s_{NN}} = 19.6$ GeV to 200-GeV, *Phys. Rev. C* **70**, 021902 (2004).
- [24] E. Richardson *et al.* (PHENIX Collaboration), A Reaction Plane Detector for PHENIX at RHIC, *Nucl. Instrum. Methods Phys. Res., Sec. A* **636**, 99 (2011).
- [25] M. Bleicher *et al.*, Relativistic hadron hadron collisions in the ultrarelativistic quantum molecular dynamics model, *J. Phys. G* **25**, 1859 (1999).
- [26] M. L. Miller, K. Reygers, S. J. Sanders, and P. Steinberg, Glauber modeling in high energy nuclear collisions, *Ann. Rev. Nucl. Part. Sci.* **57**, 205 (2007).
- [27] W. Busza, J. E. Elias, D. F. Jacobs, P. A. Swartz, C. C. Young, and M. R. Sogard, Charged-Particle Multiplicity in π^- -Nucleus Interactions at 100 GeV/c and 175-GeV/c, *Phys. Rev. Lett.* **34**, 836 (1975).
- [28] W. Reisdorf *et al.* (FOPI Collaboration), Central collisions of Au on Au at 150, 250 and 400 MeV/nucleon, *Nucl. Phys. A* **612**, 493 (1997).

- [29] L. Ahle *et al.* (E802 Collaboration), Simultaneous multiplicity and forward energy characterization of particle spectra in Au + Au collisions at 11.6-A GeV/c, *Phys. Rev. C* **59**, 2173 (1999).
- [30] S. V. Afanasiev *et al.*, Recent results on spectra and yields from NA49 Collaboration, *Proceedings, 16th International Conference on Ultra-Relativistic nucleus nucleus collisions (Quark Matter 2012)*, *Nucl. Phys. A* **715**, 161 (2003).
- [31] S. Chatrchyan *et al.* (CMS Collaboration), Measurement of the Pseudorapidity and Centrality Dependence of the Transverse Energy Density in Pb-Pb collisions at $\sqrt{s_{NN}} = 2.76$ TeV, *Phys. Rev. Lett.* **109**, 152303 (2012).
- [32] L. Ahle *et al.* (E802 Collaboration), Kaon production in Au + Au collisions at 11.6-A GeV/c, *Phys. Rev. C* **58**, 3523 (1998).
- [33] L. Ahle *et al.* (E917 and E866 Collaborations), An Excitation function of K^- and K^+ production in Au + Au reactions at the AGS, *Phys. Lett. B* **490**, 53 (2000).
- [34] B. I. Abelev *et al.* (STAR Collaboration), Identified particle production, azimuthal anisotropy, and interferometry measurements in Au + Au collisions at $\sqrt{s_{NN}} = 9.2$ GeV, *Phys. Rev. C* **81**, 024911 (2010).
- [35] K. Aamodt *et al.* (ALICE Collaboration), Centrality Dependence of the Charged-Particle Multiplicity Density at Mid-Rapidity in Pb-Pb Collisions at $\sqrt{s_{NN}} = 2.76$ TeV, *Phys. Rev. Lett.* **106**, 032301 (2011).
- [36] G. Aad *et al.* (ATLAS Collaboration), Measurement of the centrality dependence of the charged particle pseudorapidity distribution in lead-lead collisions at $\sqrt{s_{NN}} = 2.76$ TeV with the ATLAS detector, *Phys. Lett. B* **710**, 363 (2012).
- [37] J. D. Bjorken, Highly Relativistic Nucleus-Nucleus Collisions: The Central Rapidity Region, *Phys. Rev. D* **27**, 140 (1983).
- [38] F. Karsch, Lattice QCD at high temperature and density, *Lectures on quark matter. Proceedings, 40. International Universitätswochen for theoretical physics, 40th Winter School, IUKT 40, Lect. Notes Phys.* **583**, 209 (2002).
- [39] G. Martinez, Advances in Quark Gluon Plasma, [arXiv:1304.1452](https://arxiv.org/abs/1304.1452).
- [40] R. Nouicer, Charged particle multiplicities in A + A and p^+p collisions in the constituent quarks framework, *Proceedings, Workshop for Young Scientists on the Phys. of Ultrarelativistic Nucleus-Nucleus Collisions (Hot Quarks 2006)*, *Eur. Phys. J.* **49**, 281 (2007).
- [41] U. W. Heinz and A. Kuhlman, Anisotropic Flow and Jet Quenching in Ultrarelativistic U + U Collisions, *Phys. Rev. Lett.* **94**, 132301 (2005).
- [42] T. Hirano, P. Huovinen, and Y. Nara, Elliptic flow in U + U collisions at $\sqrt{s_{NN}} = 200$ GeV and in Pb + Pb collisions at $\sqrt{s_{NN}} = 2.76$ TeV: Prediction from a hybrid approach, *Phys. Rev. C* **83**, 021902 (2011).
- [43] Md. Rihan Haque, Z.-W. Lin, and B. Mohanty, Multiplicity, average transverse momentum and azimuthal anisotropy in U + U collisions at $\sqrt{s_{NN}} = 200$ GeV using a multiphase transport model, *Phys. Rev. C* **85**, 034905 (2012).
- [44] B. Schenke, P. Tribedy, and R. Venugopalan, Initial-state geometry and fluctuations in Au + Au, Cu + Au, and U + U collisions at energies available at the BNL Relativistic Heavy Ion Collider, *Phys. Rev. C* **89**, 064908 (2014).
- [45] A. J. Kuhlman and U. W. Heinz, Multiplicity distribution and source deformation in full-overlap U + U collisions, *Phys. Rev. C* **72**, 037901 (2005).
- [46] H. Masui, B. Mohanty, and N. Xu, Predictions of elliptic flow and nuclear modification factor from 200 GeV U + U collisions at RHIC, *Phys. Lett. B* **679**, 440 (2009).
- [47] Q. Y. Shou, Y. G. Ma, P. Sorensen, A. H. Tang, F. Videbaek, and H. Wang, Parameterization of deformed nuclei for Glauber modeling in relativistic heavy ion collisions, *Phys. Lett. B* **749**, 215 (2015).
- [48] A. Adare *et al.* (PHENIX Collaboration), Centrality categorization for $R_{p(d)A}$ in high-energy collisions, *Phys. Rev. C* **90**, 034902 (2014).
- [49] D. V. Perepelitsa (private communication).
- [50] R. Hofstadter, Electron scattering and nuclear structure, *Rev. Mod. Phys.* **28**, 214 (1956).
- [51] R. J. M. Covolan, J. Montanha, and K. A. Goulianos, A New determination of the soft pomeron intercept, *Phys. Lett. B* **389**, 176 (1996).